

Electrical Properties of Macro-Fiber Composite Actuators and Sensors

Justin Michael Lloyd

Thesis submitted to the faculty of the Virginia Polytechnic Institute and State University in partial fulfillment of the requirements for the degree of

Masters of Science
In
Mechanical Engineering

Dr. Daniel Inman, Chair
Dr. Harry Robertshaw
Dr. Donald Leo

June 22nd, 2004
Blacksburg, Virginia

Keywords: MFC, electrostatic modeling, capacitance, conformal mapping, actuator

Electrical Properties of Macro-Fiber Composite Actuators and Sensors

Justin Michael Lloyd

Abstract

Piezoceramic fiber composite (PFC) actuators and sensors offer many advantages over conventional monolithic piezoceramic devices. Conformable, durable and, when equipped with interdigitated electrodes (IDEs), more responsive than regular monolithic devices, PFCs promise to revolutionize the application of piezoelectric materials. Developed by the NASA-Langley Research Center, the Macro-Fiber Composite (MFC) actuator and sensor is the most sophisticated PFC device yet invented. With superior qualities among PFCs in performance, behavior repeatability and manufacturability, the MFC has spawned great interest in the commercial and academic community as a tool in multitudinous engineering applications.

While the MFC's characteristics render it a singularly useful device, limited characterization and modeling research on the MFC exists. Empirically designed and assembled, the MFC is poorly understood, especially in terms of its underlying operating principles, its dependence on design parameters and its electrical properties. The majority of published MFC studies focus on experimental quantification of MFC mechanical and actuation properties, and the research that attempts to model the MFC relies totally on finite element analysis. Published works widely assume that analytical models of the MFC are totally impossible.

Rectifying gaps in the current body of MFC research, this study presents the first accurate analytical model of the static electrical field properties of the MFC. Implementing the techniques of conformal mapping, a branch of complex analysis, the following chapters derive a closed-form, exact analytical solution describing the electrical potential field and electrical field of the MFC's dual-IDE structure. Based on the conformal mapping solution for the MFC's electrical field, the electrical field of the commercially available MFC is examined and analyzed, introducing an intuitive

knowledge of the MFC's operation. Demonstrating the utility of this solution in modeling the MFC, this work also predicts the capacitance and induced strain properties of a continuum of potential MFC designs and offers final suggestions on improving the current commercial MFC design. After establishing the theoretical underpinnings of the analytical MFC model, this report derives the conformal mapping solutions for the MFC, discusses the computational application of the resulting equations and then presents the results of numerical analyses executed using the new analytical model.

Acknowledgements

I wish to express my sincerest gratitude to the many individuals who supported and enabled, both professionally and privately, the completion of this work. Foremost, I thank my advisor, Dr. Daniel J. Inman, without whose guidance and very acceptance of me as a graduate research assistant I would undoubtedly have learned much less and enjoyed the pursuit of my Master's Degree far less. I thank my committee members, Dr. Donald Leo and Dr. Harry Robertshaw, for their sage mentoring and instruction during my tenure at Virginia Tech. Also, I thank Dr. W. Keats Wilkie, whose invention is the subject of my work and whose professional aid and kindness always ensured easy access to important information unattainable via alternate channels.

In terms of personal support, my many colleagues at CIMSS always provided me with a warm and entertaining work environment, as well as camaraderie outside of the office. Of course, my incredible roommates and friends at Virginia Tech served as the crucial foundation for my efforts, encouraging me constantly and influencing my professional and personal growth in profound and permanent ways. Without my friends, it would have been very difficult to overcome the many obstacles that I encountered during my research. I would like to thank my girlfriend, Aimee, for her bright and inspiring presence in my life, especially during the writing of this thesis. Last, and most importantly, I would like to thank my family, specifically Rick Lloyd, Rosemary Lloyd and Adam Lloyd, for their lifelong support, encouragement, constant help and belief in me. Without them, I would never have reached graduate school, let alone finish.

Table of Contents

Acknowledgements.....	iv
List of Tables and Figures.....	vii
Nomenclature.....	ix
1 Introduction.....	1
1.1 Active Materials and Piezoceramics.....	1
1.2 Active Fiber Composites.....	4
1.3 The Macro-Fiber Composite.....	7
1.4 MFC Research and Development.....	8
1.5 The MFC IDE Problem.....	11
2 Conformal Mapping.....	14
2.1 Potential and Electrical Field Problems.....	14
2.2 Complex Analysis.....	19
2.3 Conformal Mapping.....	26
2.4 Schwarz-Christoffel Mapping.....	29
2.5 Potential Solutions in the Complex Plane.....	33
3 Electrostatics Modeling.....	38
3.1 IDE Model.....	38
3.2 Schwarz-Christoffel Mapping Solution.....	43
3.3 Computational Issues.....	59
4 Model Results.....	63
4.1 Commercial MFC Electrical Properties Solution.....	63
4.2 Variation of MFC Capacitance with Respect to IDE Design.....	79
4.3 Variation of MFC Actuation Properties with Respect to IDE Design.....	84
5 Conclusions.....	90

5.1 Problem Overview and Summary of Findings.....	90
5.2 Study Contributions.....	92
5.3 Recommendations for Future Work.....	95
5.4 Concluding Remarks.....	98
Appendices.....	99
Appendix A.....	99
Commercial MFC Electrical Field Values	
Appendix B.....	104
Capacitance Values of Alternate MFC Designs	
Appendix C.....	107
Estimated Average Strain Values of Alternate MFC Designs	
Appendix D.....	110
Commercial MFC Electrode Electrical Field Values	
References.....	111
Vita.....	116

List of Tables and Figures

Table 1: Piezoceramic properties.....	3
Table 2: Rectangular domain mapping values.....	46
Table 3: MFC unit cell mapping values, w-plane.....	54
Table 4: MFC unit cell mapping values, ζ -plane.....	55
Table 5: Commercial MFC unit cell dimensions.....	64
Table 6: Critical mapping values for the commercial MFC unit cell.....	64
Table 7: Commercial MFC unit cell analysis results.....	78
Figure 1: PFC structure.....	5
Figure 2: PFC operating principle.....	5
Figure 3: MFC structure.....	8
Figure 4: MFC photo.....	8
Figure 5: Complex number geometry.....	21
Figure 6: Basic mapping concepts.....	23
Figure 7: Orthogonal curves.....	25
Figure 8: Sector mapping diagram.....	30
Figure 9: General Schwarz-Christoffel mapping diagram.....	32
Figure 10: Internal MFC structure schematic.....	38
Figure 11: MFC symmetry.....	39
Figure 12: 3-D MFC unit cell.....	41
Figure 13: 2-D MFC unit cell.....	42
Figure 14: Rectangular domain in the complex plane.....	43
Figure 15: Mapped rectangular domain in the w-plane.....	49
Figure 16: Mapping correspondence between w-plane and z-plane.....	50
Figure 17: MFC unit cell in the complex plane.....	53
Figure 18: Mapped MFC unit cell in the w-plane.....	53
Figure 19: Mapped MFC unit cell in the ζ -plane.....	55
Figure 20: Commercial MFC solution grid in the z-plane.....	65
Figure 21: Commercial MFC solution grid in the w-plane.....	66
Figure 22: Commercial MFC potential solution in the w-plane.....	67
Figure 23: Commercial MFC potential solution in the z-plane.....	68

Figure 24: Commercial MFC electrical field solution.....	69
Figure 25: Commercial MFC FEA electrical field solution.....	70
Figure 26: Error between fine mesh FEA and conformal mapping solutions.....	71
Figure 27: Error between coarse mesh FEA and conformal mapping solutions.....	72
Figure 28: Diagram of a generic capacitor system.....	73
Figure 29: Electrical field of high-voltage unit cell electrode.....	74
Figure 30: FEA electrical field of high-voltage unit cell electrode.....	75
Figure 31: Capacitance of unit cell designs, view #1.....	81
Figure 32: Capacitance of unit cell designs, view #2.....	81
Figure 33: Capacitance of unit cell designs, zoomed view #1.....	83
Figure 34: Capacitance of unit cell designs, zoomed view #2.....	84
Figure 35: Estimated average induced strain of unit cell designs.....	87
Figure 36: Estimated average induced strain of unit cell designs, zoomed view.....	88

Nomenclature

- a = unit cell width, center-to-center spacing of interdigitated electrodes
- $A(.)$ = arbitrary parametric smooth curve in the complex plane, intersects $B(.)$
- A_n = discrete area element of interdigitated electrode
- α = vertex number
- \arg = phase of a complex number, interpreted as a vector angle
- $B(.)$ = arbitrary parametric smooth curve in the complex plane, intersects $A(.)$
- β = interior angle change factor
- C = constant multiplier
- C_1 = constant of integration
- d = $\frac{1}{2}$ interdigitated electrode width
- d_{31} = indirect piezoelectric constant, electrical field perpendicular to mechanical field
- d_{33} = direct piezoelectric constant, electrical field aligned with mechanical field
- \underline{D} = electrical displacement field
- D = w -plane domain, primary domain
- D' = z -plane domain, mapped domain
- $E(.)$ = complex electrical field solution
- \underline{E} = electrical field
- E_u = partial derivative of electrical field with respect to u
- E_v = partial derivative of electrical field with respect to v
- E_y = partial derivative of electrical field with respect to y
- $\Xi(.)$ = electric flux function
- $f(.)$ = complex function
- $f^1(.)$ = inverse complex function
- $F(.)$ = incomplete elliptic integral of the first kind, elliptic function of the first kind
- $g(.)$ = inverse complex function
- γ = a real constant that characterizes an angle direction change
- h = unit cell height, half of the height of a piezoceramic fiber
- $h(.)$ = a real composition function that is harmonic
- i = imaginary number, $(-1)^{1/2}$

- j = imaginary number, $(-1)^{1/2}$
 k = elliptic modulus
 k' = complementary elliptic modulus
 k_ζ = ζ -plane elliptic modulus
 $K(\cdot)$ = complete elliptic integral of the first kind, complete elliptic function of the first kind
 n = a real integer constant characterizing the angle of a direction change
 $P(\cdot)$ = complex potential function
 π = pi, 3.141.....
 p = characteristic mapping constant for the MFC problem
 P = arbitrary point in the complex plane
 $\Phi(\cdot)$ = real potential function
 Q = charge
 ρ = total charge contained in a system
 \underline{S} = 2-D surface function
 t = length of unit cell electrodes
 θ = angle of intersection of two smooth curves in the complex plane
 $u(\cdot)$ = real function constituting the real part of a complex function
 u_x = partial derivative of $u(\cdot)$ with respect to x
 u_y = partial derivative of $u(\cdot)$ with respect to y
 u_0 = level curve in the complex plane, output of $u(x_0, y_0)$
 v_0 = level curve in the complex plane, output of $v(x_0, y_0)$
 V_0 = constant voltage differential
 $v(\cdot)$ = real function constituting the imaginary part of a complex function
 v_x = partial derivative of $v(\cdot)$ with respect to x
 v_y = partial derivative of $v(\cdot)$ with respect to y
 V = voltage, potential solution
 w = complex variable, w -plane
 w_0 = arbitrary complex constant, w -plane
 x = real variable
 x_0 = arbitrary real constant

y = real variable
 y_0 = arbitrary real constant
 z = complex variable, z -plane
 \bar{z} = complex conjugate of z
 z_0 = arbitrary complex constant, z -plane
 ζ = complex variable, ζ -plane

Chapter 1

Introduction

1.1 Active Materials and Piezoceramics

Over the past twenty years, research in the development and application of active or “smart” materials has blossomed, occupying both academic and commercial efforts. The propagation of new research in active materials results from the now established recognition of their versatile and incomparable capabilities, the relatively recent invention of several new types and their increasing availability and affordability. More than ever before, engineers and scientists are exploiting the unique properties of cheap, diverse smart materials to overcome a plethora of technological challenges.

As a broad definition, an active material functions as an energy conversion device, transforming an energy input of one form into an energy output of another form. In this sense, a variety of materials qualify as active materials, including shape-memory alloys, electroactive polymers, magnetorheological fluids and piezoceramics. Each of these materials accepts one type of input field and outputs a field of another form. For example, a shape-memory alloy produces a displacement field output in response to a thermal field input and an electroactive polymer produces a displacement field output in response to an electrical field input. In some cases, the active material exhibits a reversible input/output relationship, and the input field of the material is interchangeable with the output field (i.e. an electrical input creates a mechanical output and a mechanical input creates an electrical output).

With this special quality, active materials hold great potential for the solution of engineering problems. Readily adaptable to both sensing and actuation duties, the energy-conversion properties of smart materials have revolutionized the fundamental approaches to solving many modern and classical engineering problems. Engineering topics like vibration, structural control, automation and data-acquisition all benefit from smart materials application. A vast multitude of engineering accomplishments ranging

from the active control of helicopter rotor blades [ref. 25] to new methods of chemical sensing in ionic solutions [ref. 21] to the locomotion of MEMS-based robots [ref. 30] have been enabled by the employment of active materials. Engineers implement smart materials to address issues as commonplace as the vibration suppression of cantilever beams [ref. 38] and as exotic as the micro-positioning of satellite telescope mirrors [ref. 19].

Along with finding application in pre-existing fields of engineering inquiry, active materials have opened many new branches of investigation for engineers, generating new technologies to solve previously intractable problems. Previously impractical areas of modern research such as structural health monitoring, power harvesting and collocated sensing/actuation formed as a direct consequence of the capabilities of smart material devices. Indeed, these powerful materials present research and design engineers with the prospect of developing nearly limitless new technologies to overcome previously insurmountable, and perhaps unimagined, obstacles.

Despite the futuristic, cutting-edge façade of smart materials, researchers discovered some classes of active materials decades ago. Most notable in this respect are the earliest known active materials, piezoelectrics. Pierre and Jacques Curie discovered piezoelectric materials in the form of quartz, tourmaline and Rochelle salts in 1880 as a result of their investigations of pyroelectricity [ref. 16]. Like electroactive polymers, piezoelectric materials change shape in response to an applied electric field. Discovered first by the Curies, a converse piezoelectric effect also exists, whereby piezoelectric materials generate an electrical charge in response to a mechanical force input. The chemically-derived Rochelle salts studied by the Curies exhibited a stronger form of this effect than the naturally occurring quartz and tourmaline, but practical uses for the newly discovered piezoelectric effect temporarily languished.

Beginning in 1916, engineering uses for piezoelectric materials began to materialize in the form of primitive sonar and several types of acoustic devices [ref 16]. Characterization work conducted by early pioneers in piezoelectrics, such as Walter G.

Cady, led to the development of several new and more robust types of piezoelectric materials [ref. 16]. Eventually, researchers introduced the first piezoelectric ceramic, Barium Titanate, in 1940, ushering in a new era of durable, responsive piezoelectric materials dubbed piezoceramics. Polycrystalline, metallic compounds, piezoceramics exhibit extremely strong electromechanical coupling and mechanical properties similar to other ceramic materials. A flurry of improved piezoceramics exhibiting stronger piezoelectric effects were developed over the course of the next two decades, yielding the most common modern piezoceramics like lead zirconate titanate (PZT) and lead metaniobate (PMN).

Among other types of active materials, piezoceramics exhibit several notable characteristics which render them particularly useful in many applications. Although the electrically induced strains of piezoceramics are relatively small (around 0.1%), piezoceramic force outputs can be very large, resulting in high energy density. Piezoceramic response times are very short, rendering them particularly useful in high-frequency, high bandwidth applications, such as structural control and high-frequency vibration damping. Additionally, piezoceramic materials exhibit high-sensitivity to mechanical deformation, producing measurable charges for very small applied displacements. This feature makes them attractive for implementation as sensors.

Material	K_3^T (1kHz)	k_{33}	d_{33} , pm/V	d_{31} , pm/V	ρ , g/cm ³	s_{33}^E	s_{11}^E	s_{13}^E	s_{44}^E
PZT-5A	1900	0.72	390	-190	7.8	18.8	16.4	-7.22	47.5
PZT-5H	3800	0.75	650	-320	7.8	20.7	16.5	-9.1	43.5
PMN-PT	7151	0.91	2285	-1063	8.05	86.5	59.7	-45.3	14.4

Table 1: Selected material properties of three common piezoceramic materials. PMN-PT is a single-crystal piezoceramic material.

For structural actuation and sensing, piezoceramic materials are usually implemented in the form of monolithic wafers. The term monolithic refers to a single, contiguous piece of piezoceramic, free from added materials or augmenting structural components. Structural control, sensing and vibration suppression applications typically

rely on in-plane actuation and sensing, i.e. induced stresses and strains parallel to the structure's surfaces. As a result, in structural implementations, piezoceramic wafers commonly operate through the d_{31} effect, whereby an electric field administered perpendicular to the poling direction of the piezoceramic induces a perpendicular strain. Under this technique, in-plane structural strains are conveniently induced and measured with an affixed piezoceramic monolith.

Fortunately, monolithic piezoceramic wafers are easily mounted to almost any type of material, are simple to prepare for actuation or sensing and proficiently induce or sense strains in a host structure. Unfortunately, as noted before, piezoceramics possess mechanical properties similar to other ceramics and are brittle, stiff materials, displaying low strain under loads. In addition, monolithic piezoelectric actuators with uniform electrodes fail to exploit the full electro-mechanical coupling of piezoelectrics. Limiting energy-density and strain output, the d_{31} piezoelectric effect is a much weaker phenomenon than the d_{33} piezoelectric effect, where electric fields applied parallel to the direction of piezoelectric poling induce large strains in the same direction. Consequently, the inherent brittle nature of piezoceramics and primary mode of operation limit applications employing them. Many relevant and interesting areas of potential use for piezoceramics, such as the structural control of membranes or irregularly-shaped surfaces, are altogether impossible for monolithic wafers to achieve.

1.2 Active-Fiber Composites

Attempting to remedy the significant drawbacks of monolithic piezoceramics, Bent et. al. [ref. 6] developed the first generation of piezocomposite actuators. Piezocomposites combine piezoceramic materials and additional inactive components in a specific structure to form an overall actuator/sensor package. In this manner, the advantageous properties of both piezoceramics and other structural materials reinforce each other in a device that embodies the best aspects of both, creating an actuator with superior performance qualities. Considering their indisputable advantages, PFCs generate avid research interest in academic, private and government organizations, which

strive to develop improved types through experimenting with actuator geometry, construction and composition.

Pioneering PFC research, creators of the active fiber composite (AFC) avoided the conformability issues of standard piezoceramic monoliths by surrounding round, extruded piezoceramic fibers with an epoxy matrix, protecting the fibers from brittle fracture and yielding a composite device with highly conformable mechanical properties akin to epoxies. Instead of conventional electrodes producing electric fields perpendicular to the direction of the fiber poling, AFCs incorporated a dual interdigitated electrode (IDE) design, which yields an electric field roughly parallel to the direction of fiber poling. Successfully exploiting the strong d_{33} effect through the use of IDEs, the AFC almost doubled the strain output of its encased piezoceramic elements and quadrupled their strain energy density.

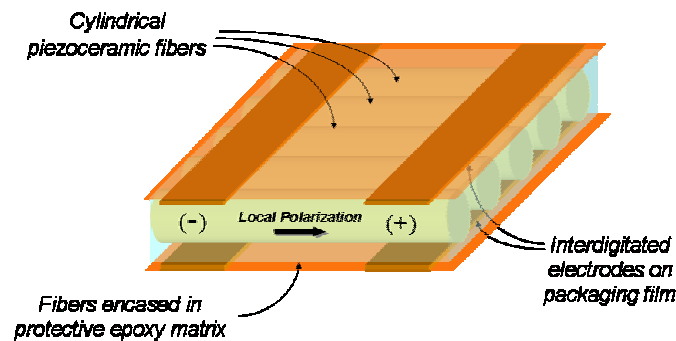


Figure 1: Section illustration of the structure of a generic piezoceramic fiber composite [ref. 35].

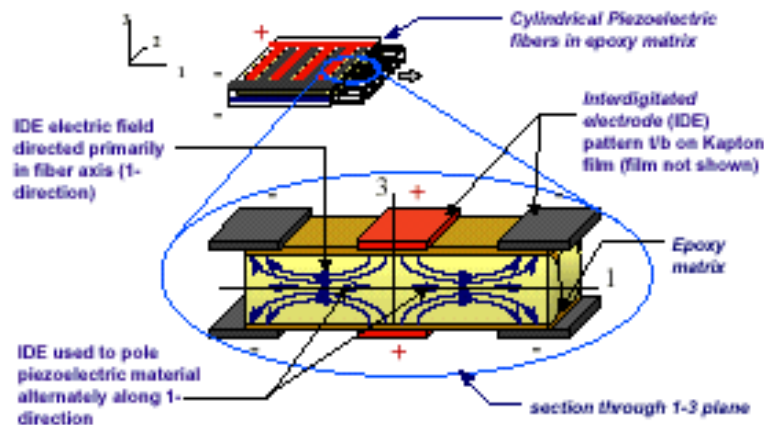


Figure 2: Section illustration explaining the operating principle of a generic PFC [ref. 35].

Due to the singular advantages of the AFC, researchers focused a great deal of effort on the development of AFC-based engineering solutions. In the first publication on the AFC, Bent et al [ref. 6] introduced the concept of combining IDEs with piezoceramic fiber composites, providing several numerical models of AFC behavior and experimental strain and capacitance values of prototype AFCs. One of the first survey papers on the AFC (Bent et al. [ref. 7]) documents a variety of early research activities involving the AFC, including investigations on manufacturing improvements and methods, characterization findings, optimization projects and applications research. Later survey papers on the characterization and technological refinement of the AFC (Rosetti et al [ref. 26]) include information on advanced AFC design methods, such as the use of single-crystal piezoceramic fibers and improved fabrication processes. In crucial characterization experiments, Morris et. al [ref. 20] focused on the load limit properties of the AFC, designing a set of experiments intended to expose the critical depoling stress limits of the AFC. Novel AFC applications research appearing in the literature comprise practical projects like the adaptive control of acoustic vibrations generated by a vibrating cylinder (Goddu et al [ref. 14]) and the reduction of vibration in aircraft rotors through active-twist control using the AFC (Wilbur et. al. [ref. 32]). Researchers continue to execute even more specific aerospace work with the AFC, equipping helicopter rotor blades with embedded AFCs to control undesired dynamics (Wickramasinghe et al [ref. 33]) and studying the fatigue limits of AFC performance in rotor control applications (Wickramasinghe et al [ref. 34]). AFC implementation has also found a place in more exotic applications, contributing to fields such as structural health monitoring (Datta et al [ref. 10], Schulz et al [ref. 28]).

Despite this large body of related research and significant accomplishments in the areas of actuation and sensing, several difficulties hampered the performance of the AFC design. Foremost, problems with attaining sufficient contact between the IDEs and cylindrical piezofibers of the AFC spawned issues with the consistency of optimal performance of the AFC. Manufacturing issues contributed to variations in the structure of one AFC to the next, reducing the repeatability in the performance of each individual

actuator and increasing the costs of mass production [ref. 36]. These drawbacks of the AFC design eventually led to the development of other, superior piezoceramic fiber composite (PFC) actuators which often employed similar design concepts.

1.3 The Macro-Fiber Composite

Responding to difficulties associated with the AFC, the NASA-Langley Research Center developed the Macro-Fiber Composite (MFC) actuator [ref. 35], addressing several shortcomings in the operational characteristics of competing PFC packages. Like the AFC, the MFC actuator package employs piezoceramic fibers locked in an epoxy matrix and sandwiched between two arrays of interdigitated electrodes. Contrasting the round fiber geometry of the AFC, however, the piezoelectric fibers in MFCs have rectangular cross sections and are assembled in the MFC package with regular spacing and precise parallel alignment. Manufacturing considerations necessitated the rectangular form of the MFC fibers, which are much more cost-effective to construct and handle in mass-production environments. Production of rectangular fibers instead of round fibers enabled the use of commercially available piezoceramic materials in raw form, which were diced into smaller piezoelectric fibers through a repeatable, cheap manufacturing process. Thus, MFC active layer geometry served to standardize the performance of mass-produced MFCs while lowering production costs. Due to these substantial manufacturing advantages, the MFC has realized actual commercial licensing and mass-production, a feat never achieved by the AFC.

Additionally, the rectangular fiber geometry of the MFC guarantees consistent, appreciable contact between the IDEs and piezoceramic fibers, reducing attenuation of the IDE electric field due to the low dielectric constant of the epoxy matrix. Because of the improved electrical contact, MFC strain performance exceeds AFC strain performance by up to 150% [ref 35]. Due to the in-situ poling scheme used in manufacturing, the poling direction of the MFC's piezoceramic fibers aligns with the electric field produced by the MFC's interdigitated electrodes, enabling the high strain output of the MFC.

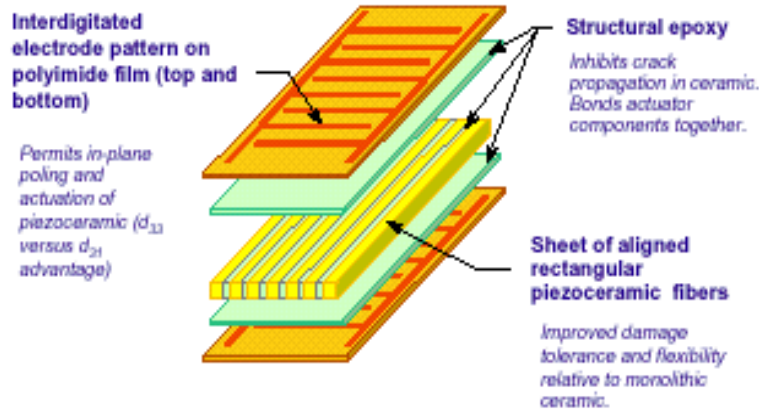


Figure 3: Diagram of the layered construction of a typical MFC [ref. 35].

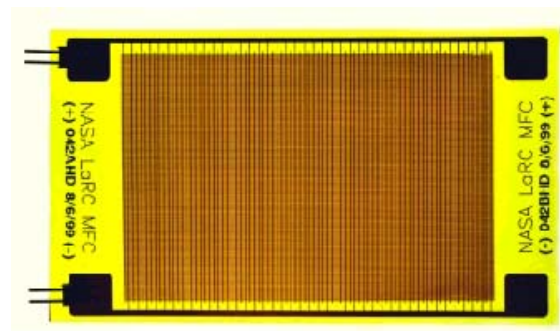


Figure 4: Top view of an actual MFC [ref. 35].

Currently manufactured by the Smart Material Corporation, MFCs are categorized as layered composite materials. Every MFC contains an orthotropic piezofiber/epoxy layer in its center, which is then sandwiched between two layers of homogenous epoxy to add structural reinforcement. Laminated to the bottom and top of the epoxy/piezofiber layers are two more orthotropic layers of IDEs, running perpendicular to the piezoceramic fibers and encapsulated in Kapton. Figure 3 illustrates the MFC structure.

1.4 MFC Research and Development

MFC research branches into two independent categorizations: characterization research and applications development. Of the two, applications development work

constitutes a much larger body of information. Recognizing the superior qualities of MFCs for sensing and structural applications, researchers have adopted the MFC as the actuator of choice for a full spectrum of structural control, vibration suppression and structural monitoring projects. Due to its high conformability, high flexibility and low mass, the MFC doesn't introduce significant mass or stiffness coupling to host structures. MFC conformability also enables mounting of the MFC to curved and flexible surfaces. Stemming from these advantageous qualities, extensive research has been conducted on using the MFC for the dynamic analysis and control of membranes and inflatable, thin-walled structures. Park et. al. [ref. 24] proved that the MFC excels in exciting the vibratory modes of inflatable, thin-walled structures by using the MFC to excite an inflatable torus satellite in modal analysis experiments. Further work on this subject by Ruggiero et. al. [ref. 27] extended this finding, showing that the MFC also functions proficiently as a sensor of vibrations in inflatable membrane structures through MIMO modal testing of an inflatable torus satellite. Building on the previous dynamic analysis work for inflatable satellites, Jha et. al. [ref. 17] implemented an active control application of the MFC actuator by designing a sliding-mode compensator with an MFC actuator for control authority. Testing their compensator on an inflatable torus satellite, Jha and his colleagues established the strength of the MFC as an actuator in structural control schemes. Departing from active control research, Adachi et. al. [ref. 1] studied the use of MFCs as passive damping devices, incorporating them as piezoelectric shunts to add damping to cantilever beams. Efforts to adapt the MFC to the burgeoning research topic of structural health monitoring (SHM) also appear in the literature. Recently, Sodano et. al [ref. 29] published a study of the MFC as an impedance-based sensor for monitoring the state of bolted-joint connections in structures, concluding that the MFC exhibits great potential in SHM applications.

Equally important but less prevalent, MFC characterization research focuses on the quantification, explanation and prediction of MFC behavior and properties. Although extremely useful, MFC technology arose from an almost completely empirical design process, leaving the specification and explanation of the mechanical properties, electronic properties, and actuation and sensing capabilities of the MFC to later investigations.

Relatively abundant experimental studies have sought to tabulate data on MFC actuation behavior and subsequently derive piezoelectric properties based on the results. In their introductory publication on the MFC in 1999, Wilkie et. al. [ref 35] presented the first voltage/strain data for the “reference” MFC design, along with long-term fatigue performance data and energy density data. Later, Williams et. al. [ref. 36] conducted more advanced characterization work on the MFC, developing first-principles based analytical models of the mechanical properties of the MFC that closely corresponded to experimental data. Williams also examined manufacturing issues, quantifying the thermal processes involved in curing the epoxy matrix of the MFC and developing methods to expedite the process. Mature comparative work between the experimentally derived performance properties of the MFC and competing PFC actuators surfaced in recent publications by Williams et al [ref. 37], who also discussed relevant manufacturing and mechanical property topics.

Various attempts to achieve accurate models of the electric behavior and electromechanical coupling of the MFC and similar PFCs (AFC) heavily focus on finite element formulations and other numerical models. The primary obstacle in explaining and modeling MFC behavior lies in the complex electrical interaction between the dual IDEs and the electromechanically coupled piezoelectric fibers composing the active layer. Efforts by Beckert and Kreher [ref. 5] to model the electric field of the IDE structure with ANSYS strove to predict the strain behavior of IDE equipped PFCs based on actuator geometry. Analyzing the micro-scale behavior of the AFC, Kim et al [ref. 18] developed a three-dimensional finite element model to calculate the local stress distributions occurring between piezoceramic fibers and epoxy matrix of PFCs during actuation. Agbossou et al [ref. 2] suggested a periodic homogenization numerical model of the electromechanical properties of IDE based PFCs and attempted to ascertain an optimal fiber aspect ratio to maximize the actuation of IDE-PFCs. Other FEA formulations considered a more global perspective of MFC implementation, modeling the MFC laminated to its host structure to predict the frequency response of the overall structure [Azzouz et al [ref. 4)].

Generally, all modeling efforts pertaining to the electromechanical behavior of the MFC assume that FEA models provide the only possible approach to obtaining solutions. Some MFC studies go so far as to specifically declare analytical solutions to the electric field produced by the dual-IDE structure to be impossible. Despite these claims, exact or even simplified analytical models of MFC response phenomena remain desirable for their explanatory value and computational efficiency. With this same motivation, scientists have administered unrelated studies to derive analytical expressions modeling the electric behavior of the IDE structure for the sake of other devices

Purely mathematical studies of the electric field of the IDE structure directly relate to MFC development, even though some treatments first appeared several decades ago. In seminal work on the subject, Engan [ref. 12] considered the excitation of elastic surface waves in piezoelectric materials through the use of surface laminated IDEs. Although Engan's work deals with a single strip of IDEs, it offers analytical expressions for the electric field and capacitance of a single strip IDE in the form of expanded harmonic polynomials. More recent examinations of the IDE design were carried out by Otter [ref. 22], who developed approximate analytical expressions for the potential distribution and capacitance of IDEs in correlation with Engan's earlier work. While both of these studies helped to reinforce the possibility of advanced analytical treatments of the electrical behavior of IDEs, neither directly engaged the problem of the dual-IDE system, having both scrutinized the simpler problem of single strip IDEs.

1.5 The MFC IDE Problem

Closing the gaps in MFC characterization research is a requisite for the optimization of MFC architecture and the development of better, more advanced MFC applications. While FEA models present a means for some understanding of the complex behavior of MFCs, and experimental data offers empirical predictions of MFC behavior, the development of an exact analytical model of MFC actuation and sensing phenomena would result in the most accurate depiction of MFC behavior. Assuming that a first-principles analysis would yield such a model, an analytical solution would offer a deeper,

more intuitive description of the MFC with real explanatory and predictive power. In addition, an analytical model would avoid the computational overhead of FEA codes and, ostensibly, be more useful in optimization studies of the MFC.

With the intent of developing an analytical model of the MFC for the enumerated reasons, the dual-IDE problem was studied. Through the use of complex analysis, conformal mapping theory and, specifically, Schwarz-Christoffel mapping, it is possible to achieve an exact analytical solution for the potential field distribution, and, consequently, the electrical field (EMF) produced by the dual-IDE structure of the MFC. Directly corresponding to the EMF solution because of the in-situ poling process used in MFC manufacturing, the polarization vector field of the MFC piezoceramic fibers also emerges from the conformal mapping analysis of the dual-IDE structure.

Precise analytical results for the poling field and electrical field of the MFC yield important information about useful engineering properties. Bulk capacitance values for the MFC were calculated based on the electrical field and potential field distributions of the dual-IDEs, leading to an explanation of MFC capacitance properties as well as useful optimization data for capacitance-based designs. Linear estimates of MFC actuation behavior, closely paralleling the actual actuation properties of MFCs, also arose through calculations based on the analytically obtained electric field and poling field results. Low computational overhead for the analytical solution enabled the quick and efficient calculation of MFC capacitance and actuation strains for a continuum of IDE geometries, culminating in optimization plots representing the electrical and actuation properties of various MFC designs.

The following chapters explain the mathematical foundations of the analytical MFC model, the conceptual modeling process, the results of the model and a discussion and analysis of the implications of the model, both for scrutinizing the electromechanics of the MFC and for optimizing its design. Summarizing, this work seeks to contribute to the body of knowledge on MFCs via three primary accomplishments:

1. The development of an exact analytical model of the electrostatic field of the MFC, facilitating an intuitive and utile characterization of the MFC's electrical properties.
2. Through the newly developed analytical model, the prediction of the relative capacitance properties of a continuum of possible MFC designs, optimizing the capacitance properties of future MFCs.
3. Through the newly developed analytical model, the prediction of the relative average induced strain properties of a continuum of possible MFC designs, optimizing the actuation capabilities of future MFCs.

For the first time, a complete understanding of the electrical phenomenon produced by the dual-IDE design is possible, in turn providing an intuitive and accurate picture of the operation of the MFC. Future progress in MFC characterization and application will be nurtured and improved as a result of these findings.

Chapter 2

Conformal Mapping

2.1 Potential and electrical field problems

Methods for determining the electrical field produced by a static system of electrically charged bodies constitute the primary focus of the field of electrostatics, forming the basis for electromagnetic theory as a whole. Although a sweeping and complex subject, the solution of most electrostatics problems finds its mathematical basis in the very accessible techniques of vector analysis. In cases where this generalization applies, a system of static bodies with known charges and geometry is analyzed using geometric relationships, multivariable calculus and vector analysis, yielding a specific vector field solution for the electric field of the system. Other solutions for system properties such as electrical potential and capacitance follow directly from the mathematical vector expression for the system electrostatic field.

Indeed, the basis of all electrostatic theory stems from a few fundamental laws, derived on the foundation of simple experimental evidence and described mathematically in terms of vector analysis. Maxwell's equations themselves, the universal expression of all of electromagnetic theory, originate from simple rules relating the force between two particles with known charges (Coulomb's Law), mathematically extended to complex geometric distributions of charge and multiple bodies. As such, the mathematical techniques for determining the electrical field and potential of a static electric system of known charges and geometry is well-developed, being fundamental and rooted in the most basic concepts of electrostatics.

In more complex cases, however, the solution of an electrostatics problem requires the determination of the electric field of a system on the basis of known potentials in the system. These inverted problems present only information on the electrical potential of the charged bodies in the system, and from this knowledge other

properties like the charge distributions and electrical field of the system are determined. Problems of this type are one concern of the subject of potential theory. Mathematical relationships between the electric potential, electrical charge and electric field of a system enable the determination of any of these characteristics when at least one is completely specified. Resultantly, the primary obstacle in solving an electrostatics potential problem lies in determining the potential field of a system from boundary information.

Naturally, this type of problem falls under the broader theoretical domain of boundary value problems. Deriving the generalized mathematical expression of the electrostatics potential problem is a simple exercise of combining Gauss's law, the relationship between an electric field and a displacement field and the relationship between the electric field and potential field. The definition of the electric displacement field of an electrostatic system is –

$$\nabla \cdot \underline{D} = \rho \quad (1)$$

where \underline{D} is the electric displacement field, operated on by the “del” operator, and ρ is the charge enclosed by the electrostatic system. The electrical permittivity constant relates the electric displacement field and the electric field of an electrostatic system –

$$\underline{D} = \epsilon \underline{E} \quad (2)$$

where \underline{E} is the electric field produced by the system and ϵ is the electric permittivity of the medium occupying space between the charged bodies of the system. Finally, the electric potential of an electrostatic system relates to the electric field of the system through the equation –

$$\underline{E} = -\nabla V \quad (3)$$

where V is the scalar potential field of the system. Combining these mathematical

expressions of the laws of electrostatics and rearranging the outcome yields –

$$\nabla \cdot \nabla V = \nabla^2 V = -\frac{\rho}{\epsilon} \quad (4)$$

Known as Poisson's equation, this expression applies to systems containing a set of conductors and electrodes separated by a space containing a charge distribution. Under circumstances where no charge exists in the space between conductors and electrodes, Poisson's equation simplifies to –

$$\nabla^2 V = 0 \quad (5)$$

This powerful result, also known as Laplace's equation, implies that, for electrostatic systems containing zero charge density, any possible arrangement of conductors and electrodes always produces a potential field for which the second-order gradient is zero.

A second order partial differential equation, Laplace's equation applies to one, two and three-dimensional system geometries. Written for a two-dimensional, Cartesian system, the Laplace equation becomes –

$$\frac{\partial^2 V}{\partial x^2} + \frac{\partial^2 V}{\partial y^2} = 0 \quad (6)$$

The uniqueness theorem, developed through basic vector calculus and integration, guarantees a unique solution to Laplace's equation for a given unique system of charged bodies [ref. 31]. Solutions to Laplace's equation, called harmonic equations or harmonics, are in the form of an equation for the scalar potential field of an electrostatics system. Application of the previously introduced electrostatics equations to the potential field results produces the electric field and electric displacement field of the system.

Due to its utility in determining the solutions to a diverse set of important electrostatic problems, many techniques for solving Laplace's equation have been developed, especially in two dimensions. In the trivial case of one dimensional systems, direct integration of Laplace's equation is possible and suffices to generate a solution for any possible set of boundary conditions, which are provided in the form of point conditions. For two-dimensions, direct analytical solutions to Laplace's equation involve applying the same techniques used to solve any two-dimensional PDE. Namely, the PDE solution process entails obtaining a general solution, usually through a separation of variables technique, and then applying the given boundary conditions to arrive at a unique solution. Boundary conditions for two dimensional potential problems are specified along lines and can be in the form of either constant potential or constant electric field (constant potential gradient). Although intuitively valuable and mathematically straightforward, direct PDE solutions to Laplace's equation fail for all but the most simplified boundary conditions, removing the possibility of solving many interesting and practical electrostatics problems. To circumvent this obstacle, other indirect techniques prove useful.

The advent of cheap, abundant computing power self-selected the numerical method of finite element analysis as the modern method of choice for solving complicated two-dimensional electrostatics problems. Often quick, usually accurate and capable of solving any set of boundary conditions, FEA overshadows other potential field solution methods developed before the invention of computers. Prominent among these alternatives, the method of images and the graphical method of curvilinear squares can successfully achieve precise mathematical and approximate graphical potential solutions, respectively, for a multitude of electrostatics problems. A mapping technique, the method of curvilinear squares consists of sketching equipotential and electrical field lines around a system of known potential boundaries. Lines are sketched under the guidance of a set of rules dictated by the known relationships between potential and electrical fields. At best, the method of curvilinear squares yields approximate results that increase with accuracy proportionally to increasing proficiency in the artistic facets of the technique. Nonetheless, useful qualitative information on the structure of a system's

electric and potential field is attainable using curvilinear square illustrations. Superior to the method of curvilinear squares and even FEA in terms of its capacity to yield exact solutions, the method of images applies to systems of point and line charges in the presence of simple dielectric and conductor surfaces. Postulating “imaginary” line and point charges outside of the system in consideration, the technique allows for the specification of the electric field through graphical methods or calculation of force interactions between the real charges in the system. While the method of images adequately solves many electrostatic problems of intermediate difficulty, it can only provide analogies or simplified models of complex electrostatics problems.

Undoubtedly, conformal mapping presents the most versatile and powerful means for obtaining analytical solutions to potential problems. Essentially, conformal mapping theory enables the transformation of elaborate boundary condition geometries, which have no solution, to geometric configurations with known potential solutions that are then transformed back to the original problem geometry. Mathematicians began to develop the theoretical foundation of conformal mapping during the mid 1800s, elaborating on their findings through the late 1800s and early 1900s. Engineers and scientists eventually recognized the practical implications of conformal mapping theory, and the early decades of the 20th century witnessed frequent application of the method to electrostatics research, among other subjects. Capable of solving a breadth of complicated problems inaccessible to direct PDE solution processes, conformal mapping procedures simultaneously offer the advantage of exact analytical solutions, eschewing the inaccuracies associated with approximate methods such as FEA. For these reasons, despite the overwhelming modern emphasis on FEA, the research community recently rediscovered the utility of conformal mapping in the investigation of many topics, including electrostatics. Over the past five years, many researchers have explored conformal mapping as a valuable comparative tool for establishing the accuracy of FEA models. Additionally, computational mathematicians have adapted the theory of conformal mapping to numerical techniques, and frequently, numerical conformal mapping packages prove more computationally efficient in obtaining potential problem solutions than FEA codes. Citing just a few examples of conformal mapping studies that

have recently appeared, Akduman et. al. [ref. 3] applies conformal mapping to numerically solve electrostatics imaging problems, Costamagna [ref. 9] surveys the utility of numerical conformal mapping techniques by solving a variety of direct and inverse mapping problems and Goano et. al. [ref. 13] apply conformal mapping to optimize the performance of waveguide designs. With the recent revival of conformal mapping methods as important tools in many engineering analyses, any search for conformal mapping literature promptly returns thousands of texts.

If any disadvantages to conformal mapping exist, they lie in the rigor of the advanced mathematics necessary to prove and apply the tenets of the theory, as well as in the difficulty of visualizing the complex function solutions generated by the theory. Indeed, conformal mapping mathematically roots itself in the erudite domain of complex analysis, demanding a working knowledge of complex function theory to derive mapping rules for a given potential problem. Thus, without at least a brief discussion of complex analysis and complex function theory, understanding and deriving conformal mapping solutions becomes impossible.

2.2 Complex Analysis

Complex analysis refers to the mathematics of complex numbers, and for every concept associated with the familiar topic of real analysis, there exists an analogue concept for complex number theory. Logically, complex number theory revolves around the manipulation and properties of complex numbers and variables, that is, numbers with both real and imaginary components. The fundamental expression of a complex number, z , in rectangular form is

$$z = x + iy \tag{7}$$

where x is the real component of z and y is the imaginary component of z . The number i

is called an imaginary number, and is defined to be

$$i = \sqrt{-1} \quad (8)$$

Complex number theory specifies a full set of algebraic operations, and complex number addition, subtraction, multiplication and division are all defined operations for complex numbers. Along with these familiar algebraic operations, an “extra” operation, termed conjugation, is uniquely defined for complex numbers as

$$\bar{z} = x - iy \quad (9)$$

where z “bar” is called the complex conjugate of z .

Analogous to analytical geometric relationships for real numbers, complex numbers exhibit certain relationships between algebraic and geometric concepts. All real numbers can be geometrically expressed as points along an infinite number line, the magnitude of the difference of two real numbers can be interpreted as a distance on the same number line and equations of a real variable correspond to curves in a plane. Similarly, a complex number may be interpreted as a coordinate in a two-dimensional plane, where the real component of the complex number corresponds to the familiar x -coordinate and the imaginary component corresponds to the y -coordinate in the plane. In this respect, the x - y plane can be viewed as the “complex plane”, containing the set of all complex numbers. Often in other texts, and for the duration of this work, the complex plane is also referred to as the z or w -plane. Implementing an even more sophisticated geometric perspective of a complex number, complex numbers can be treated as vectors, where the vector begins at the origin of the complex plane and ends at a point in the complex plane, which coincides with a unique complex number. Employing this concept, a complex number can be said to have a magnitude and angle, or argument,

which are defined as the length and angle of rotation of a vector, respectively

$$\begin{aligned} |z| &= \sqrt{x^2 + y^2} \\ \arg z &= \tan^{-1}\left(\frac{y}{x}\right) \end{aligned} \tag{10, 11}$$

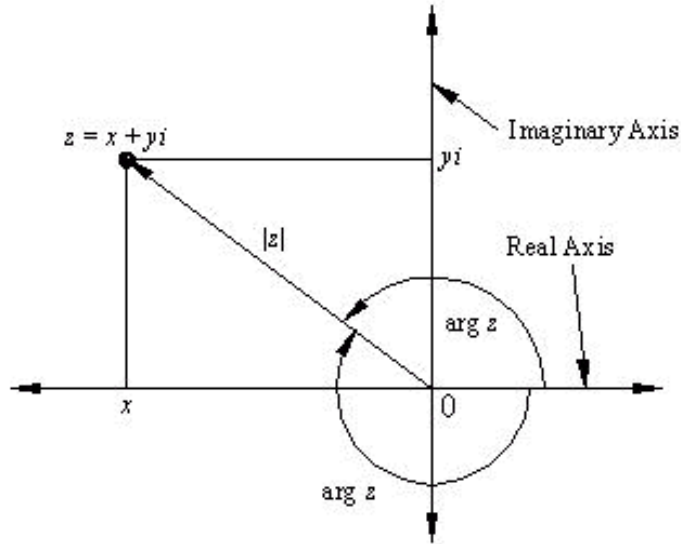


Figure 5: A complex number plotted in the complex plane. The y -axis corresponds to the imaginary portion of the complex number, while the x -axis corresponds to the real portion.

Equations (10) and (11) implicitly relate the y -component of a two-dimensional vector to the imaginary component of a complex number and the x -component of the vector with the real portion. Thus, the vector concept of a complex number provides an alternate mathematical expression of complex numbers: the “polar” form of a complex number. Polar expressions for complex numbers greatly facilitate and simplify complex number calculations.

Conceptually, the idea of a complex function is directly analogous to that of a real function. Complex functions, roughly speaking, are well-defined mathematical rules which pair one complex number with another. As with real functions, for a set of ordered complex number pairs defined by a complex function, each pair must be unique, i.e. each

first entry in a pair must occur only once, being paired with only one other complex number. So, for a complex variable z , a complex function, $f(z)$, assigns one and only one point w in the complex plane. Nomenclature for a complex function, under the previous definition, follows the standard expression for a real function

$$w = f(z) \tag{12}$$

where f is the complex function, z is the independent complex variable and w is the dependent complex variable. In the jargon of complex analysis, a specific outcome of a complex function, w_0 , is called the “image” of an input number z_0 , which is also referred to as the “preimage” of w_0 . Geometrically speaking, a complex function locates a point w on the w -plane for a given point z on the z -plane. In this sense, a complex function can be said to “map” or “transform” a set of complex numbers in the z -plane to a corresponding set of complex numbers in the w -plane, which leads to the alternate terminology for complex functions as mappings or transformations.

Particularly useful in the development of the theory supporting conformal mapping, the decomposition of a complex function into a sum of two real variable functions occurs repeatedly in proofs and statements of important complex analysis theorems. Given a complex function, f , substituting the mathematical definition of a complex variable, z , yields –

$$w = f(z) = f(x + iy) = u(x, y) + v(x, y)i \tag{13}$$

Readily verifiable for any example of a complex function, this result plays a large role in the derivation of the Cauchy-Riemann equations and theorems guaranteeing the existence of the derivatives of a complex function.

While a complex function, by definition, must match only one image point in the w -plane for each preimage point in the z -plane, more than one unique z -plane point may correspond to each w -plane point. Mappings of this type are referred to as “many-to-

one” mappings. Contrasting the many-to-one mapping, a one-to-one mapping pairs no more than one preimage point with every image point. Thus, each unique image point, w_0 , corresponds to only one unique preimage point z_0 .

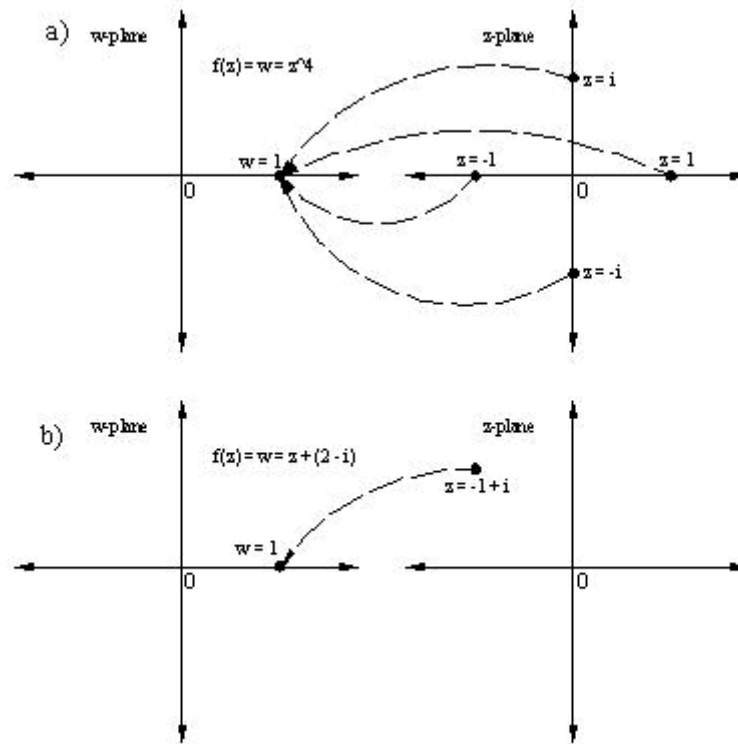


Figure 6: Illustration of the concept of one-to-one mappings and many-to-one mappings; a) shows the effects of a many-to-one map between complex planes, b) shows a one-to-one mapping function between complex planes.

One-to-one mappings exhibit the desirable property that their inverses are also valid one-to-one complex functions.

Intertwined with the mathematics of one-to-one mappings and conformal maps, the concept of the analyticity of a complex function is very similar to the idea of the regularity of a real function. Simply put, a complex function is analytical at a point z_0 if it is differentiable within a certain neighborhood of that point. Furthermore, a complex

function is guaranteed to be differentiable at a point z_0 if, at that point –

$$\begin{aligned}u_x &= v_y \\v_x &= -u_y\end{aligned}\tag{14, 15}$$

where the subscripts denote the partial derivatives in terms of x and y of the real functions $u(x,y)$ and $v(x,y)$ (eqn. (13)). Named the Cauchy-Riemann equations, equations (14) and (15) state the sufficient conditions for the existence of the derivative of a complex function $f(z)$, provided that $f(z)$ and its partial derivatives are continuous throughout some neighborhood around z_0 . An entire function is analytic at every point in the complex plane. Individual, isolated points within an analytic function that fail to meet the conditions of analyticity are referred to as singular points or singularities.

The concept of analytic complex functions has immense consequences for the solution of practical scientific and engineering problems. Serendipitously, the real and imaginary components of analytic complex functions qualify as solutions to Laplace's equation (eqn. (5)). In fact, the condition that a complex function $f(z)$ is analytic in a given domain guarantees that the real and imaginary parts of $f(z)$ are harmonic in that domain. A direct exercise, the proof of this assertion follows from differentiation of the Cauchy-Riemann equations [ref. 23]. Accordingly, the real portion of an analytic complex equation is a harmonic function, and the imaginary component is referred to as the conjugate harmonic function of the real part. Furthermore, for every unique harmonic function $u(x,y)$ defined in a given domain, there exists a unique conjugate harmonic function $v(x,y)$ defined in the same domain for which an analytic complex function $f(z)$ exists according to equation (13). From these definitions, every analytic complex function comprises a pair of harmonic conjugate functions.

Pairs of conjugate harmonic functions also define sets of mutually orthogonal curves in their specified domain of the complex plane, hinting at another extremely useful

aspect of analytic complex functions. Precisely, for a pair of conjugate harmonic functions $u(x,y)$ and $v(x,y)$ without a vanishing gradient at a point (x_0,y_0) , define

$$\begin{aligned} u(x_0, y_0) &= u_0 \\ v(x_0, y_0) &= v_0 \end{aligned} \tag{16}$$

The level curves defined as

$$\begin{aligned} u(x, y) &= u_0 \\ v(x, y) &= v_0 \end{aligned} \tag{17}$$

intersect orthogonally at (x_0,y_0) . Geometrically, this mathematical rule of conjugate harmonic functions intuitively parallels the physical phenomenon relating electric and electric potential fields, which always intersect orthogonally. In fact, in applications to electrostatic potential problems, it is conventional to identify the real portion of a complex function with the harmonic potential function, and the imaginary portion of the complex function with the conjugate harmonic electrical flux field.

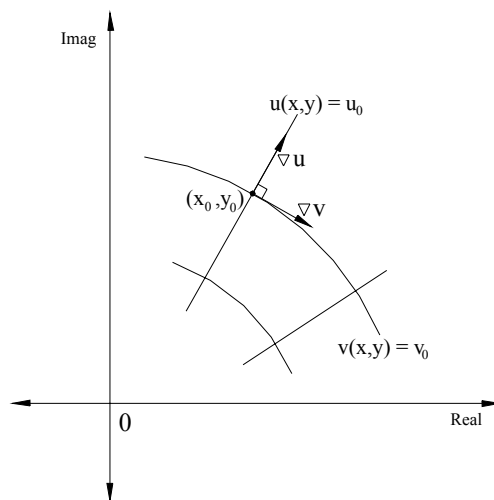


Figure 7: Schematic plot of orthogonally intersecting curves in the complex plane.

A special case of an important, broad property, the orthogonality of the real and imaginary parts of an analytic complex function leads to the complex analysis topic of conformality.

2.3 Conformal Mapping

Pertaining to the invariance of certain geometric relationships under mapping, the concept of conformality lends its name to the term conformal mapping. A complex mapping function, $f(z)$, that preserves the angle of intersection of smooth curves from the preimage plane to the image plane is called a conformal map. Specifically, a complex mapping function $f(z)$ is conformal on a given domain D if for a point z_0 in that domain and any pair of smooth curves $A(t)$ and $B(t)$ intersecting at z_0 at an angle θ , the mapped curves $f(A(t))$ and $f(B(t))$ intersecting at the image point of z_0 at $f(z_0)$ will intersect at the same angle θ .

By means of a relatively simple mathematical proof [ref. 23], it is possible to show that analytic functions $f(z)$, at points z_0 where they possess non-vanishing derivatives ($f'(z_0) \neq 0$), are conformal. Along with maintaining the values of angles between points, a complex analytic function is also a scale-preserving mapping. Simple geometric arguments taken to infinitesimal limits combined with the definition of conformality [ref. 23] readily demonstrate that complex analytic functions preserve the relative magnitudes of geometric structures within their domain of conformality, leading to the “scale-preserving” conclusion.

Applying the knowledge that conformal maps preserve the infinitesimal geometric relationships between mapped points in the complex plane, the practical leap to solving a variety of potential problems becomes possible. As stated previously, harmonic functions are solutions to the Laplace equation, which expresses the physics of electrostatic potential problems. Difficulties in determining the solution to a given electrostatic potential problem revolve around matching the values of a harmonic

equation to the boundary conditions of the problem domain. Often, this task proves impossible using conventional mathematics. Alluded to previously, one convenient way of circumventing this difficulty would be to transform the geometry of the boundary conditions of an electrostatics problem to a “simple” geometry with a known or easily attainable harmonic solution. The known harmonic solution could then be transformed back to the original problem geometry. Conformal mapping techniques offer a method for implementing this idea.

Assume that an electrostatics potential problem is posed in the complex plane with a set of “difficult” boundary conditions prescribed on a domain D . Translating a two-dimensional boundary value problem plotted on the real x - y plane to the complex plane involves the simple task of respectively equating the real coordinates x and y with the real and imaginary components of a complex variable, z . Postulating the need to determine a harmonic function $u(x,y)$ on the domain D in the z -plane, assume that a one-to-one analytic mapping $z = f(w)$ exists that transforms a “simple” image domain D' in the w -plane to the preimage domain D . If harmonic functions prove invariant under certain conditions, then a composition function, $h(w) = u(f(w))$, should exist and also be the harmonic solution to the transformed potential problem in the domain D' . Since $f(w)$ is a one-to-one mapping function, an inverse function $w = f^{-1}(z)$ exists that maps D back to D' . Thus, the harmonic solution to the original “difficult” problem on domain D follows from the determination of the harmonic solution $h(w)$ on the “simple” domain D' and the application of the transformation $u(x,y) = h(f^{-1}(z))$.

Simple calculus and the application of previously stated function definitions finally expose the relationship between one-to-one analytic mappings and conformal maps. For purposes of formality and brevity, let

$$z = f(w) \quad w = f^{-1}(z) = g(z) \quad (18)$$

From the definition of one-to-one mappings, for every point z in the domain D ,

$$w = g(f(w)) \quad (19)$$

Taking the derivative of this equation in terms of w yields

$$1 = g'(f(w))f'(w) = g'(z)f'(z) \quad (20)$$

Simplifying the expression above yields

$$\frac{dw}{dz} \frac{dz}{dw} = 1 \quad \frac{dw}{dz} = \frac{1}{dz/dw} \quad (21)$$

Considering this result, it is apparent that for every point w in D' , the one-to one analytic map $f(w)$ has a nonzero derivative, and is therefore a conformal map. Indeed, this simple derivation shows that all one-to-one analytic functions meet the criteria for a conformal map. Further derivations involving some tedious but standard calculus readily show that, for a real-valued harmonic function $u(x,y) = u(z)$ on a domain D in the z -plane, as long as the mapping function $z = f(w)$ is analytic and maps D onto another domain D' in the w -plane, the real-valued composition function $h(w) = u(f(w))$ is also harmonic on D' [ref. 23].

On this substantive mathematical foundation, the utility of conformal mapping and complex analysis in the solution of electrostatic problems becomes clear, opening the way to real applications in engineering research. Before taking the steps to the actual application of these findings, however, a special method for deriving mapping functions, useful in the solution of a large number of boundary value problems, must be explained. Without a means to systematically select complex functions tailored to transform a difficult boundary value geometry to a defined geometry with a known solution, the mathematical implications of the preceding sections are moot. Schwarz-Christoffel mapping offers just such a method.

2.4 Schwarz-Christoffel Mapping

Independently derived by Schwarz and Christoffel in the mid-1800's, the Schwarz-Christoffel integral defines a conformal mapping from the upper-half complex w -plane onto a polygonal region in the complex z -plane. Solving the Schwarz-Christoffel integral results in a complex mapping function which transforms the upper-half w -plane to a prescribed polygon geometry in the z -plane. In later chapters, application of the Schwarz-Christoffel integral method allows for the transformation of the complicated boundary value problem representing the electrostatic physics of the MFC to a tractable geometry.

In the interest of simplicity, the mathematical proofs and derivations of the Schwarz-Christoffel mapping technique are avoided in the following section, but the assertions of the properties of the mapping functions presented hold in conjunction with established theory. References [11, 23, 31] contain extensive information regarding the theory behind Schwarz-Christoffel integrals. The one-to-one complex mapping function

$$\begin{aligned} z = f(w) &= k(w - w_0)^{\frac{1}{n}} + z_0 \quad \Rightarrow \\ z - z_0 &= k(w - w_0)^{\frac{1}{n}} \end{aligned} \tag{22}$$

maps the upper-half w -plane (domain D') onto a sector of angle π/n in the z -plane (domain D), where k and n are constants and w_0 and z_0 are constant points in their respective complex planes. Figure 8 illustrates the mapping properties of equation (22).

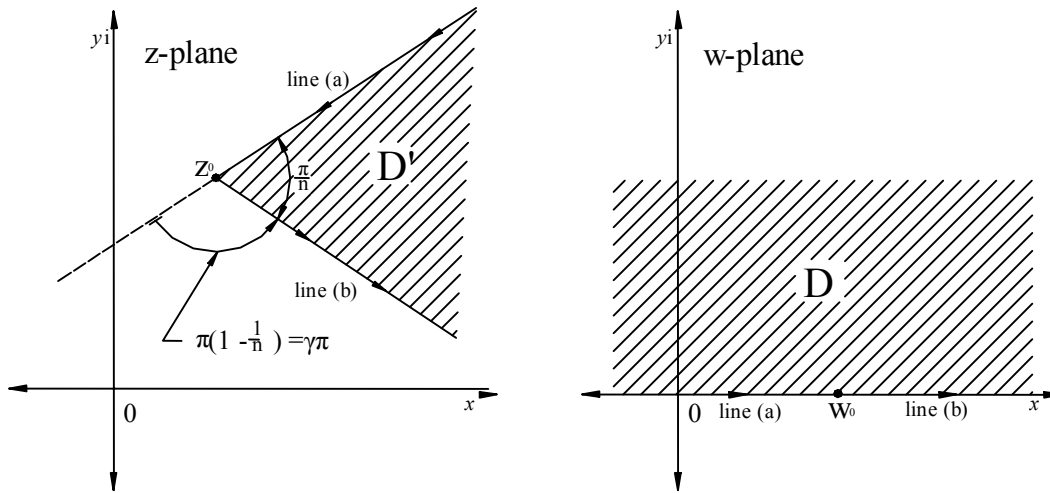


Figure 8: The mapping properties of equation (22) as it maps points between two complex domains.

Equation (22) transforms a defined sector of the z -plane to the entire upper-half w -plane.

Point w_0 in the w -plane corresponds to point z_0 in the z -plane, and both represent the respective “origin” of each domain. Taking the derivative of equation (22) yields

$$\frac{dz}{dw} = \frac{k}{n} (w - w_0)^{(1/n - 1)} \quad (23)$$

Inspection of equation (23) readily reveals that the function $f(w)$ is analytic except at $w = w_0$ for $n > 1$ and at $w = \infty$ for $n < 1$. At $n = 1$, equation (22) simplifies to a linear complex function. Augmenting the boundary of domain D through the inscription of an infinitesimally small circle about w_0 serves to alleviate the problems associated with non-conformality at w_0 , effectively excluding the singularity from the mapped domain. These results confirm that $f(w)$ is conformal between domains D and D' .

Analyzing the geometric behavior of the map defined by equation (22) through inspection of figure 8, several interesting aspects emerge. Equation (22) maps the real axis of the w -plane to the edge of D' , implying that the boundary of domain D' corresponds to the boundary of domain D . As a hypothetical point, P , moves along a

segment (a) of the boundary of D' in the z -plane, its image in the w -plane simultaneously moves along segment (a) of the real axis. Figure 8 indicates this direction of progression in both planes by arrows along the domain boundaries. Point P and its corresponding image both approach the origins of their respective domains simultaneously (points z_0 and w_0), and both pass through these points concurrently. After P travels through z_0 , the direction of progression of point P along the boundary of D' changes by an angle of π/n , where n corresponds to equation (22). Point P then continues to move in the z -plane along boundary segment (b) as its image continues to travel along the real axis in the w -plane along the image boundary (b). Concisely quantifying the direction change of the path of P , the factor γ multiplies π radians to indicate the change in the angle of progression of P in radians, with positive angles measured in the counter-clockwise direction. Thus, $\gamma = 1/2$ would indicate an angular change of 90° in the counter-clockwise direction.

An intuitive analysis of the mapping function (22) suggests that the mapped domain D in the z -plane may be interpreted as a single vertex of a larger polygonal boundary. Extrapolating from the form of equation (23), the derivative form of the Schwarz-Christoffel mapping function arises

$$\frac{dz}{dw} = C(w - w_1)^{-\gamma_1} (w - w_2)^{-\gamma_2} \dots (w - w_\mu)^{-\gamma_\mu} = C \prod_{(\alpha)} (w - w_\alpha)^{-\gamma_\alpha} \quad (24)$$

where the constants w_α correspond to the preimage vertices of a polygon in the z -plane, C is a constant specifying a scale and rotation factor and the constants γ_α represent the pi-multiplier of the angle change for each vertex of the z -plane polygon.

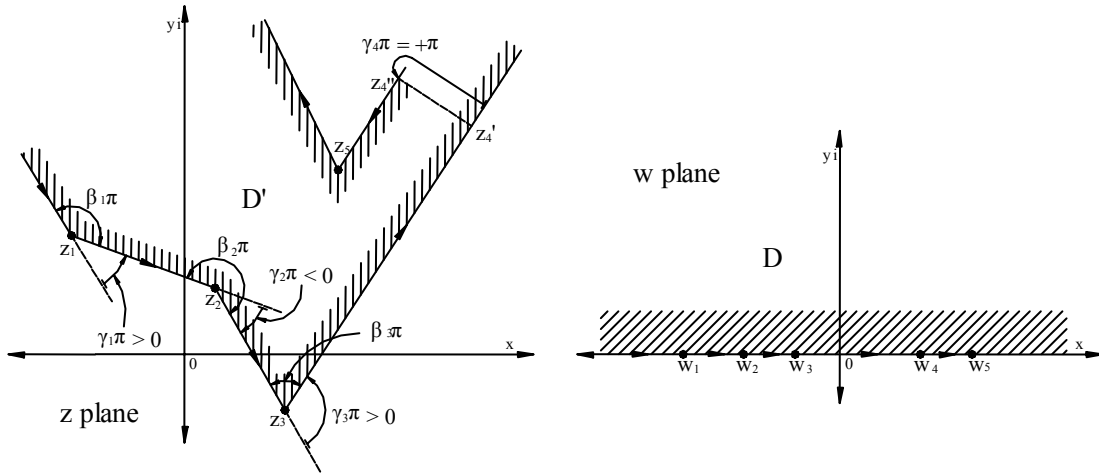


Figure 9: The generic mapping properties of equation (25) as it maps points between two complex domains. Equation (25) transforms the interior of a defined polygon in the z -plane to the entire upper-half of the w -plane.

Although it serves as the preliminary mathematical framework to systematically determine conformal mapping functions with specific properties, equation (24) has little practical use. Integration of equation (24) results in the Schwarz-Christoffel integral

$$z = f(w) = C \int \prod_{(\alpha)} (w - w_{\alpha})^{-\gamma_{\alpha}} dw + C_1 \quad (25)$$

where C_1 is a constant of integration that essentially locates the origin of the mapped domain. If solved, the Schwarz-Christoffel integral yields an expression for a unique conformal mapping function, capable of transforming a given polygon geometry to the upper-half plane. Sets of vertex coordinates define the polygon domain geometry of the z -plane, but, because of the properties of the complex plane, polygon vertices may lie at infinity, which is a valid point in the complex plane. Point z_5 in figure 9 illustrates a complex point at infinity, where the change in angle of progression of the map equals π or a full 180° rotation. Allowances for such abstractions enable the mapping of very unconventional polygon domains, where some angles comprise parallel edges that “meet” at infinite distances and open borders. Solving equation (25) demands the integration of

the geometrically mandated form of the integrand along with the calculation of the unknown constants C and w_α . Simplifying the determination of the constants w_α , three image vertices in the w -plane may be arbitrarily selected to correspond to specific vertices in the z -plane. Prudent specification of these constant values often simplifies the final form of the integrand in equation (25), ameliorating the solution process.

Depending on the shape of the mapped z -plane polygon domain, the Schwarz-Christoffel integral might not have a solution in the form of an elementary function. Along with this obstacle, the primary difficulty in solving the Schwarz-Christoffel integral consists of determining the constants C and C_l , as well as identifying three points in the w -plane to correspond to three selected vertices in the z -plane. Requirements on vertex selection follow from the Riemann mapping theorem and its corollaries, which show that the specification of three image points on the w -plane for three vertices in the z -plane fully prescribes a unique Schwarz-Christoffel conformal map $z = f(w)$. Consequently, the selection of three image points for three vertices dictates the values for the constants C and C_l and the remaining unspecified images of the other vertices.

Consideration of the systematic, generalized procedure to determine a Schwarz-Christoffel mapping function readily evinces the power of the Schwarz-Christoffel technique. Any electrostatics potential problem with boundary conditions expressible as a complex polygon may be mapped, at least in theory, to a simpler upper-half plane geometry exhibiting soluble boundary conditions. Obtaining a solution for the original problem then becomes a systematic exercise of transforming the w -plane solution back to the original system geometry.

2.5 Potential Solutions in the Complex Plane

Of course, without mathematics to express and determine potential solutions in complex form, the fabrication of a complex mapping function is irrelevant. Mentioned previously, harmonic functions are invariant under conformal mapping, so given potential solutions expressed in mathematics compatible with complex analysis, a potential

solution in one domain also gives the solution for its image domain. Potential solutions to boundary value problems in the complex plane may be written in complex form as

$$P(w) = \Phi(u, v) + j\Xi(u, v) \quad (26)$$

where $P(w)$ is a complex potential function in the w -plane, dependent on the complex variable w . Obeying the convention of equation (13), w comprises two real variables, u and v .

$$w = u + iv \quad (27)$$

The real part of the complex potential function, $\Phi(u, v)$, represents the actual potential solution to the boundary value problem, while the imaginary portion, $\Xi(u, v)$, is the electric flux function for the boundary value problem. Thus, at every w -plane point on a complex domain defining a potential boundary value problem, $P(w)$ provides a specific scalar value corresponding to the electric potential at w , as well as a scalar value for the electric flux. Of course, since $\Phi(u, v)$ depends only on real variables, the potential solution may also be plotted on the real, two dimensional u - v plane, equating u with x and v with y . The real and imaginary parts of the complex potential function, or the potential and flux solutions, are conjugate functions in the complex plane, and form sets of orthogonal curves in the w -plane.

Taking the gradient of Φ in the real u - v plane yields two partial derivative equations, which, by equation (3), expresses the electric field.

$$\begin{aligned} -E_u &= \frac{\partial \Phi}{\partial u} \\ -E_v &= \frac{\partial \Phi}{\partial v} \end{aligned} \quad (28, 29)$$

Rewriting equations (28) and (29) in complex form and applying the Cauchy-Riemann

equations (14) and (15) results in the complex expression for the electric field solution.

$$E(w) = E_u + iE_v = -\frac{\partial\Phi}{\partial u} + i\frac{\partial\Xi}{\partial u} \quad (30)$$

The analyticity of $P(w)$ guarantees a direction independent derivative of $P(w)$ at any point in the defined problem domain, meaning that the derivative at a point w in the complex plane doesn't vary in relation to the direction of approach to w . Since the derivative of $P(w)$ at an arbitrary point w is the same whether w is approached from the u direction (0°) or an arbitrary direction w , equation (30) relates to the complex derivative of $P(w)$ through the equation

$$\frac{dP(w)}{dw} = \frac{dP(w)}{du} = \frac{\partial\Phi}{\partial u} + i\frac{\partial\Xi}{\partial u} \quad (31)$$

By the result of equation (31), equation (30) may be written as

$$E(w) = -\overline{\left(\frac{dP}{dw}\right)} \quad (32)$$

Equation (32) offers a formula to determine the complex electric field of a system from the complex potential solution of that system in a defined complex domain. Comparison of equation (32) with the equivalent expression given by equation (30) reveals that the electric field values provided by application of equation (32) are complex, enforcing the interpretation of these values as vector quantities given in the explanation of equations (10) and (11). By way of this concept, equation (32) actually yields a vector result at every point w in the problem domain, equating the y -direction field (E_u) with the imaginary component of the complex result and the x -direction field (E_v) with the real portion. Synthesis of these resolved u - v components via equations (10) and (11) produces the magnitude and direction of the electric field vectors, \underline{E} , originating at unique points w in the complex plane.

Quite purposefully, the previous equations express complex electric field and potential solutions in the w -plane. Combining these ideas with the concepts of conformal mapping enables the development of equations to transform potential and electric field solutions between complex domains related by mapping functions. Assume that, as discussed previously, w relates to z on a specified domain through the invertible conformal map $z = f(w)$. Obviously, the potential value of each point w is identical to the potential of each corresponding image point, z . Therefore, analytically determining the potential function for the image domain in the z -plane is a simple process of substitution

$$\begin{aligned} P(w) &= P(f^{-1}(z)) \Rightarrow \\ P(z) &= P(f^{-1}(z)) \end{aligned} \quad (33)$$

Via the replacement of w with the inverse mapping function, the potential solution becomes a function of z and articulates the potential field in the z -domain. Commonly, the Schwarz-Christoffel mapping function $z = f(w)$ has no analytically derivable inverse, and exact numerical methods are the only recourse for determining a point w for a given image point z . Indeed, the lack of closed-form inverse formulas for most complicated Schwarz-Christoffel maps leads to one of the important computational issues associated with solving electrostatics problems with conformal mapping techniques.

Finding the electric field in the z -plane from the w -plane solution is slightly more complicated than the case of the potential field. Combining the result of equation (32) and the derivative of the inverse conformal mapping function produces a formula for the transformed electric field solution in the z -plane

$$E(z) = -\overline{\left(\frac{dP}{dz}\right)} = -\overline{\left(\frac{dP}{dw} \frac{dw}{dz}\right)} \quad (34)$$

Implicit derivation of the conformal mapping function readily yields the derivative of w with respect to z , assuming algebraic rules suffice to separate z and w terms in the resulting differential equation.

Armed with the complex formulas and relations for the electric and potential fields of a system expressed in the complex plane, the full power of conformal mapping theory comes to light. Successful implementation of Schwarz-Christoffel techniques can reduce the geometry of an intractable boundary value problem posed in the complex plane to an equivalent problem having the most basic complex potential solution, often inferable by mere inspection. With the results developed in the previous subsection, a complex potential solution readily provides electric field equations in the simplified domain, and both the potential and electric field solutions easily translate back to the original problem geometry through a few rudimentary equations. Bringing this analytical scheme to bear on the MFC problem, the next chapter addresses the solution of the dual-IDE electrostatics problem.

Chapter 3

Electrostatics Modeling

3.1 IDE Model

Prior to the execution of a mathematical analysis of the electrical behavior of the MFC, it is necessary to construct an accurate model of the physics of the dual-IDE structure. Without the guarantee of a representative physical model for a basis, any analytical expression characterizing the MFC becomes irrelevant, as it would correspond to a different physical system. Devoting attention to this concern, a first principles, physics oriented analysis of the dual-IDE structure was conducted under the guidance of established electrostatic laws, resulting in a sufficiently accurate model.

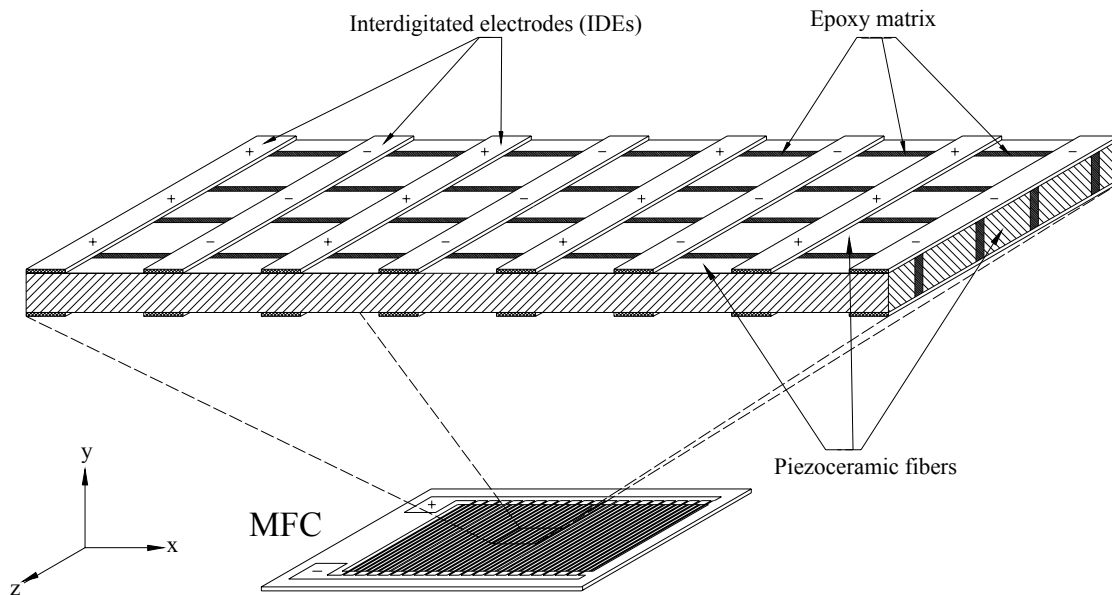


Figure 10: Schematic of the repeating structure of the MFC. This picture shows a magnified internal portion of the MFC

A schematic depiction, figure 10 illustrates the regularly repeating geometry of the MFC dual-IDE system. As shown in the figure, the IDE structure comprises two opposing “banks” of electrodes alternating in polarity which sandwich piezoceramic fibers. Logically, the term interdigitated electrode itself originates from these evenly spaced, oppositely polarized electrode fingers. Actual operation of the MFC involves the application of a differential voltage across the two electrode terminals at which individual IDE fingers of common polarity connect. Due to this globally imposed electrical boundary condition, the voltage of each IDE finger is actually constant along the entirety of each finger and of either a positive or negative value. Along with the material properties and physical structure of the MFC, the condition of fixed voltages along the IDEs constitutes the only trivial information on the MFC electric field problem. All other data, including the form of the IDE electrical and potential fields, must be calculated based on this “given” information. Since fixed voltage values in specific locations govern the physics of the IDE problem, it fits the form of a potential boundary value problem, where the boundary conditions correspond to fixed voltage values and potential field gradient conditions based on problem symmetry.

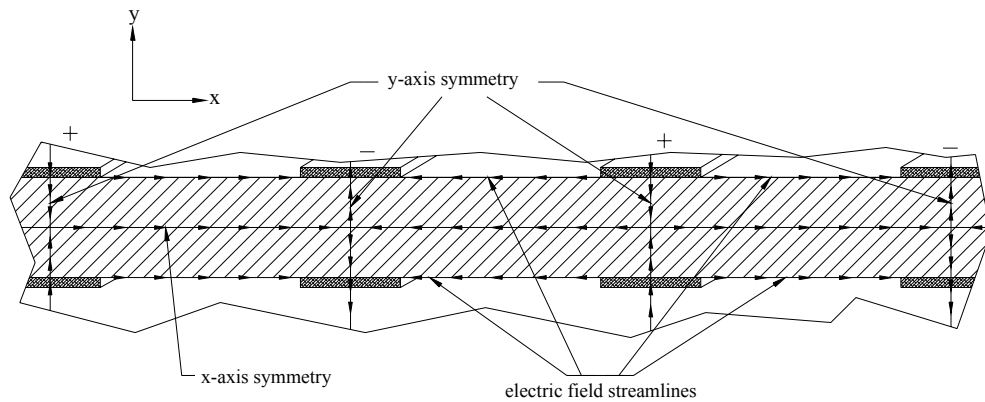


Figure 11: Illustration of the symmetry inherent to the MFC. The arrowed lines in this diagram, a cross-sectional schematic of an MFC piezoceramic fiber, indicate lines of geometric symmetry which correspond to the direction of flux lines in the electrical field of the MFC.

Examination of the potential boundary values of the system in conjunction with the system geometry immediately reveals symmetry conditions which both complete the

specification of the problem boundary conditions and decompose the overall system into a matrix of repeating unit cells exhibiting identical physical behavior. Assuming an infinite MFC size simplifies the problem analysis by effectively ignoring the influence of edge effects at the actual physical ends of an MFC. Under this reasonable idealization, two planes of symmetry exist for each pair of equipotential electrodes. Shown in figure 11, one plane exists parallel with the length of the piezoelectric fibers and halfway between the opposing banks of IDEs. Along this plane located at half the distance between the opposing IDE banks, an unstable y -direction electric field equilibrium occurs because all points in this locus are positioned equidistant from equipotential boundaries, forming an x -axis symmetry. Hypothetical charges in this plane experience only x -direction forces, a physical condition which corresponds to an electric vector field with no y -component. Mathematically, this condition relates to a zero-valued partial derivative of the potential field in the y -direction. Perpendicular to the piezoelectric fibers, another symmetry plane intersects the midpoints of opposing equipotential electrode pairs (fig. 11). On both sides of this plane, the potential values of the MFC IDEs repeat in the same pattern and balance the x -direction EMFs experienced by a test charge in the plane, resulting in no net x -direction electric force. Thus, a zero-valued x -direction electric field characterizes this locus, and only y -direction electric field vectors develop at points in this plane. In the context of the potential field problem, the mathematical equivalent of this plane of symmetry is a zero-valued gradient of the potential field in the x -direction. According to the mathematical jargon of boundary value problems, the terminology for a constant gradient boundary condition is a Neumann boundary condition. A Dirichlet boundary condition refers to a constant value along a domain boundary.

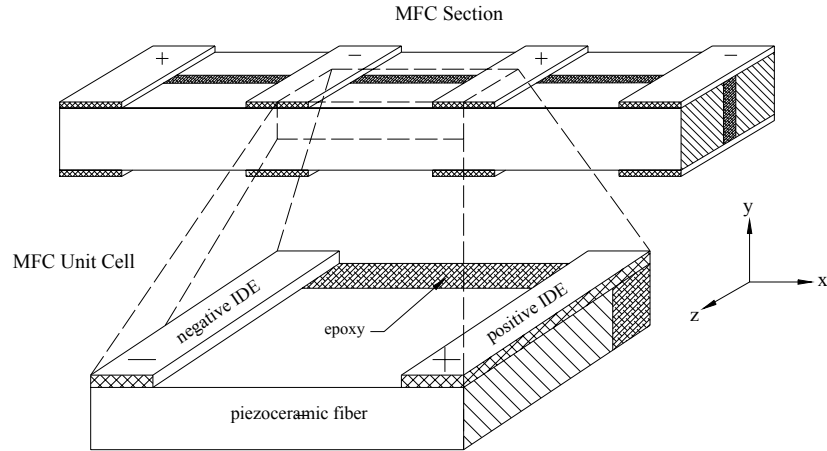


Figure 12: Schematic illustration of the 3-D MFC unit cell. The unit cell edges correspond to lines of electric field symmetry and geometrically repeating material interfaces in the internal MFC structure.

Having gleaned this secondary information from the system geometry, a basic unit cell encapsulating the complete boundary characteristics of the MFC potential field problem may be constructed. Separated in two dimensions by the previously described planes of symmetry and the planes containing the IDE banks, this unit cell represents the mathematical domain of the MFC potential field problem as well as a physically repeating unit in the MFC structure. Figure 12 provides a schematic depiction of the MFC unit cell in three dimensions, showing how the physical boundaries of the cell correlate to the boundary conditions of the mathematical potential problem.

Along with the electrical field symmetry conditions, physical interfaces between the material constituents of the MFC mark the unit cell boundaries along the z -axis. While the form and direction of the electrical field of the MFC unit cell is uniform along the z -axis, the varying electrical permittivity of the materials composing the MFC alter the strength of the electrical field by a constant between different materials. Thus, the electrical field in the piezoceramic fibers is much stronger than the electrical field in the intervening epoxy matrix. Without varying material properties along the z -axis, the MFC unit cell would not be three dimensional, and would only possess x -direction and y -direction boundaries along electrical field lines

Although, in reality, the MFC unit cell is three-dimensional, the MFC unit cell electrical field is safely analyzed in two-dimensions because only field intensity varies with the z -direction, and by a constant at an instantaneous dielectric boundary. Figure 13 illustrates the MFC unit cell in two dimensions. For the remainder of this derivation, all references to the MFC unit cell refer to the 2-D unit cell shown in figure 13, which is merely a planar section of the 3-D unit cell in the x - y direction. Every repeating 2-D unit cell in the MFC possesses a specific and identical potential field, electric field, piezoelectric polarization field and capacitance based on the geometry of the dual IDEs. Thus, determining the electrostatic properties of the unit cell automatically defines the electrostatic properties of the aggregate MFC. Verifying this formulation of the MFC unit cell, previous finite element models of AFCs and MFCs employed an identical set of assumptions to arrive at equivalent unit cell structures [ref. 5].

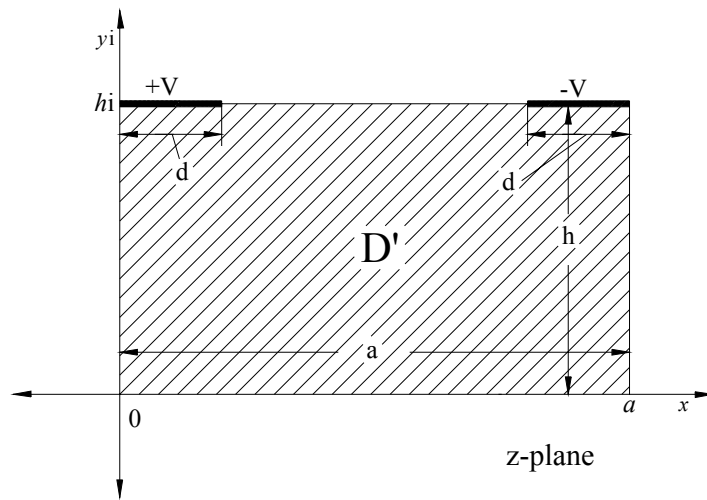


Figure 13: Plot of the uniform 2-D face of the MFC unit cell in the complex plane.

Plotting the MFC unit cell in the complex plane completes the translation of the electrostatic physics of the MFC into a mathematical form, fully elaborating on the parameters of the potential problem. In this interpretation of the MFC unit cell, the boundaries of the cell and their associated properties correspond to specific points along lines in the complex plane, specifying the mathematical boundary conditions for the

problem. Similarly, the interior of the cell translates into a rectangular-shaped domain in the complex plane, qualifying the unit cell potential problem for analysis using the techniques of Schwarz-Christoffel conformal mapping.

3.2 Schwarz-Christoffel Mapping Solution

Finding a complex analysis solution to the electrostatic potential problem posed by the MFC unit cell obviously involves mapping the rectangular domain of the unit cell to a simple domain with a known electrostatics solution. Construction of the Schwarz-Christoffel integral for a rectangular domain with a specific aspect ratio begins with numbering the four vertices of the closed polygon in a counter-clockwise progression.

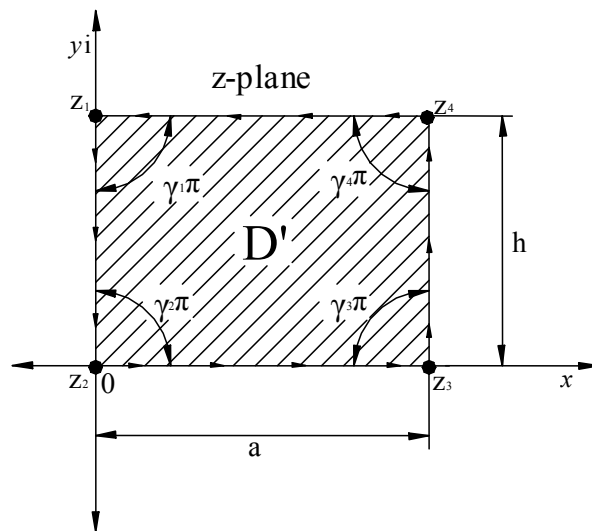


Figure 14: An arbitrary rectangular domain plotted in the complex z -plane. Polygon vertices are sequentially labeled along with the pertinent angles of perimeter directional change.

Pending this labeling, the visualization of an imaginary point progressing along the boundary of the domain from vertex one to four helps to identify the angular direction change of the perimeter after each vertex. For this case, the path of the polygon boundary changes by a value of 90° , or $\pi/2$ radians, after every vertex. Thus, in the conventions of the Schwarz-Christoffel technique, $n = 2$ for each vertex, giving all of the vertices a γ

value of $\frac{1}{2}$. Substituting these geometrically dictated γ values into the general form of the Schwarz-Christoffel integral (eqn. (25)) results in an integral of the form

$$z = f(w) = C \int_0^w \frac{1}{(w-w_1)^{1/2}(w-w_2)^{1/2}(w-w_3)^{1/2}(w-w_4)^{1/2}} dw \quad (35)$$

From inspection of the integrand of equation (35), it is evident that for any four choices of the values of the w -plane image vertices w_α , no integral solution exists in terms of elementary functions. At this juncture, the introduction of a class of exotic but well-defined functions called elliptic functions opens a course of action for integrating equation (35). Proposed at the turn of the 20th century as a solution for certain types of integrals, elliptic functions enjoyed wide study by mathematicians in ensuing decades. A precise definition of the incomplete elliptic function of the first kind, a specific type of elliptic function, follows from equation (36)

$$F(k, x) = \int_0^x \frac{1}{(1-x^2)^{1/2}(1-k^2x^2)^{1/2}} dx = \int_0^x \frac{1}{\sqrt{(1-x^2)(1-k^2x^2)}} dx \quad (36)$$

where $F(k, x)$ is an incomplete elliptic function of the first kind, x is a real or complex-valued independent variable and k is a real-valued constant referred to as the elliptic modulus. Choosing a value for k fully defines an incomplete elliptic function of the first kind for any value of x , and volumes of tabulated data exist which give the values of incomplete elliptic functions of the first kind for various combinations of k and x . Since the advent of the computing age, various algorithms to determine the value of elliptic functions for both real and complex independent variables have also been developed, making computations involving elliptic functions simple and convenient.

Comparisons of the form of equations (35) and (36) reveal blatant similarities in the structures of the integrands in both formulas. Extending this insight, it is apparent that clever choices for the values of the constants w_α force equation (35) to fit the exact

form of the incomplete elliptic integral of the first kind (eqn. (36)). Selecting values of $1/k$, -1 , 1 and $1/k$ for w_{1-4} , respectively, and substituting them into equation (35) yields

$$z = f(w) = C \int_0^w \frac{1}{\left(w - \frac{1}{k}\right)^{1/2} \left(w + \frac{1}{k}\right)^{1/2} (w-1)^{1/2} (w+1)^{1/2}} dw \quad (37)$$

Rearranging equation (37) results in the integral definition of an incomplete elliptic function of the first kind, multiplied by the elliptic modulus, k (eqn. (38)).

$$\begin{aligned} z = f(w) &= C \int_0^w \frac{1}{\sqrt{\left(w - \frac{1}{k}\right)\left(w + \frac{1}{k}\right)} \sqrt{(w-1)(w+1)}} dw \\ &= C \int_0^w \frac{k}{\sqrt{(k^2 w^2 - 1)} \sqrt{(w^2 - 1)}} dw \\ &= Ck \int_0^w \frac{1}{\sqrt{(1 - k^2 w^2)(1 - w^2)}} dw \end{aligned} \quad (38)$$

Thus, choosing special values for the w -plane vertices facilitates the solution of the Schwarz-Christoffel integral for a rectangular domain by identifying its form with the form of an incomplete elliptic integral of the first kind. Solving equation (38) with knowledge of the incomplete elliptic function of the first kind produces the mapping function to transform a rectangular complex domain to the upper-half complex plane (w -plane).

$$z = f(w) = Ck \int_0^w \frac{1}{\sqrt{(1 - k^2 w^2)(1 - w^2)}} dw = CkF(k, w) + C_1 \quad (39)$$

By the tenets and theorems of Schwarz-Christoffel mapping theory, the incomplete elliptic function of the first kind is conformal at all points in the z -plane rectangular domain, except the vertices. Choosing to identify four specific values with

the image vertices in the w -plane does not violate the Riemann mapping theorem, since only two image vertices are given the deterministic values of 1 and -1. The other two w -plane vertices, located at $-1/k$ and $1/k$, take on values dependant on the elliptic modulus k , which holds a value based on the aspect ratio of the rectangular domain in the z -plane. Accordingly, only two image vertex values are mandated, with the two other values derived on the basis of domain geometry. Table 2 summarizes the outcome of the Schwarz-Christoffel mapping of a rectangular domain with a list of the pertinent values associated with each mapped vertex of the rectangle.

Vertex	z -plane Value	w -plane Value	Angle of Progression Change	γ
1	ih	$-1/k$	$\pi/2$	$1/2$
2	0	-1	$\pi/2$	$1/2$
3	a	1	$\pi/2$	$1/2$
4	$a + ih$	$1/k$	$\pi/2$	$1/2$

Table 2: Important vertex quantities used in the Schwarz-Christoffel mapping of an arbitrary rectangular domain.

Calculation of the elliptic modulus, k , of the elliptic mapping function is possible through consideration of the distance between two vertices in the z -plane. Using the conventions of figure 14, a denotes the distance between the vertices z_2 and z_3 . From the Fundamental Theorem of Calculus and the governing equation of the Schwarz-Christoffel mapping function for a rectangular domain, the definite Schwarz-Christoffel integral between the limits of the w_2 and w_3 is equivalent to a distance of a .

$$\begin{aligned}
 z_3 - z_2 &= f(w_3) - f(w_2) = a \\
 f(w_3) - f(w_2) &= Ck \int_{-1}^1 \frac{1}{\sqrt{(1-k^2w^2)(1-w^2)}} dw \quad (40)
 \end{aligned}$$

Exploitation of the symmetry of the w -plane geometry allows equation (40) to be

equivalently written as equation (41).

$$a = 2Ck \int_0^1 \frac{1}{\sqrt{(1-k^2w^2)(1-w^2)}} dw \quad (41)$$

The form of the integral in equation (41) corresponds to the definition of the complete elliptic function of the first kind, $K(k)$. As with incomplete elliptic functions of the first kind, many numerical algorithms and bodies of data exist which give the values of the complete elliptic function, which depends only on k , for different elliptic moduli.

$$K(k) = \int_0^1 \frac{1}{\sqrt{(1-k^2w^2)(1-w^2)}} dw \quad (42)$$

$$a = 2CkK(k)$$

Although this result offers an equation relating the width of the mapped rectangular domain to the elliptic modulus, the presence of an extra unknown constant, C , obstructs the isolation of a value for k . Circumventing this difficulty, the relationship of the height of the rectangular domain to the Schwarz-Christoffel integral is examined. Namely, the distance between vertices z_2 and z_3 , jh , is mathematically equivalent to the definite Schwarz-Christoffel integral in equation (43).

$$jh = kC \int_1^{\frac{1}{k}} \frac{1}{\sqrt{(1-k^2w^2)(1-w^2)}} dw \quad (43)$$

Applying the Fundamental Theorem of Calculus to equation (43) and introducing the complementary elliptic modulus, k' , leads to equation (44).

$$jh = kC \left(F\left(k, \frac{1}{k}\right) - F(k,1) \right) = jkCK(k')$$

where

$$F\left(k, \frac{1}{k}\right) = K(k) + jK(k')$$

$$k' = \sqrt{1 - k^2}$$
(44)

Rearranging equation (42) to solve for C and substituting the result into equation (44) yields an equation strictly in terms of the elliptic modulus and the dimensions of the rectangular domain.

$$C = \frac{a}{2kK(k)} \Rightarrow \frac{a}{2h} = \frac{K(k)}{K(k')} \quad (45)$$

Equation (45) shows that the ratio of the width of the z -plane rectangular domain to its height uniquely determines the elliptic modulus of the elliptic mapping function. A value for the constant C also follows from the solution of the elliptic modulus by means of equation (42). Unfortunately, due to the lack of an inverse for the complete elliptic function of the first kind, no simplification of equation (45) facilitates the direct analytical solution of k , requiring the use of numerical solver algorithms.

Completion of the Schwarz-Christoffel mapping function also requires the calculation of the constant of integration C_1 . Once again, inspection of the symmetry of D' evinces that the point $z = a/2$ is the image of $w = 0$. Substituting these values into equation (39) solves for C_1

$$z = CkF(k, w) + C_1$$

$$\frac{a}{2} = CkF(k, 0) + C_1 \Rightarrow C_1 = \frac{a}{2} \quad (46)$$

Combined with the result of equation (39), the values for k and C produced by equations (42) and (45) and the value of C_I fully describe the Schwarz-Christoffel mapping function for an arbitrary rectangular domain to the upper-half w -plane

$$z = \frac{a}{2K(k)} F(k, w) + \frac{a}{2} \quad (47)$$

where a depends on the problem geometry and k is generated by equation (45).

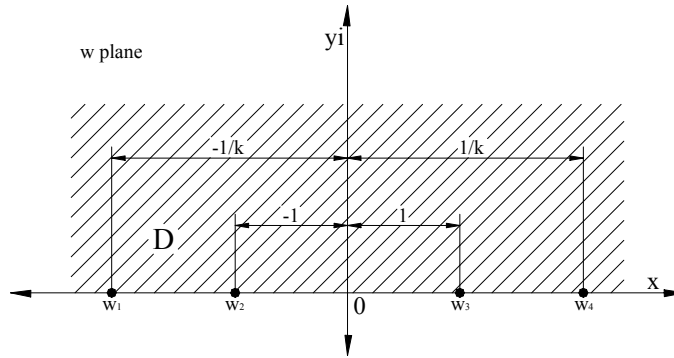


Figure 15: The mapped geometry of an arbitrary rectangular domain operated on by equation (47). Mapped rectangle vertices are labeled along with their distance from the imaginary axis, and the mapped domain corresponds to the entire upper-half w -plane.

Figure 15 provides an illustration of the geometry of the upper half w -plane under the mapping effects of equation (47). Vertex labeling corresponds to the labeling of figure 14, evincing the correspondence of the critical points in each complex domain. Comparing the z -plane and w -plane domains reinforces an important property of the mapping between the two regions. Holding important implications for the solution of potential boundary value problems, the correspondence of the w -plane real axis to the perimeter of the z -plane rectangle domain is a very pertinent feature of the elliptic mapping function. Segments of the real axis demarcated by the vertex images w_a correspond to individual sides of the z -plane rectangle. For example, the left side of the z -plane domain maps to the real axis in the w -plane between w_1 and w_2 . In this fashion,

perimeter sections falling between pairs of z -plane vertices correspond to the w -plane real axis sections located between the mapped images of the vertex pairs. Due to this geometric correlation, precise segments of the w -plane real axis share the boundary conditions of different sides of the z -plane domain.

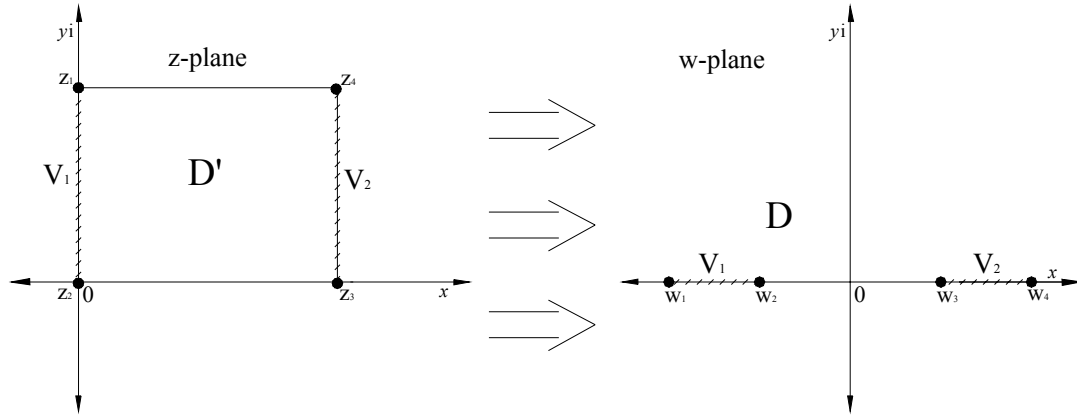


Figure 16: Illustration of the correspondence of domain boundaries between the z -plane and w -plane under the mapping properties of equation (47).

Assigning a constant high potential value to the right side of the z -plane domain and a constant low potential to the left side, the complex solution for the potential field within the z -plane domain is a trivial linear equation.

$$P(z) = V_1 - \frac{(V_1 - V_2)}{a} z \quad (48)$$

In equation (48), V_1 is the constant potential value (Dirichlet boundary condition) of the left side of D' , V_2 equals the potential value of the right side of D' (Dirichlet boundary condition) and a equals the width of D' . Intuitively correct in its simplicity, equation (48) is harmonic for the stated boundary conditions in the defined z -plane domain, since it solves the stated potential boundary value problem on the domain. Identical to the simplified (ignoring fringing) potential solution for a parallel plate capacitor, equation (48) implies that the top and bottom boundaries of the z -plane domain exhibit Neumann

boundary conditions, with the potential field varying constantly in the real direction. Indeed, taking the derivative of equation (48) shows that, under the prescribed boundary conditions, the complex potential field varies constantly with z across the entire domain.

$$\frac{dP}{dz} = \frac{d}{dz} \left(V_1 - \frac{(V_1 - V_2)}{a} z \right) = \frac{(V_1 - V_2)}{a} \quad (49)$$

Of course, applying equation (32) to this expression gives the complex form of the electric field produced by the parallel potential surfaces on either side of D' .

$$\begin{aligned} E(z) &= -\overline{\left(\frac{dP}{dz} \right)} \\ E(z) &= \frac{(V_1 - V_2)}{a} \end{aligned} \quad (50)$$

Intuitively correct, equation (50) mathematically states that the electric field magnitude of the uniform parallel plate problem is invariant with respect to z and points in the positive x -direction, identifying the real component of the complex electric field equation with the x -coordinate (eqn. (7)). A direct algebraic analysis of the parallel plate problem using first principles produces the same outcome.

Due to the invariance of harmonic solutions under conformal mappings, the potential and electric field values at points in the z -plane domain are identical for the image points in the w -plane. Applying this fact and the previously expounded relationships between the w -plane real axis and z -plane domain perimeter, the potential solution for the z -plane may be interpreted as the potential solution for coplanar strips after transformation to the w -plane. Solved above for the z -plane domain, the boundary value problem of parallel equipotential surfaces transforms to the w -plane as a coplanar strip boundary value problem under equation (47). Results from Chapter 2 enable the calculation of the potential field for the coplanar strip boundary value problem based on the solutions for the uniform parallel plate boundary value problem in the z -domain.

Direct substitution of the Schwarz-Christoffel mapping function for z into the potential solution for the z -plane yields the potential solution for the w -plane

$$\begin{aligned}
 P(z) &= V_1 - \frac{(V_1 - V_2)}{a} z \\
 P(z) = P(f(w)) &= P\left(\frac{a}{2K(k)} F(k, w) + \frac{a}{2}\right) = V_1 - \frac{(V_1 - V_2)}{2K(k)} F(k, w) - \frac{(V_1 - V_2)}{2} \\
 P(w) &= -\frac{(V_1 - V_2)}{2K(k)} F(k, w) + \frac{(V_1 + V_2)}{2}
 \end{aligned} \tag{51}$$

Despite the clear utility of the previous Schwarz-Christoffel mapping results in this study, the solution of the MFC potential problem requires embellishment on the mapping procedures explained thus far. Difficulties related to the boundary conditions of the MFC unit cell necessitate an extra mapping step in order to transform the problem to a domain with a known solution. Notably, the equipotential boundary segments of the MFC unit cell do not correspond to the equipotential surfaces of the simple parallel plate problem, occurring along the top boundary of the unit cell's rectangular domain instead of the two sides. Compounding the dissimilarities between the two problems, the boundary conditions along the top edge of the MFC unit cell are mixed, with a Neumann boundary condition intervening between the two Dirichlet boundary conditions of the electrodes.

Again, conformal mapping techniques overcome these obstacles. Using equation (47) to map the unit cell domain and boundary conditions to the upper half w -plane produces a boundary value problem not vastly dissimilar to that of the coplanar strip problem addressed previously. Figure 17 illustrates the labeled vertex geometry of the unit cell in the z -plane, while figure 18 shows the corresponding geometry of the w -plane under the mapping of equation (47).

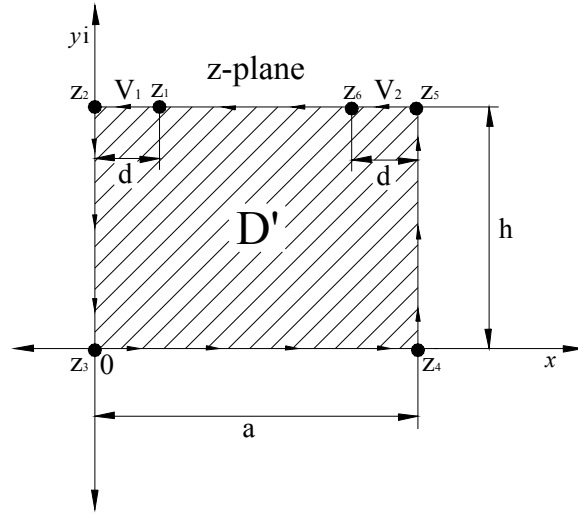


Figure 17: The mathematical interpretation of MFC unit cell geometry in the complex z -plane. Important MFC unit cell vertices are labeled, along with the geometry-defining dimension variables.

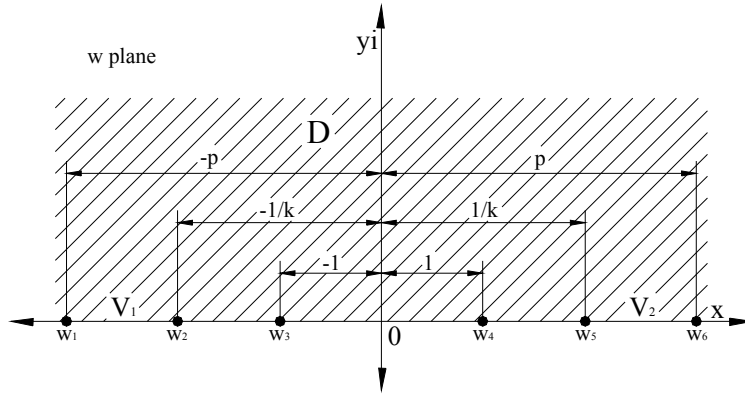


Figure 18: The MFC unit cell mapped to the complex w -plane through equation (47). Corresponding w -plane vertices are labeled, along with their distance from the imaginary axis.

While the mapping of the rectangle corners under equation (47) produces the same pairings between z -plane and w -plane points as the standard coplanar strip problem, two extra critical points demarcating the limits of the alternating IDE equipotential surfaces map to the w -plane as points at p and $-p$. Table 3 catalogues the mapping of the vertices and critical points of the IDE unit cell problem between the z -plane and w -plane.

Vertex / Critical Point	z -plane Value	w -plane Value	Angle of Progression Change	γ
1	$d + ih$	$-p$	n/a	n/a
2	ih	$-1/k$	$\pi/2$	$1/2$
3	0	-1	$\pi/2$	$1/2$
4	a	1	$\pi/2$	$1/2$
5	$a + ih$	$1/k$	$\pi/2$	$1/2$
6	$(a - d) + ih$	p	n/a	n/a

Table 3: Important vertex quantities used in the Schwarz-Christoffel mapping of the MFC unit cell to the upper-half w -plane.

Figures 17 and 18 also illustrate the boundary mapping, equivalently the transformation of boundary conditions, between the two planes. Unlike the standard coplanar strip problem, the two transformed equipotential surfaces in the w -plane begin at $1/k$ and $-1/k$ and end at p and $-p$. Relative to the coplanar strip problem, this “shifting” of the equipotential boundary surfaces away from the origin of the w -plane invalidates the potential solution derived for the w -plane coplanar strip problem in equation (51).

To match the w -plane geometry of the transformed IDE unit cell to the standard coplanar strip geometry, a simple, invertible linear mapping function is used to contract the w -plane domain to the ζ -plane domain. Equation (52) is the mapping function that relates the w and ζ planes.

$$w = g(\zeta) = \frac{\zeta}{k} \quad (52)$$

Since complex linear functions are analytic on any complex domain [ref. 23], the transformation given by equation (52) is, by definition, a conformal map between the w and ζ planes. Conversely, the inverse of equation (52) generates the ζ -plane domain from the w -plane domain

$$\zeta = g^{-1}(w) = kw \quad (53)$$

Operating on the w -plane domain of the IDE unit cell with equation (53) transforms the w -plane to the standard coplanar strip problem, as exemplified by figure 19.

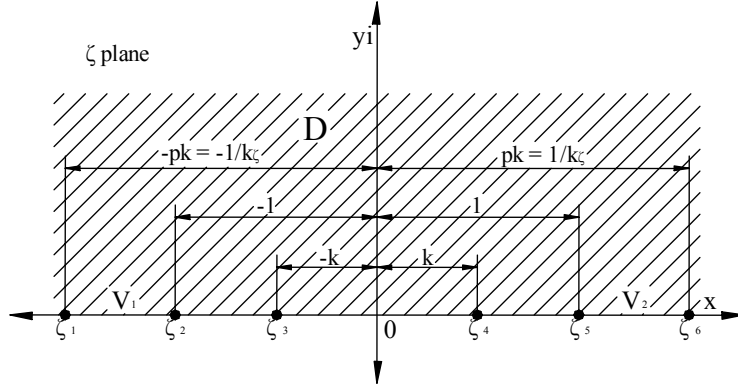


Figure 19: The mapping of the transformed MFC unit cell in the w -plane to the ζ -plane through the application of equation (53). Corresponding vertices are labeled, along with their distance from the imaginary axis.

By way of this secondary mapping, critical point #1 contracts from $-p$ to $-kp$ and critical point #6 contracts from p to kp . Vertices #2 and #4 reduce in value to -1 and 1 , respectively. Table 4 summarizes the relationships between the w -plane and ζ -plane vertices and critical points.

Vertex / Critical Point	W-plane Value	ζ -plane Value
1	$-p$	$-kp (-1/k\zeta)$
2	$-1/k$	-1
3	-1	$-k$
4	1	k
5	$1/k$	1
6	p	$kp (1/k\zeta)$

Table 4: Important vertex quantities used in the conformal mapping of the transformed MFC unit cell from the upper-half w -plane to the upper-half ζ -plane.

From knowledge of the mapping effects of equation (53) and inspection of figure 19, it is evident that the geometry of the equipotential strips of the w -plane changes in the ζ -plane to the geometry of the equipotential surfaces defined in the standard coplanar strip problem solved by equation (51). Introduction of an extra variable, the elliptic modulus k_ζ , completes the compatibility of the standard coplanar strip potential solution with the ζ -plane

$$\frac{1}{k_\zeta} = kp \Rightarrow k_\zeta = \frac{1}{kp} \quad (54)$$

Equation (54) relates the location in the ζ -plane of the critical points #1 and #6 to the inverse of an elliptic modulus, as called for by the standard potential solution for the coplanar strip problem. Calculated through this equation, the ζ -plane elliptic modulus is used as a constant value in the ζ -plane potential solution, and ultimately depends on the domain geometry of the z -plane.

Assembling these insights, the result for the standard coplanar strip problem solves the potential problem of the ζ -plane, and the w -plane potential solution smoothly arises through the synthesis of the mapping function between w and ζ and the standard coplanar strip potential formula via equation (51). Taking this mathematical step yields

$$\begin{aligned} P(\zeta) &= -\frac{(V_1 - V_2)}{2K(k_\zeta)} F(k_\zeta, \zeta) + \frac{(V_1 + V_2)}{2} \\ P(w) = P(g^{-1}(w)) &= -\frac{(V_1 - V_2)}{2K(k_\zeta)} F(k_\zeta, kw) + \frac{(V_1 + V_2)}{2} \end{aligned} \quad (55)$$

Repeating this mathematical operation one more time by substituting for w results in the

potential solution for the z -plane

$$\begin{aligned}
 P(w) &= -\frac{(V_1 - V_2)}{2K(k_\zeta)} F(k_\zeta, kw) + \frac{(V_1 + V_2)}{2} \\
 P(z) &= P(f^{-1}(z)) = -\frac{(V_1 - V_2)}{2K(k_\zeta)} F(k_\zeta, kf^{-1}(z)) + \frac{(V_1 + V_2)}{2}
 \end{aligned} \tag{56}$$

Since no closed form inverse function, $f^{-1}(z)$, exists for the complicated conformal map giving the relationship between z and w (eqn. (47)), the potential solution in the z -plane cannot be calculated through a closed form solution and must be obtained through numerical techniques.

Determining the z -plane electric field, and consequently the electric field produced by the dual-IDE structure, is an exercise of implementing the chain rule in conjunction with equation (34). Application of the chain rule is necessary because the derivation of the solution to the z -plane boundary value problem required two conformal mappings. Taking this fact into account, the expression for the electric field corresponding to the z -plane potential solution is

$$E(z) = -\overline{\left(\frac{dP}{d\zeta} \frac{d\zeta}{dw} \frac{dw}{dz} \right)} = -\overline{\left(\frac{dP}{dz} \right)} \tag{57}$$

Evidenced by the form of equation (57), information in the form of the potential solution for the ζ -plane, the mapping function from ζ to w and the mapping function from w to z coalesces mathematically to form the electric field solution for the z -plane. Manipulation

of equation (57) through substitution for the differential terms and ζ produces an exact equation for $E(z)$

$$\begin{aligned}
E(z) &= -\overline{\left(\frac{dP}{d\zeta} \frac{d\zeta}{dw} \frac{dw}{dz}\right)} \\
\frac{dP}{d\zeta} &= -\frac{(V_1 - V_2)}{2K(k_\zeta)} \frac{1}{\sqrt{(1 - \zeta^2)(1 - k_\zeta^2 \zeta^2)}} = -\frac{(V_1 - V_2)}{2K(k_\zeta)} \frac{1}{\sqrt{(1 - k^2 w^2)(1 - k_\zeta^2 k^2 w^2)}} \\
\frac{d\zeta}{dw} &= k \\
\frac{dw}{dz} &= \frac{2K(k)\sqrt{(1 - w^2)(1 - k^2 w^2)}}{a} \\
E(z) &= E(f^{-1}(z)) = -\frac{(V_1 - V_2)K(k)}{K(k_\zeta)a} \frac{\sqrt{1 - w^2}}{\sqrt{1 - k_\zeta^2 k^2 w^2}} = -\frac{(V_1 - V_2)K(k)}{K(k_\zeta)a} \frac{\sqrt{1 - (f^{-1}(z))^2}}{\sqrt{1 - k_\zeta^2 k^2 (f^{-1}(z))^2}}
\end{aligned} \tag{58}$$

Once again, as with equation (56), equation (58) isn't written explicitly in terms of z . Rather, the expression for the inverse mapping function between w and z (eqn. (18)) supplants z , as it is equivalent. Resulting from the lack of an explicit expression for the inverse mapping function of w in terms of z , this substitution signifies the need for an additional numerical step in the calculation of $E(z)$ at a specific point in the problem domain.

With these closed-form mathematical formulae for both the potential field and electric field of the MFC dual IDE system, the existence of an analytic solution to this complicated electrostatics problem is proven, contrary to past assumptions in the literature. Despite these achievements, actual application of the derived complex equations to predict the basic electronic properties and performance characteristics of a particular MFC design demands a great deal of numerical processing, alluded to earlier. Even if all of the equations describing the electrostatics of the MFC were explicit and invertible, the resources of computer technology would be crucial to complete the repetitive, difficult and probably voluminous potential and electric field calculations at multiple domain points. Understanding these facts, the next section addresses the

numerical issues inextricably intertwined with the use of the complex potential and field equations.

3.3 Computational Issues

Implementation of equations (56) and (58) obliges the solution of three transcendental equations (eqns. (45), (47), (54)) to yield values for the constants k and p and to determine image points in the w -plane for specific z values. As implied by the label “transcendental”, the algebraic or functional form of the equations where k , p and w are the only unknown quantities restricts the possibility of separating these variables from remaining terms, barring the derivation of explicit expressions. Because of this fundamental difficulty, this study employed software with numerical solver algorithms to numerically determine k , p and w as the zeros of three regrouped “zero” equations

$$\begin{aligned} \frac{a}{2h} - \frac{K(k)}{K(\sqrt{1-k^2})} &= 0 \Rightarrow k \\ \frac{a}{2K(k)} F(k, -p) + \frac{a}{2} - (d + hi) &= 0 \Rightarrow p \quad (59, 60, 61) \\ \frac{a}{2K(k)} F(k, w) + \frac{a}{2} - z &= 0 \Rightarrow w \end{aligned}$$

For each equation, the numerical solution for unknown variables was attained using the FindRoot function in the Mathematica ver. 4.2 software package. Under the options prescribed in this research, FindRoot exercised the secant method to carry out solution iterations, with a maximum of 1000 iterations allotted for any solution attempt. It should be noted that, even though numerical techniques were necessary to solve for constants appearing in the potential and electrostatic equations, the equations defining the constants and variables in this study are exact, and thus the numerical analyses should not be viewed as approximation methods. Instead, the solutions offered by the numerical methods in this study are exact numerical outcomes, limited in accuracy only by the decimal precision and mathematical integrity of the computational algorithms used in their determination.

Inevitably, the issue of computational accuracy arises in any work that is dependant on numerical analysis and sensitive to the degree of numerical precision employed in that analysis. Most conventional mathematics software packages, including Mathematica 4.2, perform calculations to 16 decimal places of precision. Complete and incomplete elliptic functions are particularly sensitive to minute variations in parameters like the elliptic modulus, producing drastically different results for identical arguments if the elliptic modulus changes by a miniscule amount. Manifested in the extreme efforts made to calculate high precision k values, great care was taken to ensure reliable results in calculations involving elliptic functions, at least within the limits of Mathematica and MATLAB. To avoid delving into the massive topic of the computer science of numerical analysis, which is outside of the scope of this study, no customized programs were written to attain the high precision k values needed. Instead, any numerical analysis conducted in this study implemented only the built-in numerical solver algorithms and elliptic function generators of Mathematica and MATLAB, which were all limited by 16-digit precision and the transparent numerical methods used to program them.

Mostly, the elliptic moduli values produced by the numerical solver algorithms for different MFC designs were sufficiently precise to guarantee software-internal accuracy. By this, it is meant that the internal check of using Mathematica or MATLAB to evaluate the zero equations with the numerically solved k values resubstituted resulted in very small values, on the order of 10^{-6} . In these internally accurate cases, maps between the w -plane and z -plane implementing the numerically generated k -values proved valid, with w points always mapping to z points within the limits of the selected z -plane domain geometry. For several problem geometries, however, the Mathematica solver, under the specified iteration limit and solver method constraints, didn't converge to or generate k -values accurate enough to calculate accurate maps. Situations where this occurred forced the use of a specialized MATLAB program, exclusively written for this investigation. Designed to manually iterate through k -values using a binary search method and MATLAB's onboard elliptic function, the k optimizer program refines guesses for the zeros of equation (59) until reaching a k -value which results in an

equation result less than 10^{-6} . With this combined approach of using Mathematica's solver function and the tailored MATLAB program, a set of software internally accurate k -values were determined for a continuum of IDE geometries.

Similar issues influenced the calculation of the p -values for each IDE geometry, which, in reality, are equivalent to the w -plane characteristic k -values, since the ζ -plane characteristic parameter k_ζ depends only on k and p . Indeed, the built-in Mathematica solver failed to optimize p value solutions to equation (47) resulting in 10^{-6} accuracy for the majority of IDE design cases, and the custom MATLAB solver program was extensively employed to determine p values. Given accurate p and k values for many different MFC designs, the calculation of w images for specified z points presents other challenges.

Noted earlier, the mapping function relating the w -plane to the z -plane is inherently non-invertible, and consequently demands a numerical solver algorithm to ascertain the values of w -plane points for specified z -plane points. Since this study seeks to determine the electrical field and potential solutions of the z -plane, which models the physical MFC problem, for a defined set of z values, it is necessary to enact a numerical solver algorithm to calculate every w point. Following the regimen laid out in the calculation of p and k values, internal software checks in Mathematica of the correspondence between every pair of z and w points were performed by substituting the numerically derived w values back into equation (47) and evaluating the result, producing recalculated z values. If high precision, accurate k and p values are used as constants in equation (47), the recalculated z values matched the originally specified z values to a precision of 10^{-6} or greater. This finding led to the conclusion that the Mathematica solver function, FindRoot, limited calculation errors to a level enabling accurate conformal mapping between the z -plane and w -plane.

Although the need for a numerical solver presents no theoretical problem in the context of the already numerical environment of computer software, which also introduces error when evaluating invertible, explicit equations, it does broach the subject

of a conformal mapping phenomenon called crowding. A type of ill-conditioning, crowding refers to dense regions of mapped points that correspond in their image plane to points occupying relatively large domains. Thus, exponentially small changes in the coordinates of the pre-image plane produce very large changes in the coordinates of the image plane. Conversely, crowding hinders attempts to numerically calculate points in the pre-image plane from known points in the image plane. Often, the difference in pre-image point values for significantly varying image points is smaller than calculable using standard IEEE 16 bit precision. Usually, crowding takes place when mapping to extremely elongated regions, such as rectangular domains with large aspect ratios [ref. 11]. On several occasions in the course of this study the mapping of the upper-half plane to elongated rectangular domains gave rise to crowding, especially in the domain regions adjacent to electrodes. Crowding induced some minute errors in the calculation of the electrical field along domain boundary segments corresponding to electrodes. However, these errors did not significantly affect the total capacitance calculations for each MFC design, which depend on the electric field along the MFC electrodes. Fortunately, the level of precision employed by the Mathematica software overcame any crowding-based difficulties for the standard locus of z -plane points used in the calculation of potential and electric fields within the problem domain, successfully arriving at internally accurate w -plane pre-image values for every z value.

Chapter 4

Model Results

4.1 Commercial MFC Electrical Properties Solution

Heeding the issues associated with the computational implementation of all of the conformal mapping theory developed and exercised thus far, MATLAB and Mathematica programs were written to produce many actual results for the electrical and actuation properties of the commercially available MFC and numerous design variants. Initial goals focused on the analysis of the commercially available MFC through the numerical implementation of the conformal mapping solutions developed in Chapter 3. Two programs, one in Mathematica and one in MATLAB, were written to perform the necessary computations to develop the electrical field and potential field solutions and then to post-process the results. Subdividing the computational tasks in terms of the best software to perform particular operations, the Mathematica code calculated the potential and electrical field solutions for the problem while the MATLAB code performed post-processing and imaging duties. Refinement of k and p values for the geometry of the commercial MFC wasn't necessary, as the aspect ratio of this particular problem is small enough to avoid problems associated with crowding.

Characteristic parameters for the unit cell of the commercial MFC were acquired from the Smart Materials Corp. website [ref. 39], which posts figures for the dimensions of the commercial MFC fibers, electrodes and structural spacing. Extracting pertinent data from the Smart Material Corp. website [ref. 39], the electrode-to-electrode centerline spacing dimension was equated with a , half the fiber height dimension was equated with h and half the electrode width dimension was identified with d . Table 5 summarizes the structural dimensions of the commercial MFC.

Commercial MFC Unit Cell Dimensions	
a	$50 \times 10^{-5} \text{ m}$
h	$8 \times 10^{-5} \text{ m}$
d	$5 \times 10^{-5} \text{ m}$

Table 5: Unit cell dimensions of the commercial MFC as dictated by the design of the commercial MFC dual-IDE structure [ref. 39].

Using the custom Mathematica program, characteristic parameters for the commercial MFC were substituted into equations (59) and (60), which were numerically solved for k and p , respectively, with Mathematica's FindRoot function. Table 6 records the critical calculated values of the commercial MFC problem, establishing the vertex geometry of the w -plane.

Commercial MFC Unit Cell Characteristic Solution Values	
p	1.00101051
k	0.99956417
$1/k$	1.00043602

Table 6: Numerically calculated values defining the conformal mapping of the commercial MFC unit cell between the z -plane, w -plane and ζ -plane.

After this step, the program initialized a 15×15 matrix of z -plane points, discretizing the unit cell domain into a lattice of spatial locations. Points were spaced at uniform intervals along the width and height of the unit cell, positioning them at the centers of 225 discrete and equally sized rectangular sub-regions. For each point in the lattice, the program calculated a unique potential field and electrical field value. Figure 20, produced by the MATLAB program in the post-processing phase, illustrates the z -plane domain for the commercial MFC, including the solution points of the analysis. Interpreted physically, this plot represents a 2-D section of the unit cell, limited on each side by the physical symmetry of the dual IDE structure.

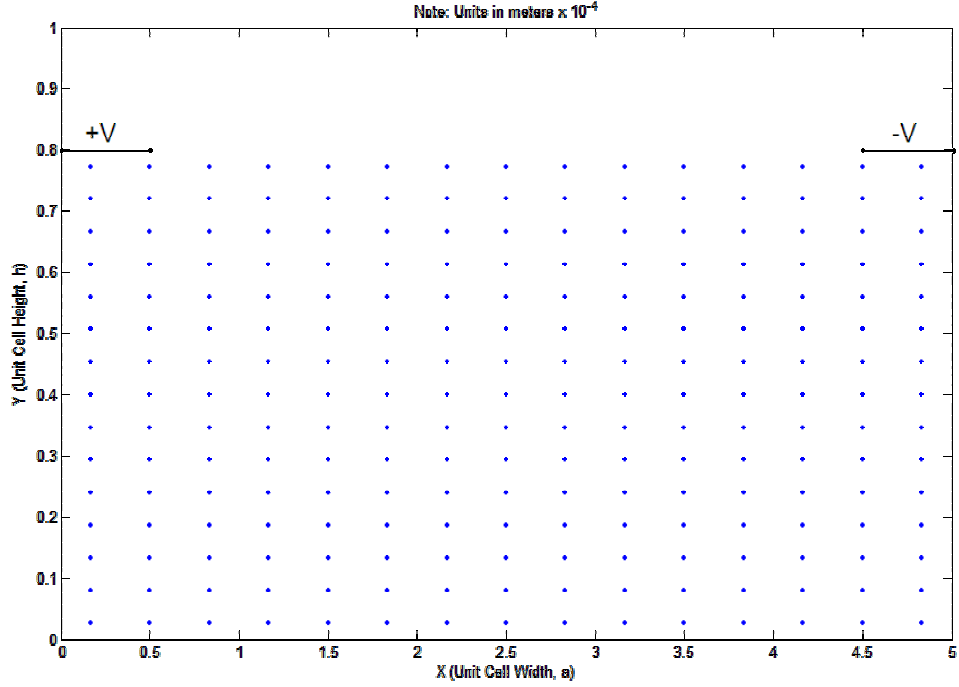


Figure 20: Solution grid for the commercial MFC unit cell in the z -plane. The proper geometric locations for the MFC electrodes are indicated in the figure, while the edges of the unit cell correspond to the plot limits.

Having determined k , p and the z -plane points to calculate field solutions for, the Mathematica code numerically solved the zero-form of equation (47), equation (61), for the w -plane points corresponding to the z -plane points in the z -plane lattice. Solving equation (61) for every z produced a matching 15×15 matrix of w values, pre-images of the z -plane values, located in the upper-half plane domain of the w -plane. Figure 21 shows the location of the w points in the w -plane. Especially clear in this depiction, the moderate influence of crowding groups most of the w points near the mapped electrodes on the real axis, which are very small due to the small distance between p and $1/k$.

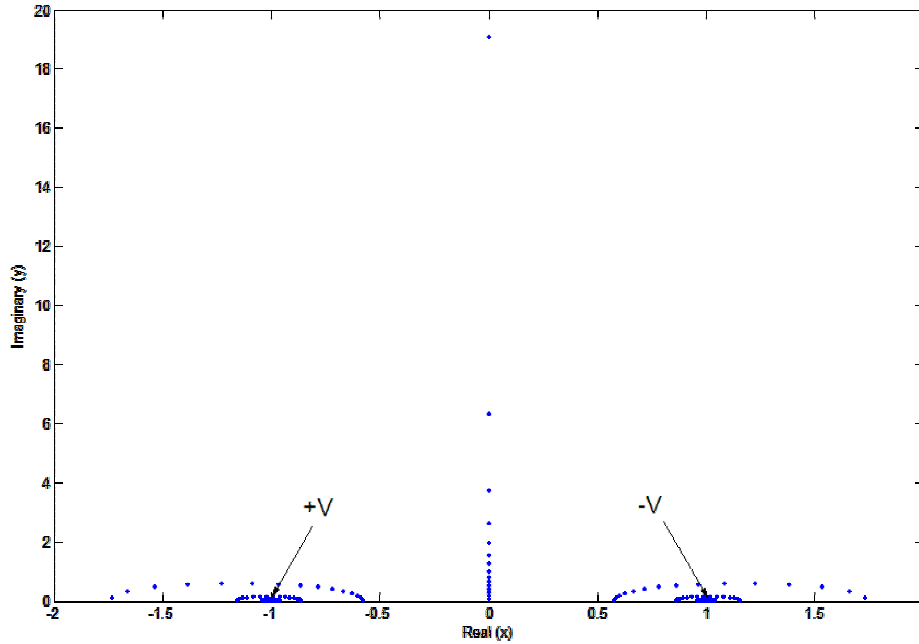


Figure 21: The solution grid for the commercial MFC mapped to the w -plane. The mapped electrode boundaries are indicated in the figure.

Substitution of the numerically derived values defining the w -plane solution locus into equations (58) and (56) readily yielded solutions for the electrical and potential fields of the commercial MFC geometry in the z -plane, as well as the electrical and potential fields in the w -plane. Sequentially solving equations (56) and (58), the Mathematica program finally arrived at the potential field and electrical field solutions of the commercial MFC problem at the specified lattice locations in the z -plane. Solutions for the w -plane potential and electrical fields were also calculated at the preimage points in the w -plane. The solution steps in the Mathematica code assumed a net potential difference of 1 V between the positive and negative electrodes of the MFC, with the “positive” electrode having a constant potential of 1 V and the “negative” electrode at a voltage of 0 V, or ground. As a consequence of the mathematical form of the electrical field solutions, the difference in voltages between the electrodes affects the form of the output solution, instead of the actual voltages at the electrodes. Thus, the z -plane and w -plane electrical field solution is the same for electrode voltages of 0.5 V and -0.5 V as it is for voltages of 1 V and 0 V. Potential field solutions for both the w -plane and z -plane

are affected by the choice of high and low voltage boundary conditions as well as the potential difference between the boundaries, but only by a constant which shifts the potential value of every data point by a constant value. Data sets for all four solutions were exported to text files for record purposes, and then examined by the MATLAB post-processing code, which produced plots describing the solutions and performed various analysis operations on the data sets.

Figure 22 is a contour plot of the w -plane potential field extrapolated from the defined set of solution points. Inspection of this plot reveals the high density of the contour lines immediately surrounding the mapped electrodes, indicating drastic potential gradients and large electric fields. Between the electrodes, the potential field changes more gradually, indicating smaller electric field magnitudes.

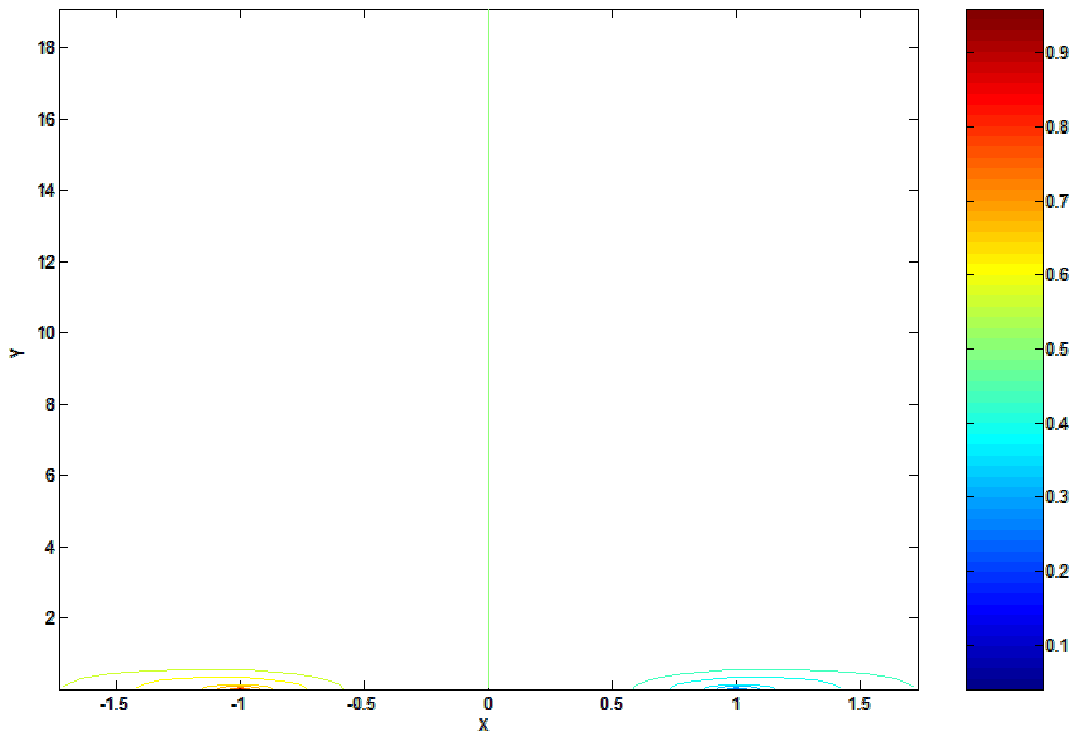


Figure 22: Contour plot of the transformed potential field of the commercial MFC in the w -plane.

Graphically depicting the potential solution for the commercial MFC unit cell, figure 23 is a contour plot of the z -plane potential solution, also extrapolated from the individually calculated potential solutions at lattice points. Consideration of figure 23 exposes the highly regular x -direction spacing of the potential field contour lines of the commercial MFC, implying a consistent magnitude electrical field in the x -direction over the piezoceramic fiber region between electrodes.

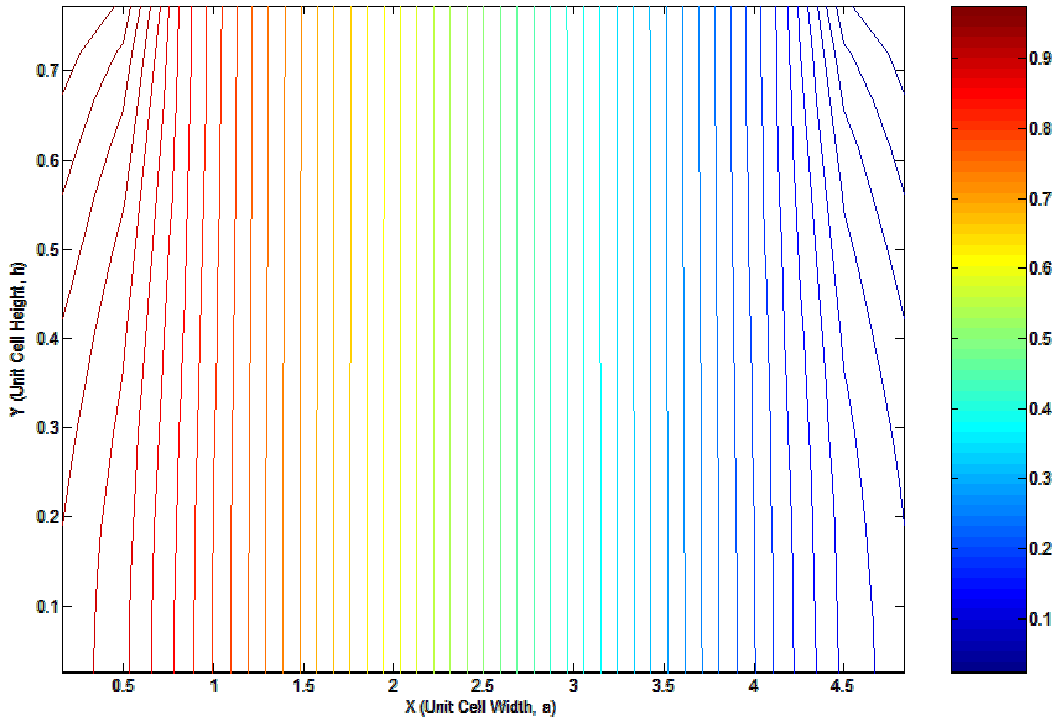


Figure 23: Contour plot of the potential field of the commercial MFC unit cell, plotted in the z -plane.

Superceding the previous results in terms of both importance and utility, the electrical field solution for the z -plane, as calculated through the conformal mapping equations by Mathematica, is expressed by figure 24. As expected, the behavior of the electrical field along the edges of the unit cell corresponds to the boundary conditions postulated in the problem formulation. Also, the electrical field vectors near the boundaries of the domain point in a direction very similar to the sense of the boundary vectors, extending the behavior of the electric field at the boundaries deeper into the z -

plane domain. Predicted by the contour plot of the z -plane potential solution, the electrical field solution for the commercial MFC unit cell is highly regular in the region of the piezoceramic fiber between the electrodes. Field vectors in this “active” region exhibit an aligned x -direction sense, as well as uniform magnitude. High field magnitudes occur immediately adjacent to the electrodes, with a maximum field concentration at the electrode tips. Many references document this well known effect in dual-IDE piezocomposite actuators, which often leads to stress induced cracking in the piezoceramic fibers near IDE edges.

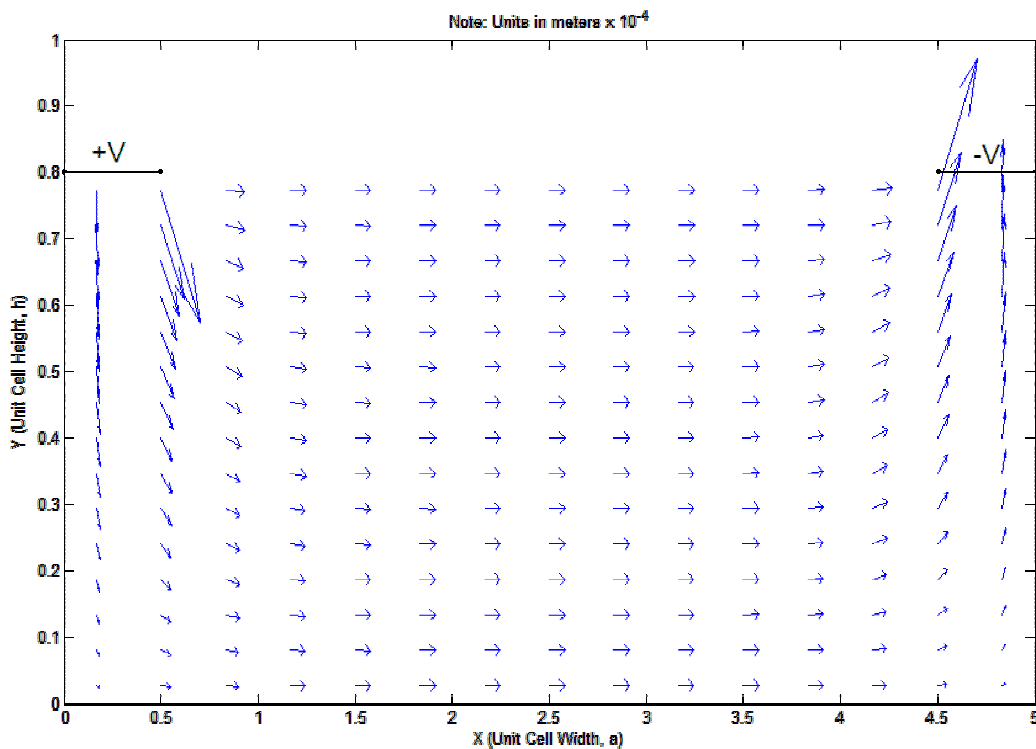


Figure 24: The electrical field of the commercial MFC unit cell, plotted in the z -plane. The correct geometric locations of the unit cell’s electrodes are indicated, while the edges of the figure correspond to the actual edges of the unit cell. Vector sizes are scaled to the correct relative vector magnitudes.

Comparison of the conformal mapping results for the commercial MFC electric field to a typical FEA solution for the identical problem evinces important differences between the two models. FEMLAB, a commercially available MATLAB module for finite element analysis, was used to develop an equivalent finite element solution for the

commercial MFC unit cell. After specifying the boundary conditions for the finite element problem to be the same as for the conformal mapping problem, FEMLAB meshed the problem domain with a free meshing algorithm using nonlinear finite elements. FEMLAB calculated a solution to the potential problem for the unit cell from the finite element formulation, and an electric field solution option in the solution step enabled output of electric field values at the same coordinates as for the conformal mapping solution. Figure 25 shows the electrical field solution as determined by the finite element method of FEMLAB. For this particular solution, FEMLAB was used to create a relatively fine finite element mesh composed of 1,165 nodes and 2,176 elements.

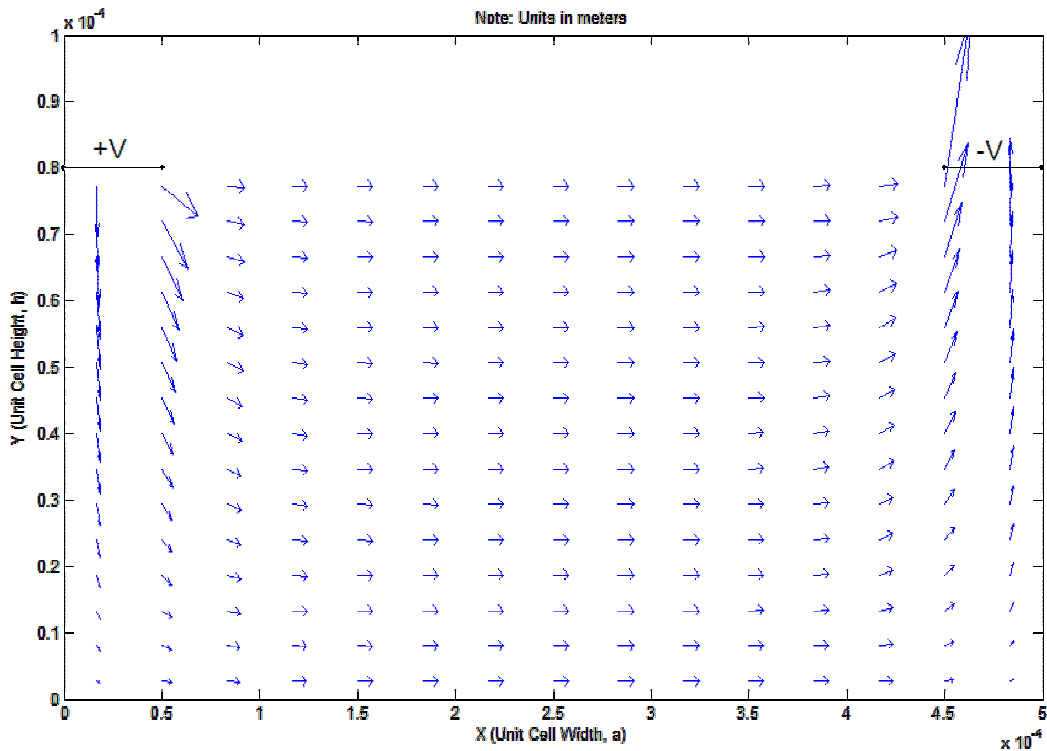


Figure 25: The electrical field of the commercial MFC unit cell as calculated using FEMLAB. Again, the correct geometric locations of the unit cell electrodes are indicated, and the edges of the plot correspond to the edges of the unit cell. Vector sizes are scaled to the relative vector magnitudes.

Visual comparison of figures 24 and 25 suggests subtle differences between the two solutions, such as more extreme electric fields in the vicinity of the electrodes for the

conformal mapping solution. A true juxtaposition, however, demands a quantitative mathematical approach, comparing the magnitudes and directions of the vector fields in both solutions. Running the customized MATLAB code accomplished this task in the post-processing step. Assuming a close match between the magnitudes of the vector fields, the direction of the fields was compared first. At each solution point for both the FE and conformal mapping solutions, the MATLAB code determined the angle of the electrical field vector measured from the x -axis and saved the solutions for both methods at points where the angle difference between the different solutions is greater than 1° . Figure 26 gives the plot of the angularly disagreeing vectors, vectors differing in phase by more than a degree, for the FE solution. Clearly, the solutions don't match, at least for the direction of the vector field, near the electrodes and in the inactive regions of the piezoceramic fibers.

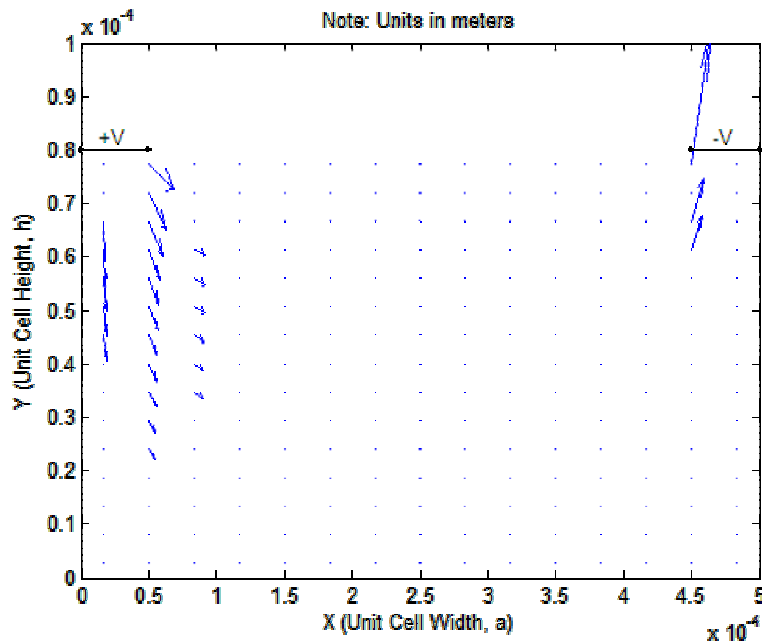


Figure 26: High error electric field vectors between the conformal mapping and fine-mesh FEA solutions. The vectors plotted in this unit cell are the conformal mapping solution vectors.

Isolation of the error, whether in the finite element solution or the conformal mapping solution, is a simple exercise of generating a coarser FE mesh and recalculating

the FE solution. If the disagreement between an FE solution based on a less refined mesh and the conformal mapping solution increases, it proves that the finite element solution converges to the conformal mapping solution with increasing numerical precision in the FE model. A pattern of this nature would also demonstrate the greater accuracy of the conformal mapping solution, which, as an exact numerical solution based on analytical expressions, is expected to be the most correct solution. To this end, the finite element solution was recalculated for a coarse mesh of 88 nodes and 136 elements and compared again to the conformal mapping solution using the MATLAB post-processing code. Figure 27 presents the results of the same angular comparison used in figure 26, plotting the FE solution vectors only at the analysis points where the FE and conformal mapping vector phases differed by more than 1° . Not only does this image show that the FE solution using the coarser mesh differs from the conformal solution at more points than for the finer mesh, but it also exemplifies the growing degree of error between the angles of the field vectors in either solution.

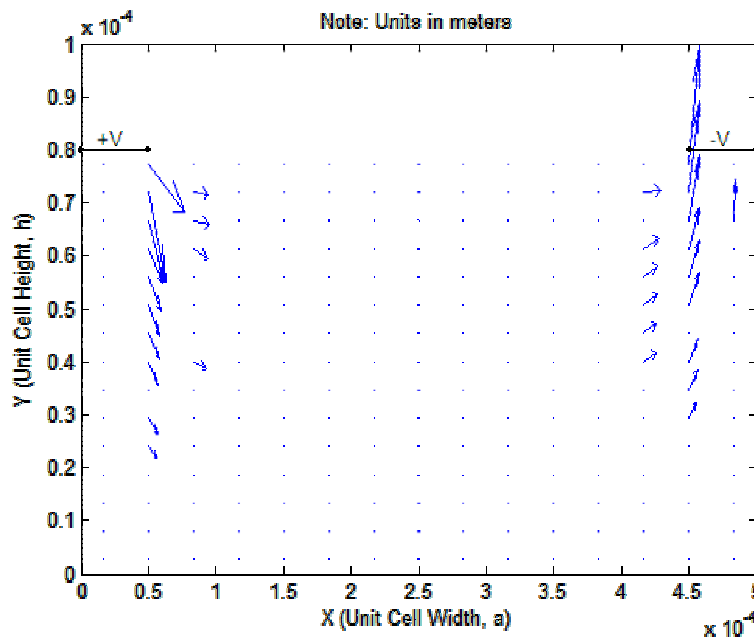


Figure 27: High error electric field vectors between the conformal mapping and coarse-mesh FEA solutions. The vectors plotted in this unit cell are the conformal mapping solution vectors.

Demonstration of the exactitude of the conformal mapping solution, while promising in terms of more accurate evaluations of MFC behavior, doesn't project any useful engineering information. Prediction of the capacitance properties of the MFC is one worthwhile application of the conformal mapping solution. Individual electrodes in the MFC function as "capacitor plates", separated by a finite gap and differing by a known differential voltage. Each MFC unit cell may be defined as a small capacitor, possessing a high voltage electrode from which all of the electric field lines in the domain emanate and a low voltage electrode at which all the electric field lines terminate. In each repeating cell, the outside edges of the capacitor region are delimited by horizontal or vertical electrical field lines and the physical boundary of the MFC where the IDEs lie, the same domain as the z -plane. The capacitance of a bounded electrostatics system, generically illustrated in figure 28, with a known electric field and potential boundary conditions is calculated using

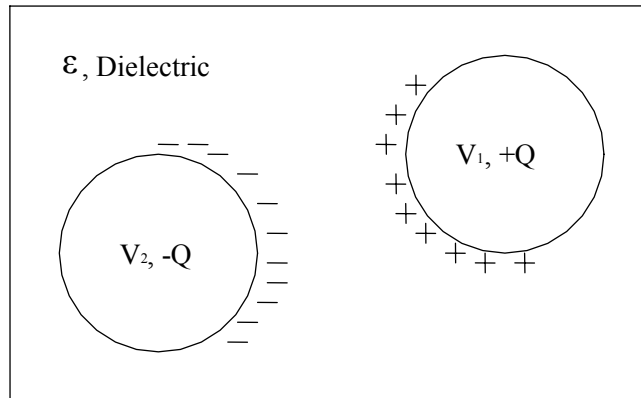


Figure 28: Generic system of charged bodies forming a simple capacitor; $V_0 = V_1 - V_2$.

$$C = \frac{Q}{V_0} = \frac{\epsilon \oint_S \underline{E} \cdot d\underline{S}}{V_0} \quad (62)$$

where Q is the total charge stored on one of the equipotential boundaries, V_0 is the potential difference between the defined equipotential boundaries of the system, ϵ is the permittivity of the dielectric constant pervading the electrostatics system and $d\underline{S}$ is a

differential surface element of an equipotential surface. Thus, solving the surface integral of the electric field at one of the MFC electrodes and dividing by the potential difference between the electrodes yields the capacitance of an individual MFC unit cell.

Logically, the same Mathematica code used to calculate the electrical field of the commercial MFC within the unit cell domain can also evaluate the values of the electric field of the MFC along the IDEs. Slightly modifying the Mathematica code from the version used to calculate electrical field values in the problem domain, 100 equally spaced points along the entirety of the high-potential IDE were initialized and electrical field values were determined at each point. Post-processing of the resulting data using the MATLAB program produced figure 29, a plot of the conformal mapping solution for the local IDE electrical field of the commercial MFC.

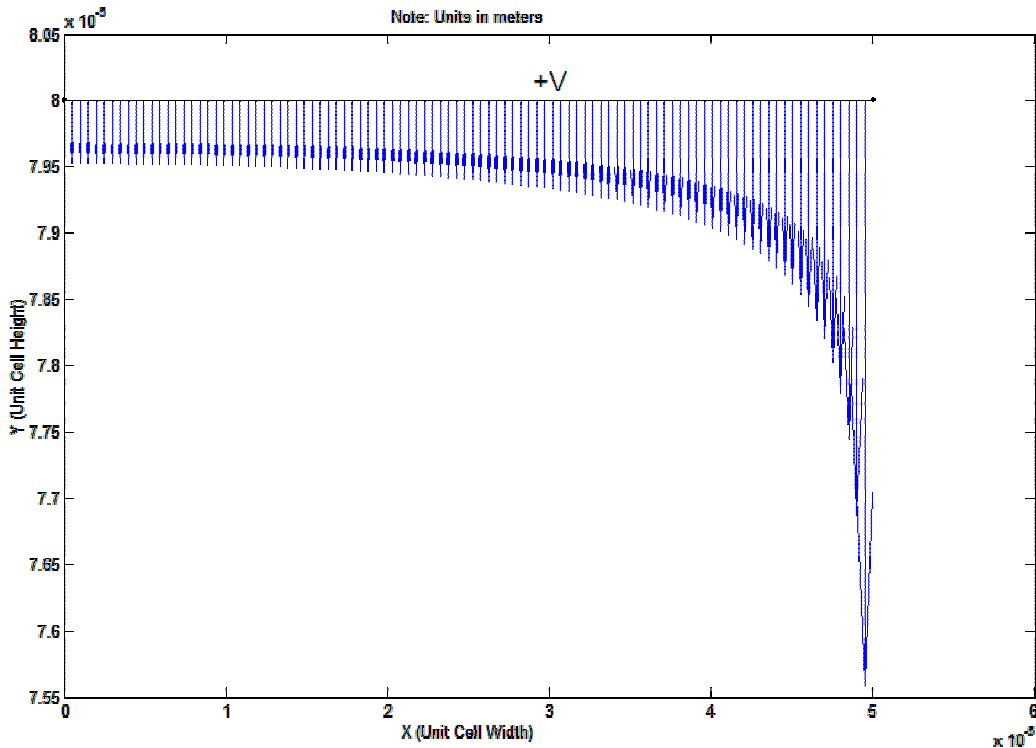


Figure 29: Electrical field at the high-voltage electrode of the commercial MFC unit cell. This plot results from calculations based on the conformal mapping solution.

Consistent with the boundary conditions prescribed for the MFC unit cell, all of the electrical field vectors along the high-voltage IDE point in the negative y -direction, having pure imaginary values. Figure 29 clearly illustrates the smoothly increasing magnitude of the electrical field to a maximum at the tip of the IDE.

Identical to the methods employed in the analysis of the electrical field within the unit cell domain, FEMLAB calculations provided an equivalent finite element solution of the electrical field along the MFC IDE. Finite element codes directly estimate domain solutions to physical problems but not boundary solutions, which must be explicitly specified in order to conduct an FE analysis. Consequently, FEMLAB can only interpolate the boundary electrical field of the MFC unit cell based on the domain solution. Computing the electrical field vectors at the same 100 points along the IDE used in the conformal mapping solution, FEMLAB generated the local IDE field solution plotted in figure 30.

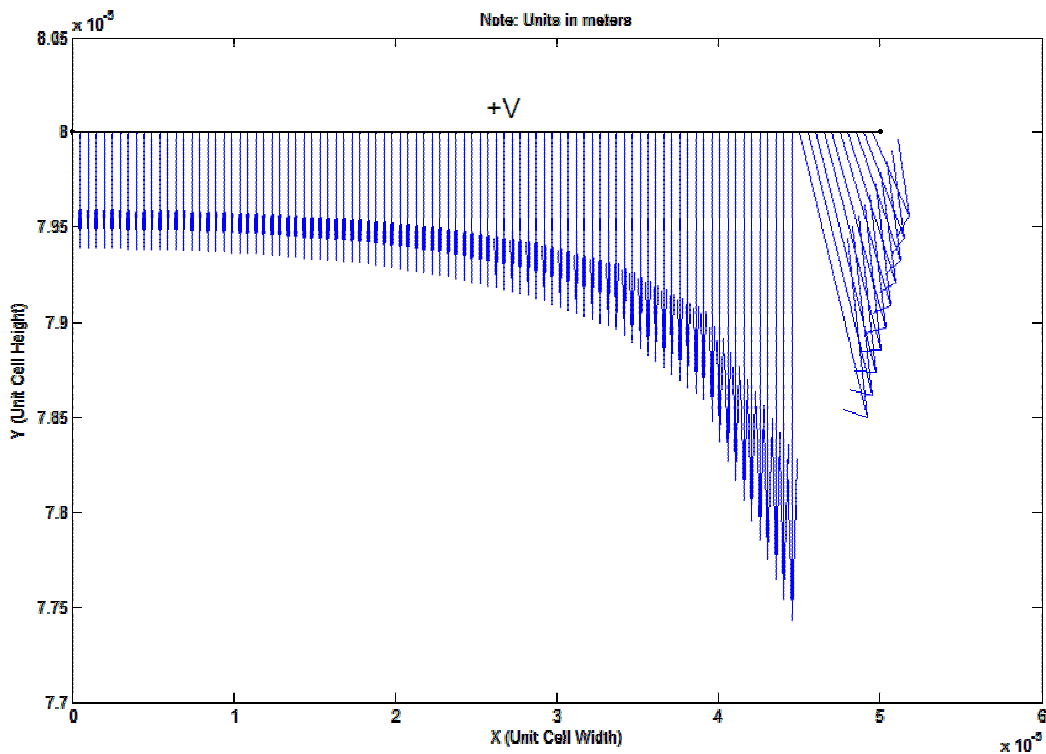


Figure 30: Electrical field at the high-voltage electrode of the commercial MFC unit cell. This plot results from calculations based on the FEA solution.

Immediately, significant dissimilarities between figures 29 and 30 materialize. Most importantly, the FE solution computes electrical field vectors that violate the physically mandated boundary conditions of the MFC unit cell. By electromagnetic theory, the electrical field lines emanating from an equipotential surface should be perpendicular to the surface. Near the IDE tip, the FE solution field vectors possess a significant x -direction component, breaking this intuitive electrostatic law. Furthermore, the field vectors in the vicinity of the IDE tip exhibit a markedly lower magnitude than vectors farther away from the tip, conflicting with physically supported expectations. Finally, the smooth progression of increasing electrical field magnitude near the IDE tip characterizing the conformal mapping solution is absent in the FE solution, which follows a piecewise progression.

Direct calculation of the capacitance of the commercial MFC unit cell using equation (62) was not possible. Because the electrical field solutions are necessarily discrete, exact integration of the continuous surface integral contained in equation (62) was not possible. Instead, a numerical integration technique of summing the field fluxes estimated for individual electrical field vectors was employed to approximate the solution for the capacitance of the unit cell. With this method, a summation of the dot products of each field vector with the differential electrode area corresponding to it along the length of the MFC electrode yields the value for the total charge on the electrode surface. Since the orientation of the MFC electrodes is parallel to the real axis in the conformal mapping expression of the MFC unit cell, the area dot product of an electric field vector at the electrode is simply the product of the discrete area of the electrode and the imaginary component of the vector running through the area element.

Equation (63) summarizes the discrete surface integration technique mathematically

$$Q = \varepsilon \oint_S \underline{E} \cdot d\underline{S} = \varepsilon \sum_{n=1}^{100} E_y A_n = \varepsilon \sum_{n=1}^{100} \text{Im}(E) A_n \quad (63)$$

$$A_n = \left(\frac{d}{100} \right) \cdot t$$

where A_n is a discrete portion of the overall electrode area and t is the depth of the MFC unit cell. Clearly, the result of equation (63) also depends on the permittivity of the dielectric material intervening between the electrode surfaces. A comparison between capacitance results derived from FEA and the conformal mapping solution don't depend on the dielectric constant, however, as it only linearly scales the capacitance of the unit cell. Postulating a dielectric permittivity of 1.682×10^{-8} over the domain of the unit cell, this study prescribed a permittivity constant consistent with the properties of PZT 5-AH, effectively assuming that this material fills the space between the MFC electrodes. Only an idealization, this assumption doesn't impact the comparative results between the FEA and conformal mapping solutions, but it does simplify the numerical processing of the electrical field data. Also, the application of equation (63) demands the specification of a commercial MFC unit cell depth, since the FEA and conformal mapping solutions only analyze 2-D regions. Again, as with the case of the dielectric permittivity constant, the unit cell depth only scales the capacitance result and cancels out of any comparative ratio, so a depth value of $t = 1$ was chosen to simplify data processing.

Employing equation (63) to numerically calculate the MFC unit cell capacitance founded on the FEA and conformal mapping electrical field data, the MATLAB post-processing code resolved two disparate capacitance values for each solution method. Table 7 presents the capacitance values of the commercial MFC unit cell established from both the FEA and conformal mapping data.

Commercial MFC Unit Cell Capacitance	
Conformal Mapping Capacitance	2.551×10^{-9}
FEA Capacitance	2.606×10^{-9}
% Difference	2.11%
ε	1.682×10^{-8}
t	1

Table 7: Numerical results for the capacitance of the commercial MFC unit cell and selected constants.

Evinced by table 7, the conformal mapping solution prognosticates a slightly lower value for the capacitance of the commercial MFC unit cell than the FEA solution. Although a 2.11% difference isn't significant, other MFC structural geometries, modified from the commercial MFC design, exacerbate the dissimilarities between the capacitance values generated by either model. Irrespective of the quantitative differences between the capacitance values, the data used for calculation of the FEA based capacitance value contains inherent flaws stemming from its disagreement with physical knowledge. As such, no physically accurate data supports the FEA solution for the commercial MFC unit cell capacitance, which probably corresponds to the conformal mapping solution by chance.

Proof of the descriptive capacity and accuracy of the conformal mapping solution in quantifying the electrostatic phenomenon of the commercial MFC design opens new avenues for the exploitation of the conformal mapping model. Foremost, despite the prominent numerical issues linked to the computational implementation of the conformal mapping technique, the speed, efficiency and accuracy of the method encourage its adaptation to optimization studies of a continuum of MFC designs. Indeed, the time elapsed during the computational execution of the conformal mapping solution is far less than for an equivalent FEA analysis, with a truer data set output. Repeating the processes used to analyze the capacitance of the commercial MFC, the direct resolution of the capacitances of a matrix of MFC geometries culminates in a set of three-dimensional capacitance plots that encapsulate the effects of MFC design on unit cell capacitance.

4.2 Variation of MFC Capacitance with Respect to IDE Design

As with the commercial MFC study, discrete numerical techniques served as the means to explore the relationship between MFC capacitance and MFC design. Using the “brute force” tactic of iteratively computing the capacitance of a large group of representative MFC designs with the same code used in the commercial MFC analysis, a compilation of capacitance information was assembled. Choosing a grid of discrete MFC design geometries framed a systematic approach to establishing the affect of MFC IDE geometry on MFC unit cell capacitance. Two characteristic geometric variables dictate the full range of possible MFC dual-IDE designs. These two parameters, electrode width and center to center electrode spacing, respectively correspond to the defined unit cell quantities of electrode half-width, d , and unit cell width, a . Fixing the unit cell height, h , which is half the height of a piezoceramic fiber, the parameters a and d were each adjusted over specified sets of values. All unique permutations of the values of a and d delineated a set of MFC designs, each with MFC unit cell equivalents. Despite fixing h , this method of specifying unit cell geometries accounts for all possible variations of the dual IDE design, since a simple scaling of the resulting designs produces the full spectrum of possible unit cells with differing piezoelectric thicknesses. An appropriate insight is that the capacitance data is normalized with respect to unit cell height, which doesn't reduce the generality of the information. For every unit cell geometry, a modified Mathematica code calculated unit cell capacitance following the same process as for the commercial MFC.

Visualizing the physical meaning of the combinations of a and d values offers the correct interpretation of the unit cell designs defined by these quantities. Large a values combined with relatively small d values correspond to a widely pitched, narrow IDE design. Conversely, a large d dimension and a small a dimension designates narrowly spaced, wide electrodes. Indubitably, the size of a limits the maximum size of d , which may not be larger than $\frac{1}{2}a$ for a fully electroded MFC surface. Additionally, the absolute size of a and d influence the capacitance value of a unit cell to the same degree as the

ratio of d to a , since a large d to a ratio can indicate either small electrodes with proximate center to center spacing or large electrodes with distant center to center spacing.

Plots of the capacitance of different unit cell geometries reflect the restraints on the dimension of electrode width due to the center to center electrode spacing. During the selection and pairing of the a and d values, the numeric range of possible d values was limited to a minimum of 3.1×10^{-5} meters and a maximum value of 95% of $\frac{1}{2}a$. Inhibiting accurate electrical and potential field solutions, moderate crowding problems occurred when the electrode half-widths were narrower than the minimum value of 3.1×10^{-5} meters, irrespective of the value of a . Similarly, when specifying d larger than $0.475 \times a$, moderate crowding phenomenon appeared, ruining any confidence in the accuracy of the associated conformal mapping solutions.

Within the confines placed on the unit cell dimensions by crowding difficulties and geometric considerations, a 10×10 matrix of d and a pairings was selected. Specifying h as a constant 5×10^{-4} meters, the Mathematica program also initialized ten discrete a values transcending a scope of 4×10^{-4} meters to 40×10^{-4} meters, with each at equal intervals over the range. Every a value matched ten coordinated d values, also equally delimited, spanning quantities from 0.31 to $0.475 \times a$. Pairing a and d values in this manner produced the 10×10 matrix of MFC design test points. Calculating the capacitance of the MFC unit cell for each of these selected designs and plotting it on the z -axis in a 3-D space, with a and d as independent variables on the x and y axes, yielded figures 31 and 32.

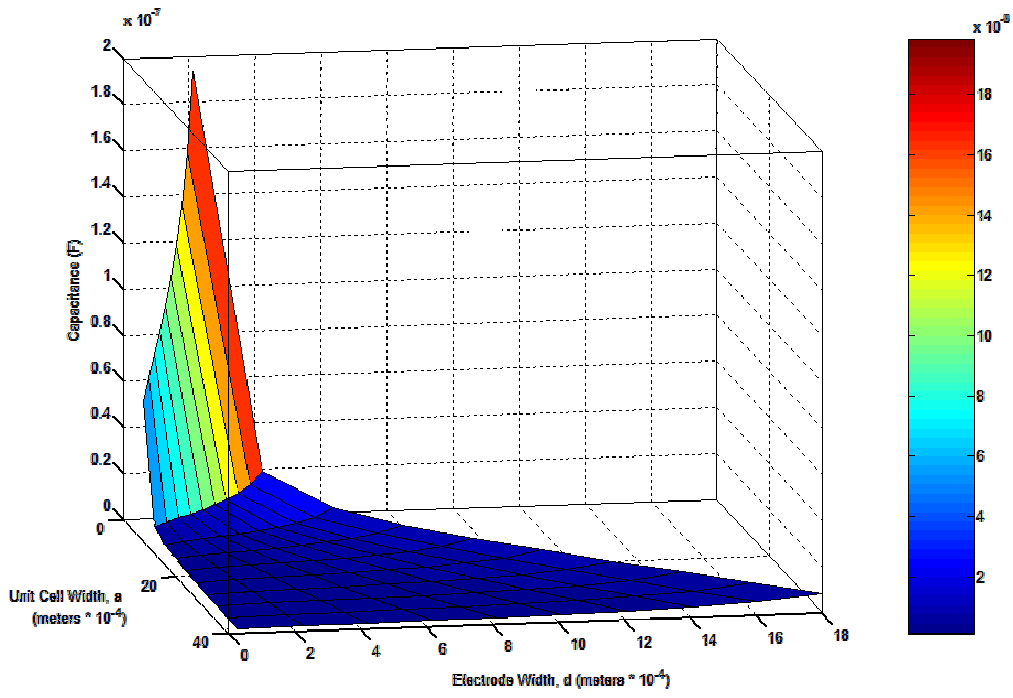


Figure 31: Capacitance of the MFC unit cell as it varies with electrode spacing and electrode width, perspective angle (1).

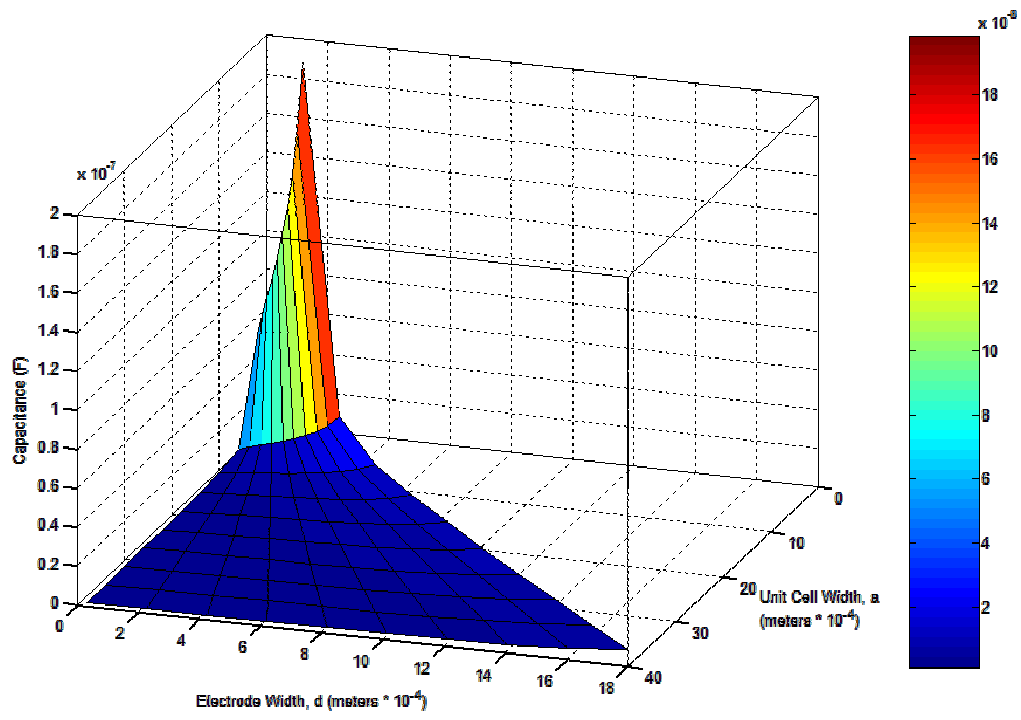


Figure 32: Capacitance of the MFC unit cell as it varies with electrode spacing and electrode width, perspective angle (2).

Understanding that surface elements in the capacitance plot don't represent actual data, but merely linear connections between actual calculated data points, inspection of figures 31 and 32 immediately reveals important features. Rotated versions of the same plot, both images demonstrate the unimodal behavior of the capacitance of the MFC unit cell with respect to unit cell geometry. Absolute minimum and maximum points in the capacitance plot coincide with the only local minimum and maximum points for the tested domain. Even though the surfaces in these plots are only linear interpolations between data points, they suggest the global nature of the variance of capacitance with unit cell geometry. Viewing the plot surface, the capacitance characteristics for different unit cell designs smoothly progresses between test points, without sudden dips, increases or discontinuities. The smoothness of the capacitance plot indicates that the capacitance of more extreme geometries for MFC unit cells continues to follow the trends exhibited over the studied domain, with larger electrodes and smaller center to center spacing resulting in higher capacitance.

Due to the pronounced peak in capacitance occurring over the sub-region of the capacitance plot demarcated by small a values, a second, localized domain was analyzed to examine the capacitance characteristics of narrow unit cells in detail. Calculating the capacitances for a focused 10×10 matrix of unit cell geometry points, the Mathematica code generated data for unit cells ranging in width from 4×10^{-4} meters to 10×10^{-4} meters, maintaining the restrictions on electrode width used for the first analysis. Figures 33 and 34 are equivalent plots of the outcome of this analysis, with a rotation introduced between the plots for illustrative purposes. Shown in the plots, the capacitance of the MFC unit cells increases smoothly and exponentially with diminishing center to center electrode spacing, relative to unit cell height. Indeed, for unit cells with the most narrow electrode spacing and largest electrode width, the capacitance is as much as two orders of magnitude larger than for most of the unit cell designs analyzed in the initial study domain. Comparing this result to the analogy of a parallel-plate capacitor reveals that higher capacitance for the "dense" unit cell designs shouldn't be surprising. Parallel capacitor designs specifying large capacitor plates with small gaps between them result in

a high capacitance system. Similarly, for MFC unit cells implementing small spaces between IDEs and a large electrode surface area relative to the cell size, capacitance of the cell should increase.

Judging from the capacitance plots, for designs where the aspect ratio of the MFC unit cell is within 20% of unity, a wide range of capacitances result from minute variations in MFC electrode width and spacing. To achieve large capacitances or a large range of capacitances, custom designed MFCs should incorporate wide electrodes with center-to-center spacing similar to half of the height of piezoceramic fibers in the MFC. High capacitance MFC designs aren't necessarily undesirable. Power-harvesting studies indicate that the relatively low capacitance of MFCs inhibits the efficacy of these devices in power-harvesting applications. Consequently, the design of high capacitance MFCs would be a boon to this important class of potential MFC applications.

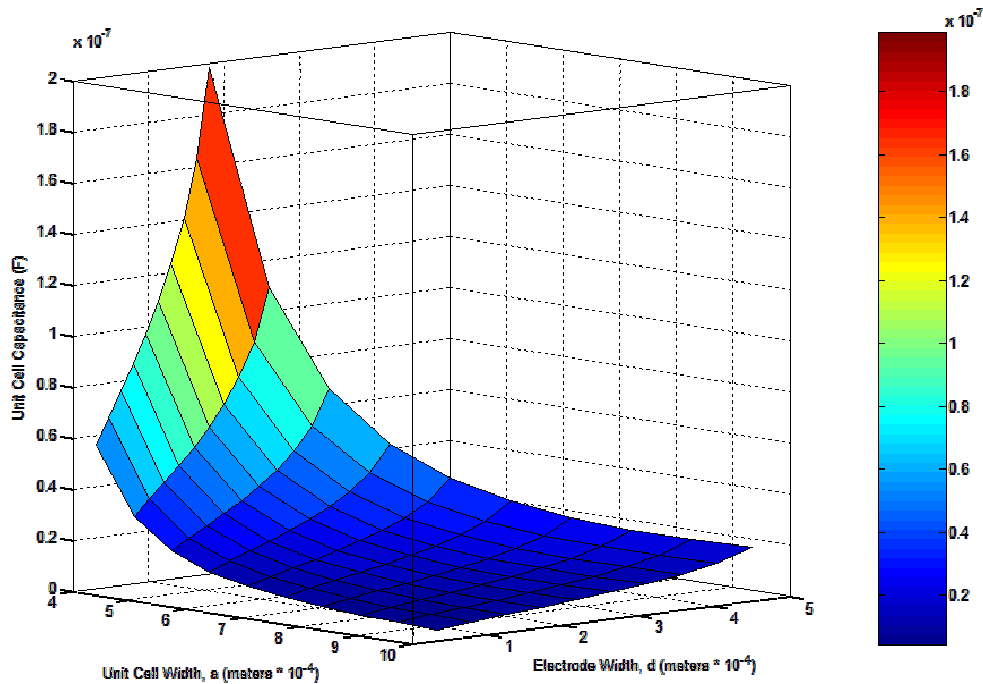


Figure 33: Capacitance of the MFC unit cell as it varies with electrode spacing and electrode width, perspective angle (1) of the refined domain.

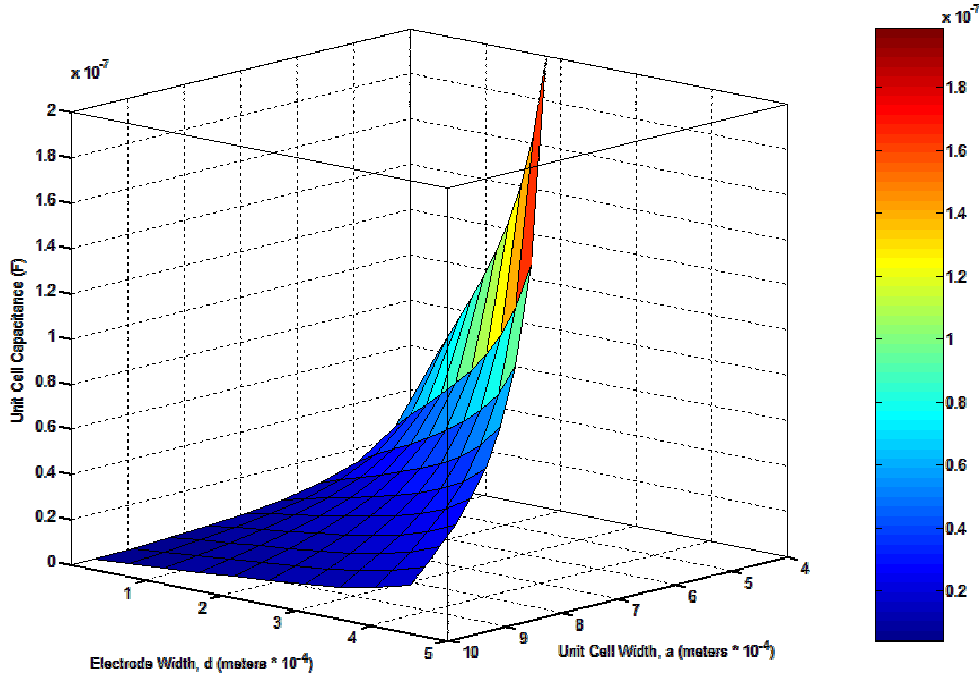


Figure 34: Capacitance of the MFC unit cell as it varies with electrode spacing and electrode width, perspective angle (2) of the refined domain.

It is important to note the association between very intense electrical fields and the high capacitance properties exhibited by certain MFC unit cell designs. Previously discussed, MFC designs corresponding to peaks in the capacitance analysis plots all exhibit especially large electrical field values relative to lower capacitance designs. This outcome, expected due to the cramped spacing of IDEs in the high capacitance designs, potentially limits the actual implementation of the high capacitance designs, which might produce electric fields sufficient to damage the MFC package.

Certainly, the capacitance of the MFC unit cell isn't the only physical characteristic of interest in the conformal mapping study of variant dual IDE designs. Maximizing net strain output performance, perhaps the most important variable in MFC design, is the most obvious goal for an MFC optimization study. MFC strain output dictates the utility of the device in actuation applications and the sensitivity of the package in sensory applications. Modeling both the electric field and polarization field of

the MFC for any design geometry, the conformal mapping solution also offers a means to estimate the strain performance of different MFC designs.

4.3 Variation of MFC Actuation Properties with Respect to IDE Design

Executing an investigative process almost identical to the approach used in the capacitance study, a Mathematica program initialized a 10×10 data matrix representing a continuum of MFC designs in the summarized form of paired electrode width and spacing dimensions. Unit cell dimensions for each test point were identical to those used in the initial survey of capacitance properties for several MFC designs, and an applied differential voltage of 0 V to 1 V was again used in field calculations. For each design, the Mathematica code numerically calculated the electrical and potential field solutions over the corresponding MFC unit cell domain with the mathematical treatment used in the solution of the commercial MFC problem. Pending the determination of the electrical field for each unit cell design, discrete electrical field vectors were used to calculate the elongation of individual subsections of the unit cell domain. After calculating a matrix of displacements, numerical integration of these displacements via summation provided the total displacement of the unit cell. Dividing the total unit cell elongation by the width of the unit cell yielded an effective strain of the unit cell.

Methodical discretization of the unit cell strain problem naturally stemmed from the numerical analysis of the electrical and potential fields of the MFC unit cell. Recalling this approach for the commercial MFC design, a Mathematica code initialized a 15×15 matrix of 2-D spatial coordinates evenly spaced over the breadth of the MFC unit cell domain. For each point, the code numerically calculated the electrical field vector at that location from the conformal mapping equations. Dividing the unit cell domain into a 15×15 mosaic of equally sized rectangular sub-areas positions these electrical field solution points at the center of each area element. Applying this geometric perspective, two approximating assumptions facilitate the discrete solution of the strain problem. First, the discrete computation assumes that the electrical field is uniform throughout each area element and identical to the known field vector at the

center of each element. Second, this analysis assumes that the piezoceramic polarization direction of each area element is perfectly aligned with the electric field vector throughout the area element. Relatively strong, this second assumption follows from the in-situ poling process employed in the manufacturing of the MFC, which guarantees the alignment between the fiber poling and MFC electric field. Under the mechanically static conditions of an ideally in-plane MFC, the electrical field of the IDEs aligns perfectly with the poling direction of the piezoceramic fibers. In reality, affected by an applied voltage, the MFC unit cell deforms and the electrode positions move, deforming the electric field of the MFC unit cell away from the static case of the conformal mapping solution and misaligning the polarization and field vectors. Ignoring this complexity doesn't introduce much error into the strain calculations, however, because the maximum induced strain of standard piezoceramic materials rarely exceeds 0.1%. Also, error due to the finite uniform electric field assumption far exceeds the simplification of the inherent nonlinearities of the unit cell deformation problem.

Multiplication of the magnitude of the electric field vector and the value of the direct effect piezoelectric strain constant (d_{33}) produces the directional strain of each area element. Resolving this strain vector into component vectors of x and y strains and then multiplying those quantities by the width and height of the area elements yields the elongation of individual area elements aligned with the unit cell's x and y axes. Summing these elongations along the "rows" of the lattice, in other words adding the elongations of sub-areas with common y coordinates, results in the total elongation of the unit cell as it changes with respect to unit cell height.

Obtaining a characteristic value for the total strain of the unit cell, even though intuition and calculations show that the unit cell elongation isn't uniform with respect to the y -coordinate, is crucial for a convenient evaluation of IDE designs. Therefore, in this study, the Mathematica code averaged the 15 distinct x -direction elongation computations to arrive at a generalized unit cell elongation. Finally, the code divided this average elongation by the MFC unit cell width to derive an effective unit cell strain. Figure 35 presents the consummation of these extensive mathematical exercises.

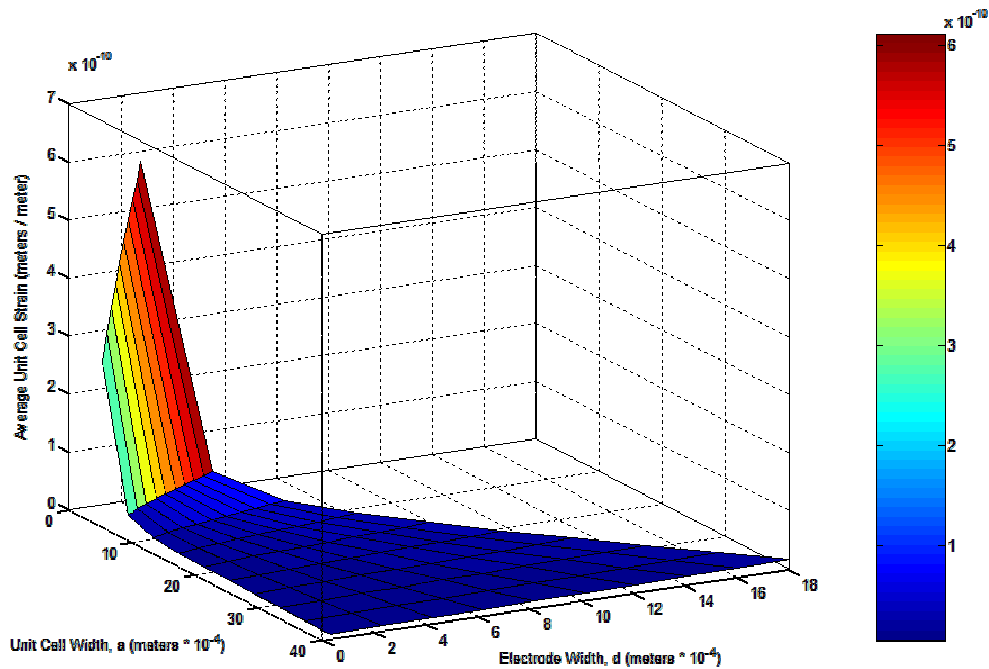


Figure 35: Estimated average induced strain of the MFC unit cell as it varies with electrode spacing and electrode width.

Counterintuitively, the average unit cell strain increases significantly for unit cell designs with closely spaced, wide electrodes, following the trends in capacitance of the unit cells. Especially surprising, this result contradicts the conventional assertion that a large, uniform electric field aligned in the x-direction between MFC electrodes produces superior MFC strain responses. According to this conformal mapping analysis, the highest performing dual IDE designs generate largely misaligned electric fields, with the field streamlines running in elliptical arcs between IDEs. Examining these high-strain IDE geometries more incisively, the Mathematica program calculated the average strains of unit cell designs distinguished by center to center electrode spacing less than 10×10^{-4} meters. Exactly like the “zoom” capacitance plot, the secondary strain plot employed the finer resolution domain grid used in the refined capacitance analysis, providing a smooth graphic of the strain output of compact unit cell designs. Figure 36 contains the focused

strain plot, emphasizing the high strain response of MFC unit cells with wide, closely-spaced IDEs.

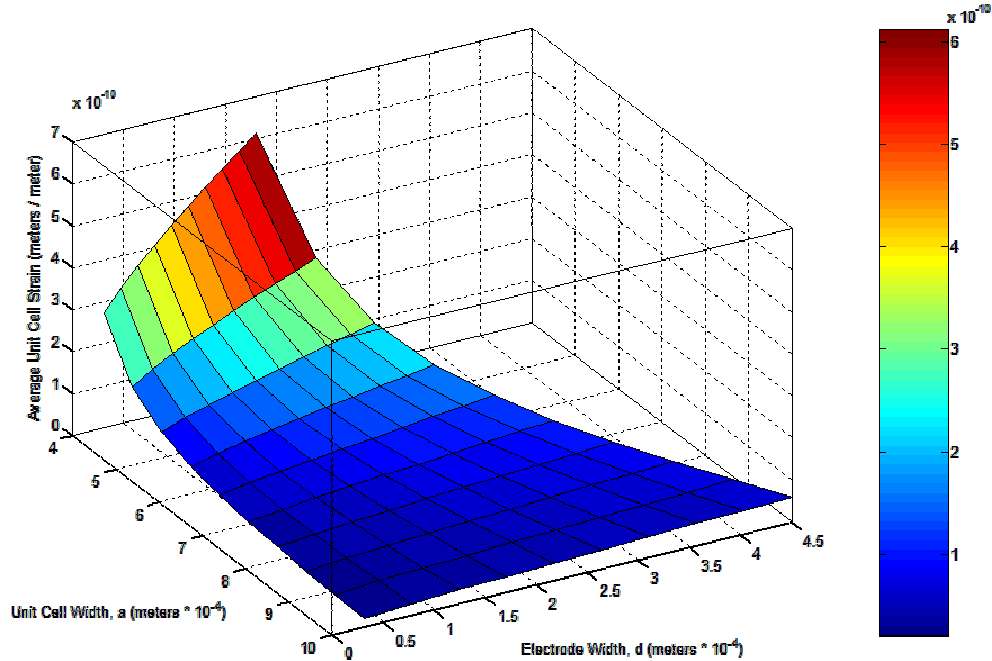


Figure 36: Estimated average induced strain of the MFC unit cell as it varies with electrode spacing and electrode width, refined domain.

Again, behaving in much the same way as the narrow range capacitance plot, the secondary strain plot shows that closely-spaced IDEs that are thin with respect to PZT thickness produce strains up to an order of magnitude larger than IDEs following a more conventional MFC design. An explanation for this phenomenon lies in the large electric fields produced by densely spaced electrodes. Because of the small gaps between equipotential surfaces in these types of IDE designs, the potential field of the MFC unit cell drastically changes over a small distance, resulting in a large potential field gradient and consequently an intense electric field. Stronger electric fields over the MFC unit cell offset inefficiencies created by misalignment of the electric field direction with the global x -direction of the MFC. One cautionary statement concerning a possibly negative byproduct of implementing these high-strain designs should be made. Since the high strength electric field produced by closely spaced, relatively wide IDEs isn't uniform and

in the global x -direction but elliptic in shape with pronounced y -direction components, the y -direction strain of the corresponding MFC unit cell designs is much larger. Large y -direction strains might lead to delamination effects or other types of unusual failure in the MFC package. Furthermore, the same admonitions stated in regards to the implementation of the high-capacitance MFC designs hold here. Unit cell designs producing high average strain estimates correspond to particularly high-electrical field values relative to low strain designs. Large electrical fields, which mitigate the large strains predicted in the analysis of these high-strain designs, might also lead to MFC package damage in actual implementation of these designs.

Contemplation of the utility of the conformal mapping solution in the analysis of the electromechanical properties of different MFC designs exposes the full promise of this analytical model. Multiple calculations of the capacitance and strain output of a plethora of MFC dual-IDE designs suggest that closely-spaced, smaller electrodes, at least relative to the thickness of the MFC's piezoceramic fibers, lead to higher capacitance and higher strain output for the characteristic MFC unit cell. Supported by these calculations, experimentation in the re-design of the MFC dual IDE structure should seek to physically verify these analytical findings and refine the analytical model, if necessary. The following chapter proposes such future research suggestions and recapitulates the findings and conclusions of this study.

Chapter 5

Conclusions

5.1 Problem Overview and Summary of Findings

Layered composite devices, piezoceramic fiber composite (PFC) actuators and sensors boast many advantages over conventional monolithic piezoceramic devices. Conformability is the foremost strength of PFCs, which comprise a layer of multiple piezoceramic fibers imbedded in a flexible matrix, usually epoxy. Developed by MIT researchers, the Active Fiber Composite (AFC) offers the added benefit of higher strain output than monolithic piezoceramics. Composed of cylindrical piezoceramic fibers and an epoxy matrix, the primary innovation of the AFC is the presence of interdigitated electrode (IDE) banks on both sides of the piezoceramic fiber layer. Structured to induce an electric field aligned with the poling direction of the AFC's piezoceramic fibers, the "dual-IDE" design allows the AFC to take advantage of the stronger d_{33} piezoelectric effect, which produces a greater strain in piezoelectric materials.

Capitalizing on the design concepts introduced by the AFC, NASA Langley researchers invented the Macro Fiber Composite (MFC) actuator and sensor. A piezoceramic fiber composite employing a dual-IDE scheme, the MFC design included the notable improvement of rectangular piezoceramic fibers. Fabricated via a quick, cheap dicing of commonly available piezoceramic wafers, rectangular fibers avoid the pitfalls that plague the production of round fibers. Significantly easier to manufacture, rectangular piezoelectric fibers also guaranteed a regular and consistent geometric structure for every MFC, ensuring the repeatable and consistent performance of each MFC and between MFCs of identical dimensions. Overall, the MFC is a superior actuator to the AFC, in terms of both manufacturability and consistent performance.

Past studies of active fiber composites and specifically the MFC concentrated on experimental descriptions of basic engineering parameters, such as bulk mechanical

properties, electrical properties and active strain behavior. Studies that attempted to model AFCs or MFCs exclusively implemented finite element analysis methods, inferring that the complexity of the electrostatics problem embodied by IDE-equipped PFCs is too complicated for explicit analytical techniques. While FEA research efforts produced models that often agreed with experimental strain data, exact solutions for problems such as the polarization field of MFC piezoceramic fibers or the electrical field generated by the dual IDE structure were elusive. Compounding the lack of utile knowledge on the subject of PFC and, specifically, MFC modeling, no published FEA models considered any meaningful applications of FEA findings, failing to capitalize on potential design optimization uses or descriptions of related PFC parameters, such as electrical properties. Also, inherently approximate methods, FEA models lack intuitive explanatory power, deriving results not from sequential elaboration of first principles but from the mathematical estimation of the solutions to well-defined boundary value problems.

Remedying these inadequacies, this research applies the overlooked but extremely powerful analytical method of conformal mapping, delineated from the considerable body of complex analysis theory. An exact method of solving two-dimensional boundary value problems (BVPs), conformal mapping theory provides a tool to transform difficult or complicated BVP geometries into simple geometric configurations having known solutions. After achieving a solution to a given BVP in the simplified problem domain, conformal mapping techniques allow for the reverse transformation of the solution to the original problem geometry, resulting in a solution to the original BVP. Posed in the form of defined complex variable equations, conformal mapping solutions are exact and follow directly from physical first principles.

Conformal mapping theory applies to the class of BVPs called potential problems, which mathematically express electrical and fluid dynamics phenomenon. Naturally, electromagnetic physics describe the physical behavior of the MFC, which mechanically extends due to the interaction of an electric field with piezoceramic fibers. Characterizing the electric field produced by the MFC's dual-IDE configuration

fundamentally explains the essence of the MFC's operation. Poled in-situ, the piezoceramic fibers of the MFC consequently exhibit poling fields commensurate with the directions of the electrostatic field generated by the dual-IDEs. Thus, understanding the electric field of the dual IDE structure automatically leads to knowledge of the polarization field of the piezoelectric MFC components, and finally the interaction between the MFC's electric field and its piezoceramic fibers. Solving the electric field of the dual-IDE structure also directly yields important electrical properties of the MFC, such as capacitance.

Through extensive mathematical machinations, this work applies complex analysis theory, conformal mapping theory and the technique of Schwarz-Christoffel mapping to solve the electrical potential and electrical field problem for the dual-IDE conductor system. Exact and derived from first principles of electrostatic theory, the conformal mapping solution gives an assured means of comparison for previously developed FE models. Arising from the conformal mapping solution to the dual-IDE electric problem, optimization studies of the capacitance and induced strain capabilities of variant MFC designs were conducted. These studies led to new insights into the affects of MFC electrode design on the capacitance and strain response of MFCs.

5.2 Study Contributions

Justification of the creation of an analytical model of MFC physics based on conformal mapping lies in the drawbacks of FEA and the shortcomings of previous MFC modeling studies. Earlier work on the problem of modeling the MFC failed to apply research findings to any constructive analysis of MFC designs and their impact on MFC properties. Furthermore, entirely based on FEA, these investigations were necessarily numerical approximations of MFC behavior, unproven by alternative models and devoid of explanatory power. Systematic and based on definite mathematical expressions of physical laws, conformal mapping clearly displays the connection between the physical parameters of the dual-IDE problem and its eventual mathematical solutions. The conformal mapping solution developed in this work is more computationally efficient

than the tested FEA techniques, reaching large sets of solution data in approximately a third of the time of comparable FEA models. Exact, the conformal mapping solution for the dual-IDE problem also establishes an entirely accurate, precise description of the electrical behavior of the MFC, superceding any type of approximation.

Most importantly, the results of this analysis, conducted on the platform of conformal mapping, contribute potentially useful critiques of MFC performance. Through predicting the relative electrical and strain properties of a continuum of possible but untested MFC designs, the optimization studies of capacitance and induced strain indicate the nature of the dependence of MFC properties on MFC design. Resulting from the high speed and accuracy of the numerical evaluation of the conformal mapping solution equations, it is possible to quickly calculate the electric fields, capacitance and estimated strain response of dozens of different dual-IDE designs. Amassing capacitance and strain response data for a plethora of MFC designs, it is trivial to plot the numerically determined properties as a function of MFC design parameters. Parameter plots of varying capacitance and strain responses provide formidable means to quickly evaluate the relative strengths of different MFC designs and to gain insight into MFC behavior.

Three major contributions of this work will presumably advance research in MFCs and possibly other topics. Summarizing these contributions in no particular order:

1. This study is the first development of a purely analytical model of the electrical potential and electrical fields of the so-called dual-IDE electrode structure. Through application of conformal mapping theory and the concepts of Schwarz-Christoffel mapping, a double mapping sequence was derived to yield a set of closed-form, exact mathematical equations describing the electrical field produced by dual-IDEs. As a consequence of these expressions, the electric potential field, electrical field, polarization field of piezoceramic fibers and the strain field of the MFC can be determined using exact numerical methods. The conformal mapping solution to the dual-IDE problem is computationally faster, more accurate and more intuitive than the only other modeling option, FEA. Crossing over into other fields, this work is the first to analytically

determine the electrostatic solution of the generic dual-IDE system and is also the first derivation of a conformal mapping solution to the unique potential boundary value problem that the MFC physically replicates. As such, it is of corollary interest to the subjects of complex analysis theory and electrostatics research, with possible applications in wave guide design and microwave device design.

2. This research provides the first systematic, analytical inquiry into the dependence of MFC capacitance on dual-IDE geometry. Best viewed as an attempt at optimization, this phase of work provided the capacitances of a continuum of arbitrary MFC designs, evidencing the affect of variations in IDE thickness and spacing on the static capacitance properties of the MFC. Dual-IDE designs producing high and low capacitance qualities were discovered, and general trends in capacitance characteristics depending on the design of dual-IDEs were realized. Specifically, the capacitance data requires the intuitive conclusion that close electrode spacing combined with electrodes that are narrow with respect to piezoceramic fiber thickness results in high capacitance properties. Conversely, widely spaced electrodes that are wide with respect to the piezoceramic fibers result in low capacitance characteristics. Interestingly, the geometric specification of the commercial MFC design fit the criteria shown to engender low capacitance properties. Finally, the capacitance of MFC designs varies drastically with respect to small changes in electrode thickness and spacing when the ratio of center-to-center electrode spacing to half of the piezoceramic fiber thickness approaches unity.

3. This research effort supplies the first systematic, analytical investigation of the strain response of the MFC as a function of dual-IDE geometry. Similar to the case for capacitance, the computational efficiency of the conformal mapping solution enabled the quick numerical estimation of the strain response for a large range of possible MFC designs. Plotting the MFC's strain response with characteristic dual-IDE dimensions facilitated an assessment of the affect of MFC design on MFC strain properties. Surprisingly, the strain estimation data indicates that, once again, condensed dual-IDE designs for the MFC lead to a higher average strain response. Thus, IDE designs comprising closely spaced electrodes that are narrow relative to the MFC's piezoceramic

fibers exhibit larger strain responses than designs with widely spaced, wide electrodes. Numerical simulations of the tested MFC designs resulted in large differences between the estimated average induced strains of different MFC versions, with strains sometimes varying by more than an order of magnitude. Obeying the same type of trends seen in the capacitance plots, the greatest changes in the calculated average induced strains occurred when the ratio of center-to-center electrode spacing to half of the piezoceramic fiber width approaches unity. Interestingly, the current commercial MFC design exhibits the same general geometric properties of dual-IDE configurations producing small strains.

Substantial additions to the body of knowledge on MFC technology, these unique aspects of the current MFC study pave the way for more elaborate and comparably useful endeavors. Research and commercial extensions of this work promise to improve the design of future MFC actuators and to hone the explanation of MFC functionality. Suggestions for the application of this inquiry and for its continuation and embellishment follow.

5.3 Recommendations for Future Work

Contemplating the possibilities for further developments based on this study, appreciable potential exists in both experimentation and more complicated modeling exercises. Exploration of the experimental avenues opened by this work should initially consist of the laboratory testing of representative prototypes that are assembled according to the enclosed findings. Most importantly, several physical MFC prototypes, exemplifying particular regions of the capacitance and strain data plots, should be fabricated and tested to corroborate the predictions offered in this analytical treatment. No explicit attempt was made to match the MFC properties projected by this research to experimental data. If, at least, the relative properties of the different MFC designs correspond between this study and real-world MFCs, then considerable room for improvement exists in MFC designs.

Notable among the tested geometries, the dual-IDE design coupling the narrowest calculated unit cell with the greatest allowed electrode coverage, 95% of the width of the unit cell, should be constructed and physically tested for capacitance and strain properties. Epitomizing the “compact” MFC design, this design applies the narrow center-to-center electrode spacing and wide electrode dimensions, relative to spacing, shown via the model calculations to result in high capacitance, high strain performance. Providing an extreme comparison, experiments should also build and test MFCs that embody unit cell design regimes contrary to the compact MFC design. More similar to the commercial MFC design, an MFC combining extremely wide unit cells with narrow electrodes, less than 5% of the unit cell width, should be constructed and tested. Presumably, this prototype, with widely spaced, thin electrodes, will possess much lower capacitance and induced strain than its compact design counterpart. Of course, because of the large electrical fields calculated for the large strain and high capacitance MFC designs, actual prototypes constructed to these design specifications may prove impractical in real world conditions. High voltage actuation of these particular designs could produce electrical fields sufficiently large to damage the MFC prototype packages, whereas similar voltages wouldn't damage conventional MFC designs. Evaluation of the feasibility of the high-capacitance and high-strain MFC designs with concern towards the practical aspects of MFC application is another reason for the experimental testing of these findings.

Pending the experimental verification of, minimally, the projected relative properties of various MFC designs, the next logical pursuit is the refinement of the current analytical model through comparison of the quantitative predictions of MFC properties to experimentally measured values. Assuming that this model doesn't accurately yield the specific overall values for static MFC capacitance and strain, all possible action should be taken to realize why the experimental and analytical parameters don't coincide. Possibly, efforts to incorporate corrections for fringing effects, three-dimensional effects and unmodeled nonlinearities will improve any modeling inadequacies. Neglecting the important nonlinearity of imperfect alignment between the MFC's electric field and piezoelectric polarization field probably inculcates the greatest

degree of modeling inaccuracy to the conformal mapping capacitance and strain solutions. Determining a way to account for this problem is one immediately evident means to improve the conformal mapping solution. Even if the analytical limits of the model restrict improving augmentations within the context of a consistently analytical solution, alternatively integrating the conformal mapping solution method to finite element type codes might result in an accurate hybrid solution, potentially more flexible and applicable to complex MFC behavior.

A final consideration in the study of the conformal mapping solution in the immediate future is the current inapplicability of the model to the dynamic operation of the MFC. In this study, static assumptions were necessary to simplify the calculation of capacitance and strain properties using the conformal mapping model. Also, conformal mapping techniques traditionally apply to implicitly static potential problems, with electrostatic equations underlying all formula derivations. By using the information supplied by this model on the electric field of the dual-IDE system and known relationships between static electrical properties and dynamic electrical properties, research should attempt to relate the current model to MFC dynamics. Possibly, simplifying assumptions on the linearity of the MFC problem will apply to this process and allow relatively simple analytical formulations describing and forecasting dynamic MFC behavior.

5.4 Concluding Remarks

Considering the original goals of this project, the development and implementation of the conformal mapping solution to the MFC's dual-IDE electrical field problem was a successful exercise, producing several useful computational results and spawning many possibilities for continued research. Insights into MFC behavior and operation were achieved, and the mathematical methods and electrostatic equations contrived to solve the dual-IDE field problem contribute to the fields of complex analysis and electrostatics. Future application and development of this work will undoubtedly improve MFC technology and lead to continued advancement in piezoelectric fiber composite devices.

Appendix A

Commercial MFC Electrical Field Values

(z-plane)	y (z-plane)	Ex	Ey	E	P
meters * 10 ⁻⁴	meters * 10 ⁻⁴	V/m	V/m	V/m	V
0.1667	0.0267	440.32	-69.60	445.79	0.9139
0.5000	0.0267	1240.03	-54.90	1241.25	0.8854
0.8333	0.0267	1753.67	-27.23	1753.88	0.8345
1.1667	0.0267	1966.03	-9.26	1966.05	0.7719
1.5000	0.0267	2032.70	-2.68	2032.70	0.7051
1.8333	0.0267	2051.50	-0.74	2051.50	0.6370
2.1667	0.0267	2056.54	-0.19	2056.54	0.5685
2.5000	0.0267	2057.56	0.00	2057.56	0.5000
2.8333	0.0267	2056.54	0.19	2056.54	0.4315
3.1667	0.0267	2051.50	0.74	2051.50	0.3630
3.5000	0.0267	2032.70	2.68	2032.70	0.2949
3.8333	0.0267	1966.03	9.26	1966.05	0.2281
4.1667	0.0267	1753.67	27.23	1753.88	0.1655
4.5000	0.0267	1240.03	54.90	1241.25	0.1146
4.8333	0.0267	440.32	69.60	445.79	0.0861
0.1667	0.0800	442.01	-209.15	488.99	0.9146
0.5000	0.0800	1247.98	-165.14	1258.86	0.8860
0.8333	0.0800	1761.79	-81.34	1763.66	0.8348
1.1667	0.0800	1969.53	-27.50	1969.73	0.7720
1.5000	0.0800	2033.78	-7.94	2033.80	0.7051
1.8333	0.0800	2051.80	-2.17	2051.80	0.6370
2.1667	0.0800	2056.63	-0.55	2056.63	0.5685
2.5000	0.0800	2057.61	0.00	2057.61	0.5000
2.8333	0.0800	2056.63	0.55	2056.63	0.4315
3.1667	0.0800	2051.80	2.17	2051.80	0.3630
3.5000	0.0800	2033.78	7.94	2033.80	0.2949
3.8333	0.0800	1969.53	27.50	1969.73	0.2280
4.1667	0.0800	1761.79	81.34	1763.66	0.1652
4.5000	0.0800	1247.98	165.14	1258.86	0.1140
4.8333	0.0800	442.01	209.15	488.99	0.0854
0.1667	0.1333	445.23	-349.76	566.18	0.9161
0.5000	0.1333	1264.11	-276.71	1294.04	0.8872
0.8333	0.1333	1778.14	-134.41	1783.22	0.8354
1.1667	0.1333	1976.47	-44.83	1976.98	0.7722
1.5000	0.1333	2035.92	-12.88	2035.96	0.7052
1.8333	0.1333	2052.40	-3.52	2052.41	0.6370
2.1667	0.1333	2056.81	-0.89	2056.81	0.5686
2.5000	0.1333	2057.69	0.00	2057.69	0.5000
2.8333	0.1333	2056.81	0.89	2056.81	0.4314
3.1667	0.1333	2052.40	3.52	2052.41	0.3630

3.5000	0.1333	2035.92	12.88	2035.96	0.2948
3.8333	0.1333	1976.47	44.83	1976.98	0.2278
4.1667	0.1333	1778.14	134.41	1783.22	0.1646
4.5000	0.1333	1264.11	276.71	1294.04	0.1128
4.8333	0.1333	445.23	349.76	566.18	0.0839
0.1667	0.1867	449.66	-492.11	666.61	0.9184
0.5000	0.1867	1288.87	-390.62	1346.76	0.8889
0.8333	0.1867	1802.97	-185.63	1812.50	0.8363
1.1667	0.1867	1986.68	-60.67	1987.60	0.7725
1.5000	0.1867	2039.02	-17.29	2039.10	0.7053
1.8333	0.1867	2053.27	-4.72	2053.28	0.6370
2.1667	0.1867	2057.06	-1.19	2057.06	0.5686
2.5000	0.1867	2057.82	0.00	2057.82	0.5000
2.8333	0.1867	2057.06	1.19	2057.06	0.4314
3.1667	0.1867	2053.27	4.72	2053.28	0.3630
3.5000	0.1867	2039.02	17.29	2039.10	0.2947
3.8333	0.1867	1986.68	60.67	1987.60	0.2275
4.1667	0.1867	1802.97	185.63	1812.50	0.1637
4.5000	0.1867	1288.87	390.62	1346.76	0.1111
4.8333	0.1867	449.66	492.11	666.61	0.0816
0.1667	0.2400	454.73	-636.82	782.51	0.9214
0.5000	0.2400	1323.03	-508.13	1417.25	0.8913
0.8333	0.2400	1836.60	-234.01	1851.45	0.8374
1.1667	0.2400	1999.92	-74.41	2001.30	0.7729
1.5000	0.2400	2042.98	-20.99	2043.08	0.7054
1.8333	0.2400	2054.38	-5.71	2054.38	0.6371
2.1667	0.2400	2057.38	-1.44	2057.38	0.5686
2.5000	0.2400	2057.98	0.00	2057.98	0.5000
2.8333	0.2400	2057.38	1.44	2057.38	0.4314
3.1667	0.2400	2054.38	5.71	2054.38	0.3629
3.5000	0.2400	2042.98	20.99	2043.08	0.2946
3.8333	0.2400	1999.92	74.41	2001.30	0.2271
4.1667	0.2400	1836.60	234.01	1851.45	0.1626
4.5000	0.2400	1323.03	508.13	1417.25	0.1087
4.8333	0.2400	454.73	636.82	782.51	0.0786
0.1667	0.2933	459.54	-784.37	909.07	0.9252
0.5000	0.2933	1367.77	-630.84	1506.24	0.8944
0.8333	0.2933	1879.42	-278.30	1899.91	0.8387
1.1667	0.2933	2015.83	-85.48	2017.64	0.7733
1.5000	0.2933	2047.62	-23.82	2047.76	0.7055
1.8333	0.2933	2055.66	-6.46	2055.67	0.6371
2.1667	0.2933	2057.75	-1.63	2057.75	0.5686
2.5000	0.2933	2058.17	0.00	2058.17	0.5000
2.8333	0.2933	2057.75	1.63	2057.75	0.4314
3.1667	0.2933	2055.66	6.46	2055.67	0.3629
3.5000	0.2933	2047.62	23.82	2047.76	0.2945
3.8333	0.2933	2015.83	85.48	2017.64	0.2267

4.1667	0.2933	1879.42	278.30	1899.91	0.1613
4.5000	0.2933	1367.77	630.84	1506.24	0.1056
4.8333	0.2933	459.54	784.37	909.07	0.0748
0.1667	0.3467	462.73	-935.05	1043.29	0.9297
0.5000	0.3467	1424.89	-760.96	1615.35	0.8981
0.8333	0.3467	1931.82	-316.84	1957.63	0.8403
1.1667	0.3467	2033.95	-93.30	2036.09	0.7738
1.5000	0.3467	2052.78	-25.64	2052.94	0.7056
1.8333	0.3467	2057.08	-6.92	2057.09	0.6371
2.1667	0.3467	2058.16	-1.74	2058.16	0.5686
2.5000	0.3467	2058.38	0.00	2058.38	0.5000
2.8333	0.3467	2058.16	1.74	2058.16	0.4314
3.1667	0.3467	2057.08	6.92	2057.09	0.3629
3.5000	0.3467	2052.78	25.64	2052.94	0.2944
3.8333	0.3467	2033.95	93.30	2036.09	0.2262
4.1667	0.3467	1931.82	316.84	1957.63	0.1597
4.5000	0.3467	1424.89	760.96	1615.35	0.1019
4.8333	0.3467	462.73	935.05	1043.29	0.0703
0.1667	0.4000	462.33	-1088.77	1182.86	0.9351
0.5000	0.4000	1497.10	-901.70	1747.67	0.9025
0.8333	0.4000	1994.04	-347.44	2024.08	0.8421
1.1667	0.4000	2053.66	-97.38	2055.97	0.7743
1.5000	0.4000	2058.23	-26.37	2058.40	0.7058
1.8333	0.4000	2058.57	-7.09	2058.58	0.6372
2.1667	0.4000	2058.59	-1.78	2058.59	0.5686
2.5000	0.4000	2058.59	0.00	2058.59	0.5000
2.8333	0.4000	2058.59	1.78	2058.59	0.4314
3.1667	0.4000	2058.57	7.09	2058.58	0.3628
3.5000	0.4000	2058.23	26.37	2058.40	0.2942
3.8333	0.4000	2053.66	97.38	2055.97	0.2257
4.1667	0.4000	1994.04	347.44	2024.08	0.1579
4.5000	0.4000	1497.10	901.70	1747.67	0.0975
4.8333	0.4000	462.33	1088.77	1182.86	0.0649
0.1667	0.4533	455.51	-1244.77	1325.50	0.9414
0.5000	0.4533	1588.71	-1057.96	1908.74	0.9077
0.8333	0.4533	2065.93	-367.20	2098.31	0.8440
1.1667	0.4533	2074.22	-97.30	2076.50	0.7748
1.5000	0.4533	2063.75	-25.94	2063.91	0.7059
1.8333	0.4533	2060.06	-6.94	2060.07	0.6372
2.1667	0.4533	2059.02	-1.75	2059.02	0.5686
2.5000	0.4533	2058.81	0.00	2058.81	0.5000
2.8333	0.4533	2059.02	1.75	2059.02	0.4314
3.1667	0.4533	2060.06	6.94	2060.07	0.3628
3.5000	0.4533	2063.75	25.94	2063.91	0.2941
3.8333	0.4533	2074.22	97.30	2076.50	0.2252
4.1667	0.4533	2065.93	367.20	2098.31	0.1560
4.5000	0.4533	1588.71	1057.96	1908.74	0.0923

4.8333	0.4533	455.51	1244.77	1325.50	0.0586
0.1667	0.5067	438.52	-1401.22	1468.24	0.9484
0.5000	0.5067	1706.89	-1237.66	2108.39	0.9138
0.8333	0.5067	2146.51	-372.43	2178.58	0.8460
1.1667	0.5067	2094.73	-92.80	2096.78	0.7753
1.5000	0.5067	2069.08	-24.36	2069.23	0.7060
1.8333	0.5067	2061.49	-6.49	2061.50	0.6373
2.1667	0.5067	2059.43	-1.63	2059.43	0.5686
2.5000	0.5067	2059.02	0.00	2059.02	0.5000
2.8333	0.5067	2059.43	1.63	2059.43	0.4314
3.1667	0.5067	2061.49	6.49	2061.50	0.3627
3.5000	0.5067	2069.08	24.36	2069.23	0.2940
3.8333	0.5067	2094.73	92.80	2096.78	0.2247
4.1667	0.5067	2146.51	372.43	2178.58	0.1540
4.5000	0.5067	1706.89	1237.66	2108.39	0.0862
4.8333	0.5067	438.52	1401.22	1468.24	0.0516
0.1667	0.5600	406.69	-1554.51	1606.83	0.9563
0.5000	0.5600	1864.43	-1454.69	2364.79	0.9210
0.8333	0.5600	2233.29	-358.75	2261.92	0.8480
1.1667	0.5600	2114.18	-83.81	2115.84	0.7758
1.5000	0.5600	2073.99	-21.68	2074.10	0.7062
1.8333	0.5600	2062.80	-5.76	2062.81	0.6373
2.1667	0.5600	2059.81	-1.45	2059.81	0.5686
2.5000	0.5600	2059.21	0.00	2059.21	0.5000
2.8333	0.5600	2059.81	1.45	2059.81	0.4314
3.1667	0.5600	2062.80	5.76	2062.81	0.3627
3.5000	0.5600	2073.99	21.68	2074.10	0.2938
3.8333	0.5600	2114.18	83.81	2115.84	0.2242
4.1667	0.5600	2233.29	358.76	2261.92	0.1520
4.5000	0.5600	1864.43	1454.69	2364.79	0.0790
4.8333	0.5600	406.69	1554.51	1606.83	0.0437
0.1667	0.6133	355.07	-1698.45	1735.16	0.9650
0.5000	0.6133	2086.66	-1736.12	2714.46	0.9294
0.8333	0.6133	2321.41	-321.69	2343.59	0.8498
1.1667	0.6133	2131.51	-70.52	2132.68	0.7762
1.5000	0.6133	2078.24	-18.01	2078.32	0.7063
1.8333	0.6133	2063.92	-4.77	2063.93	0.6373
2.1667	0.6133	2060.13	-1.20	2060.13	0.5686
2.5000	0.6133	2059.37	0.00	2059.37	0.5000
2.8333	0.6133	2060.13	1.20	2060.13	0.4314
3.1667	0.6133	2063.92	4.77	2063.93	0.3627
3.5000	0.6133	2078.24	18.01	2078.32	0.2937
3.8333	0.6133	2131.51	70.52	2132.68	0.2238
4.1667	0.6133	2321.41	321.69	2343.59	0.1502
4.5000	0.6133	2086.66	1736.12	2714.46	0.0706
4.8333	0.6133	355.07	1698.45	1735.16	0.0350
0.1667	0.6667	279.78	-1823.66	1845.00	0.9744

0.5000	0.6667	2432.72	-2144.05	3242.70	0.9397
0.8333	0.6667	2402.97	-258.05	2416.78	0.8513
1.1667	0.6667	2145.65	-53.44	2146.32	0.7765
1.5000	0.6667	2081.63	-13.50	2081.68	0.7064
1.8333	0.6667	2064.81	-3.57	2064.81	0.6373
2.1667	0.6667	2060.38	-0.89	2060.38	0.5686
2.5000	0.6667	2059.50	0.00	2059.50	0.5000
2.8333	0.6667	2060.38	0.89	2060.38	0.4314
3.1667	0.6667	2064.81	3.57	2064.81	0.3627
3.5000	0.6667	2081.63	13.50	2081.68	0.2936
3.8333	0.6667	2145.65	53.44	2146.32	0.2235
4.1667	0.6667	2402.97	258.05	2416.78	0.1487
4.5000	0.6667	2432.72	2144.05	3242.70	0.0603
4.8333	0.6667	279.78	1823.66	1845.00	0.0256
0.1667	0.7200	180.44	-1918.04	1926.51	0.9844
0.5000	0.7200	3086.41	-2868.94	4213.88	0.9528
0.8333	0.7200	2467.25	-168.25	2472.98	0.8525
1.1667	0.7200	2155.68	-33.35	2155.94	0.7768
1.5000	0.7200	2083.99	-8.37	2084.01	0.7064
1.8333	0.7200	2065.43	-2.21	2065.43	0.6374
2.1667	0.7200	2060.56	-0.55	2060.56	0.5686
2.5000	0.7200	2059.58	0.00	2059.58	0.5000
2.8333	0.7200	2060.56	0.55	2060.56	0.4314
3.1667	0.7200	2065.43	2.21	2065.43	0.3626
3.5000	0.7200	2083.99	8.37	2084.01	0.2936
3.8333	0.7200	2155.68	33.35	2155.94	0.2232
4.1667	0.7200	2467.25	168.25	2472.98	0.1475
4.5000	0.7200	3086.41	2868.94	4213.88	0.0472
4.8333	0.7200	180.44	1918.04	1926.51	0.0156
0.1667	0.7733	62.51	-1969.27	1970.26	0.9947
0.5000	0.7733	5230.54	-5125.14	7322.96	0.9726
0.8333	0.7733	2503.11	-58.58	2503.79	0.8531
1.1667	0.7733	2160.88	-11.34	2160.91	0.7769
1.5000	0.7733	2085.20	-2.83	2085.20	0.7064
1.8333	0.7733	2065.74	-0.75	2065.74	0.6374
2.1667	0.7733	2060.65	-0.19	2060.65	0.5686
2.5000	0.7733	2059.63	0.00	2059.63	0.5000
2.8333	0.7733	2060.65	0.19	2060.65	0.4314
3.1667	0.7733	2065.74	0.75	2065.74	0.3626
3.5000	0.7733	2085.20	2.83	2085.20	0.2936
3.8333	0.7733	2160.88	11.34	2160.91	0.2231
4.1667	0.7733	2503.11	58.58	2503.79	0.1469
4.5000	0.7733	5230.54	5125.13	7322.94	0.0274
4.8333	0.7733	62.51	1969.27	1970.26	0.0053

Appendix B

Capacitance Values of Alternate MFC Designs

a	d	k	p	Capacitance	Strain
meters * 10 ⁻⁴	meters * 10 ⁻⁴			F	m/m
4	0.31	0.078689	13.093233	5.59E-08	2.75E-10
4	0.48	0.078689	13.646430	6.62E-08	3.24E-10
4	0.64	0.078689	14.503740	7.61E-08	3.66E-10
4	0.81	0.078689	15.759839	8.62E-08	4.06E-10
4	0.97	0.078689	17.579480	9.71E-08	4.43E-10
4	1.14	0.078689	20.261984	1.09E-07	4.79E-10
4	1.30	0.078689	24.398795	1.23E-07	5.14E-10
4	1.47	0.078689	31.326667	1.40E-07	5.48E-10
4	1.63	0.078689	44.813001	1.63E-07	5.81E-10
4	1.80	0.078689	81.113727	1.99E-07	6.12E-10
8	0.31	0.520105	1.934901	6.62E-09	3.24E-11
8	0.68	0.520105	1.982214	8.49E-09	4.15E-11
8	1.04	0.520105	2.070784	1.01E-08	4.83E-11
8	1.41	0.520105	2.212403	1.17E-08	5.43E-11
8	1.77	0.520105	2.428778	1.33E-08	5.99E-11
8	2.14	0.520105	2.760433	1.52E-08	6.52E-11
8	2.50	0.520105	3.288990	1.73E-08	7.05E-11
8	2.87	0.520105	4.202959	2.00E-08	7.58E-11
8	3.23	0.520105	6.052262	2.36E-08	8.11E-11
8	3.60	0.520105	11.398840	2.93E-08	8.63E-11
12	0.31	0.831467	1.204810	3.51E-09	1.68E-11
12	0.88	0.831467	1.220071	4.67E-09	2.24E-11
12	1.44	0.831467	1.252512	5.59E-09	2.63E-11
12	2.01	0.831467	1.307987	6.46E-09	2.93E-11
12	2.57	0.831467	1.397549	7.39E-09	3.24E-11
12	3.14	0.831467	1.542014	8.43E-09	3.51E-11
12	3.70	0.831467	1.783444	9.68E-09	3.80E-11
12	4.27	0.831467	2.219301	1.13E-08	4.10E-11
12	4.83	0.831467	3.136190	1.35E-08	4.40E-11
12	5.40	0.831467	5.900224	1.71E-08	4.71E-11
16	0.31	0.948860	1.054423	2.68E-09	1.27E-11
16	1.08	0.948860	1.060479	3.62E-09	1.71E-11
16	1.84	0.948860	1.074773	4.30E-09	2.00E-11
16	2.61	0.948860	1.101122	4.95E-09	2.21E-11
16	3.37	0.948860	1.146986	5.64E-09	2.43E-11
16	4.14	0.948860	1.226722	6.44E-09	2.62E-11
16	4.90	0.948860	1.369722	7.43E-09	2.84E-11
16	5.67	0.948860	1.644525	8.73E-09	3.07E-11
16	6.43	0.948860	2.253523	1.06E-08	3.30E-11
16	7.20	0.948860	4.171147	1.37E-08	3.54E-11
20	0.31	0.985171	1.015196	2.28E-09	1.07E-11

20	1.28	0.985171	1.017623	3.09E-09	1.45E-11
20	2.24	0.985171	1.023935	3.64E-09	1.69E-11
20	3.21	0.985171	1.036634	4.16E-09	1.84E-11
20	4.17	0.985171	1.060914	4.73E-09	2.02E-11
20	5.14	0.985171	1.107307	5.40E-09	2.17E-11
20	6.10	0.985171	1.198243	6.26E-09	2.35E-11
20	7.07	0.985171	1.387242	7.43E-09	2.54E-11
20	8.03	0.985171	1.833918	9.16E-09	2.73E-11
20	9.00	0.985171	3.311838	1.22E-08	2.95E-11
24	0.31	0.995757	1.004302	2.03E-09	9.44E-12
24	1.48	0.995757	1.005247	2.74E-09	1.28E-11
24	2.64	0.995757	1.007947	3.19E-09	1.47E-11
24	3.81	0.995757	1.013941	3.62E-09	1.59E-11
24	4.97	0.995757	1.026697	4.11E-09	1.75E-11
24	6.14	0.995757	1.053836	4.70E-09	1.86E-11
24	7.30	0.995757	1.112719	5.47E-09	2.02E-11
24	8.47	0.995757	1.246705	6.55E-09	2.19E-11
24	9.63	0.995757	1.588034	8.18E-09	2.35E-11
24	10.80	0.995757	2.782985	1.11E-08	2.54E-11
28	0.31	0.998791	1.001222	1.83E-09	8.49E-12
28	1.68	0.998791	1.001579	2.46E-09	1.14E-11
28	3.04	0.998791	1.002698	2.84E-09	1.31E-11
28	4.41	0.998791	1.005461	3.21E-09	1.40E-11
28	5.77	0.998791	1.012058	3.63E-09	1.54E-11
28	7.14	0.998791	1.027812	4.16E-09	1.63E-11
28	8.50	0.998791	1.065972	4.86E-09	1.77E-11
28	9.87	0.998791	1.161924	5.87E-09	1.92E-11
28	11.23	0.998791	1.427853	7.43E-09	2.06E-11
28	12.60	0.998791	2.419858	1.03E-08	2.24E-11
32	0.31	0.999656	1.000348	1.67E-09	7.73E-12
32	1.88	0.999656	1.000479	2.23E-09	1.03E-11
32	3.44	0.999656	1.000931	2.56E-09	1.18E-11
32	5.01	0.999656	1.002179	2.88E-09	1.25E-11
32	6.57	0.999656	1.005540	3.25E-09	1.37E-11
32	8.14	0.999656	1.014588	3.73E-09	1.45E-11
32	9.70	0.999656	1.039193	4.37E-09	1.58E-11
32	11.27	0.999656	1.108045	5.31E-09	1.71E-11
32	12.83	0.999656	1.317282	6.80E-09	1.84E-11
32	14.40	0.999656	2.154604	9.60E-09	2.00E-11
36	0.31	0.999902	1.000099	1.54E-09	7.10E-12
36	2.08	0.999902	1.000146	2.04E-09	9.40E-12
36	3.84	0.999902	1.000325	2.32E-09	1.07E-11
36	5.61	0.999902	1.000880	2.60E-09	1.13E-11
36	7.37	0.999902	1.002570	2.94E-09	1.23E-11
36	9.14	0.999902	1.007713	3.37E-09	1.30E-11
36	10.90	0.999902	1.023470	3.97E-09	1.42E-11
36	12.67	0.999902	1.072800	4.85E-09	1.53E-11
36	14.43	0.999902	1.238264	6.27E-09	1.65E-11

36	16.20	0.999902	1.953080	9.00E-09	1.80E-11
40	0.31	0.999972	1.000028	1.43E-09	6.57E-12
40	2.28	0.999972	1.000045	1.87E-09	8.62E-12
40	4.24	0.999972	1.000115	2.12E-09	9.73E-12
40	6.21	0.999972	1.000359	2.37E-09	1.03E-11
40	8.17	0.999972	1.001199	2.67E-09	1.12E-11
40	10.14	0.999972	1.004095	3.07E-09	1.18E-11
40	12.10	0.999972	1.014116	3.63E-09	1.29E-11
40	14.07	0.999972	1.049350	4.46E-09	1.39E-11
40	16.03	0.999972	1.180506	5.81E-09	1.50E-11
40	18.00	0.999972	1.795701	8.48E-09	1.64E-11

Appendix C

Estimated Average Strain Values of Alternate MFC Designs

a	d	k	p	Capacitance	Strain
meters * 10 ⁻⁴	meters * 10 ⁻⁴			F	m/m
4.00	0.31	0.078689	13.093233	5.59E-08	2.75E-10
4.00	0.48	0.078689	13.646430	6.62E-08	3.24E-10
4.00	0.64	0.078689	14.503740	7.61E-08	3.66E-10
4.00	0.81	0.078689	15.759839	8.62E-08	4.06E-10
4.00	0.97	0.078689	17.579480	9.71E-08	4.43E-10
4.00	1.14	0.078689	20.261984	1.09E-07	4.79E-10
4.00	1.30	0.078689	24.398795	1.23E-07	5.14E-10
4.00	1.47	0.078689	31.326667	1.40E-07	5.48E-10
4.00	1.63	0.078689	44.813001	1.63E-07	5.81E-10
4.00	1.80	0.078689	81.113727	1.99E-07	6.12E-10
4.67	0.31	0.137455	7.434935	3.03E-08	1.50E-10
4.67	0.51	0.137455	7.719799	3.65E-08	1.80E-10
4.67	0.71	0.137455	8.178807	4.23E-08	2.05E-10
4.67	0.91	0.137455	8.864302	4.82E-08	2.28E-10
4.67	1.11	0.137455	9.868607	5.45E-08	2.50E-10
4.67	1.30	0.137455	11.360637	6.16E-08	2.71E-10
4.67	1.50	0.137455	13.676353	6.97E-08	2.92E-10
4.67	1.70	0.137455	17.580019	7.96E-08	3.12E-10
4.67	1.90	0.137455	25.248561	9.29E-08	3.31E-10
4.67	2.10	0.137455	46.290227	1.14E-07	3.50E-10
5.33	0.31	0.208052	4.885976	1.91E-08	9.47E-11
5.33	0.54	0.208052	5.057039	2.34E-08	1.15E-10
5.33	0.77	0.208052	5.342582	2.73E-08	1.33E-10
5.33	1.01	0.208052	5.776834	3.12E-08	1.48E-10
5.33	1.24	0.208052	6.417369	3.55E-08	1.63E-10
5.33	1.47	0.208052	7.376365	4.01E-08	1.77E-10
5.33	1.70	0.208052	8.872805	4.55E-08	1.90E-10
5.33	1.94	0.208052	11.409064	5.22E-08	2.04E-10
5.33	2.17	0.208052	16.426860	6.10E-08	2.17E-10
5.33	2.40	0.208052	30.396395	7.48E-08	2.30E-10
6.00	0.31	0.285700	3.544860	1.34E-08	6.61E-11
6.00	0.58	0.285700	3.658596	1.66E-08	8.17E-11
6.00	0.84	0.285700	3.854668	1.95E-08	9.43E-11
6.00	1.11	0.285700	4.156709	2.24E-08	1.06E-10
6.00	1.37	0.285700	4.607260	2.54E-08	1.16E-10
6.00	1.64	0.285700	5.285434	2.88E-08	1.26E-10
6.00	1.90	0.285700	6.348843	3.28E-08	1.36E-10
6.00	2.17	0.285700	8.159895	3.76E-08	1.46E-10
6.00	2.43	0.285700	11.765186	4.41E-08	1.56E-10
6.00	2.70	0.285700	21.918317	5.43E-08	1.65E-10
6.67	0.31	0.365915	2.760247	1.01E-08	4.96E-11

6.67	0.61	0.365915	2.841380	1.26E-08	6.21E-11
6.67	0.91	0.365915	2.985442	1.49E-08	7.20E-11
6.67	1.21	0.365915	3.210329	1.72E-08	8.07E-11
6.67	1.51	0.365915	3.548559	1.96E-08	8.89E-11
6.67	1.80	0.365915	4.060513	2.22E-08	9.68E-11
6.67	2.10	0.365915	4.867448	2.53E-08	1.04E-10
6.67	2.40	0.365915	6.248403	2.91E-08	1.12E-10
6.67	2.70	0.365915	9.012403	3.42E-08	1.20E-10
6.67	3.00	0.365915	16.873517	4.22E-08	1.27E-10
7.33	0.31	0.444981	2.265148	7.99E-09	3.93E-11
7.33	0.64	0.444981	2.325990	1.01E-08	4.97E-11
7.33	0.97	0.444981	2.437018	1.20E-08	5.78E-11
7.33	1.31	0.444981	2.612489	1.39E-08	6.49E-11
7.33	1.64	0.444981	2.878471	1.58E-08	7.16E-11
7.33	1.97	0.444981	3.283536	1.80E-08	7.79E-11
7.33	2.30	0.444981	3.925398	2.05E-08	8.42E-11
7.33	2.64	0.444981	5.029349	2.36E-08	9.05E-11
7.33	2.97	0.444981	7.250914	2.78E-08	9.67E-11
7.33	3.30	0.444981	13.623669	3.45E-08	1.03E-10
8.00	0.31	0.520105	1.934901	6.62E-09	3.24E-11
8.00	0.68	0.520105	1.982214	8.49E-09	4.15E-11
8.00	1.04	0.520105	2.070784	1.01E-08	4.83E-11
8.00	1.41	0.520105	2.212403	1.17E-08	5.43E-11
8.00	1.77	0.520105	2.428778	1.33E-08	5.99E-11
8.00	2.14	0.520105	2.760433	1.52E-08	6.52E-11
8.00	2.50	0.520105	3.288990	1.73E-08	7.05E-11
8.00	2.87	0.520105	4.202959	2.00E-08	7.58E-11
8.00	3.23	0.520105	6.052262	2.36E-08	8.11E-11
8.00	3.60	0.520105	11.398840	2.93E-08	8.63E-11
8.67	0.31	0.589426	1.705223	5.67E-09	2.76E-11
8.67	0.71	0.589426	1.743015	7.33E-09	3.57E-11
8.67	1.11	0.589426	1.815475	8.73E-09	4.17E-11
8.67	1.51	0.589426	1.932650	1.01E-08	4.68E-11
8.67	1.91	0.589426	2.113135	1.16E-08	5.16E-11
8.67	2.30	0.589426	2.391702	1.32E-08	5.62E-11
8.67	2.70	0.589426	2.838457	1.50E-08	6.08E-11
8.67	3.10	0.589426	3.615481	1.74E-08	6.54E-11
8.67	3.50	0.589426	5.196615	2.05E-08	7.00E-11
8.67	3.90	0.589426	9.801579	2.56E-08	7.46E-11
9.33	0.31	0.651893	1.540301	4.98E-09	2.42E-11
9.33	0.74	0.651893	1.571098	6.49E-09	3.15E-11
9.33	1.17	0.651893	1.631494	7.74E-09	3.68E-11
9.33	1.61	0.651893	1.730250	8.97E-09	4.13E-11
9.33	2.04	0.651893	1.883651	1.03E-08	4.56E-11
9.33	2.47	0.651893	2.122200	1.17E-08	4.96E-11
9.33	2.90	0.651893	2.507426	1.34E-08	5.37E-11
9.33	3.34	0.651893	3.181690	1.55E-08	5.78E-11
9.33	3.77	0.651893	4.561906	1.83E-08	6.19E-11

9.33	4.20	0.651893	8.610176	2.29E-08	6.60E-11
10.00	0.31	0.707107	1.418909	4.47E-09	2.16E-11
10.00	0.78	0.707107	1.444384	5.86E-09	2.83E-11
10.00	1.24	0.707107	1.495426	7.00E-09	3.31E-11
10.00	1.71	0.707107	1.579813	8.10E-09	3.71E-11
10.00	2.17	0.707107	1.712062	9.27E-09	4.10E-11
10.00	2.64	0.707107	1.919397	1.06E-08	4.46E-11
10.00	3.10	0.707107	2.256756	1.21E-08	4.83E-11
10.00	3.57	0.707107	2.851318	1.40E-08	5.20E-11
10.00	4.03	0.707107	4.076044	1.66E-08	5.57E-11
10.00	4.50	0.707107	7.693105	2.09E-08	5.95E-11

Appendix D

Commercial MFC Electrode Electrical Field Values

x meters * 10 ⁻⁴	Ey V/m	x meters * 10 ⁻⁴	Ey V/m	x meters * 10 ⁻⁴	Ey V/m
0.0050	-1794	0.1683	-1980	0.3317	-2757
0.0099	-1794	0.1733	-1992	0.3366	-2801
0.0149	-1795	0.1782	-2004	0.3416	-2847
0.0198	-1796	0.1832	-2017	0.3465	-2895
0.0248	-1798	0.1881	-2031	0.3515	-2946
0.0297	-1799	0.1931	-2045	0.3564	-3000
0.0347	-1801	0.1980	-2059	0.3614	-3057
0.0396	-1803	0.2030	-2075	0.3663	-3116
0.0446	-1806	0.2079	-2090	0.3713	-3180
0.0495	-1809	0.2129	-2107	0.3762	-3247
0.0545	-1812	0.2178	-2123	0.3812	-3318
0.0594	-1816	0.2228	-2141	0.3861	-3394
0.0644	-1819	0.2277	-2159	0.3911	-3475
0.0693	-1823	0.2327	-2178	0.3960	-3562
0.0743	-1828	0.2376	-2197	0.4010	-3656
0.0792	-1833	0.2426	-2218	0.4059	-3756
0.0842	-1838	0.2475	-2239	0.4109	-3865
0.0891	-1843	0.2525	-2261	0.4158	-3984
0.0941	-1849	0.2574	-2283	0.4208	-4113
0.0990	-1855	0.2624	-2307	0.4257	-4255
0.1040	-1861	0.2673	-2331	0.4307	-4412
0.1089	-1868	0.2723	-2357	0.4356	-4587
0.1139	-1875	0.2772	-2383	0.4406	-4783
0.1188	-1883	0.2822	-2410	0.4455	-5005
0.1238	-1891	0.2871	-2439	0.4505	-5258
0.1287	-1899	0.2921	-2469	0.4554	-5553
0.1337	-1908	0.2970	-2500	0.4604	-5901
0.1386	-1917	0.3020	-2532	0.4653	-6320
0.1436	-1926	0.3069	-2565	0.4703	-6838
0.1485	-1936	0.3119	-2600	0.4752	-7504
0.1535	-1946	0.3168	-2637	0.4802	-8403
0.1584	-1957	0.3218	-2675	0.4851	-9715
0.1634	-1968	0.3267	-2715	0.4901	-11903
				0.4950	-16778

References

1. Adachi, K., Park, G., Inman, D. J., “Passive damping augmentation using macro-fiber composite actuators,” American Society of Mechanical Engineers, Aerospace Division (Publication) AD. v 67 2002. p 71-78.
2. Agbossou, A., Richard, C., Vigier, Y., “Segmented piezoelectric fiber composite for vibration control: Fabricating and modeling of electromechanical properties,” Composites Science & Technology. v 63 n 6 May 2003. p 871-881.
3. Akduman, I., Kress, R., “Electrostatic imaging via conformal mapping,” Inverse Problems. v 18 n 6 December 2002. p 1659-1672.
4. Azzouz, S. M., Bevan, J. S., Ro, J. J., Mei, C., “Finite element modeling of MFC/AFC actuators,” Proceedings of SPIE - The International Society for Optical Engineering. v 4326 2001. p 376-387.
5. Beckert, W., Kreher, W. S., “Modelling piezoelectric modules with interdigitated electrode structures,” Computational Materials Science 26 (2003) 36–45
6. Bent, A. A., Hagood, N. W., “Piezoelectric Fiber Composites with Interdigitated Electrodes,” Journal of Intelligent Material Systems and Structures, v. 8, November 1997, pp. 903-919.
7. Bent, A. A., “Active Fiber Composite Material Systems for Structural Control Applications,” Proceedings, SPIE’s 6th International Symposium on Smart Structures and Materials, Newport Beach, CA, March 1-5, 1999.
8. Bent, A. A., “Active fiber composite material systems for structural control applications,” Proceedings of Spie - the International Society for Optical Engineering. v 3674 1999. p 166-177.

9. Costamagna, E., “Numerical inversion of the Schwarz-Christoffel conformal transformation: strip-line case studies,” *Microwave & Optical Technology Letters*. v 28 n 3 Feb 2001. p 179-183.
10. Datta, S., Kirikera, G. R., Schulz, M. J., Sundaresan, M. J., “Continuous Sensors for Structural Health Monitoring,” *Proceedings of SPIE - The International Society for Optical Engineering*. v 5046 2003. p 164-175.
11. Driscoll, T. A., Trefethen, L. N., Schwarz-Christoffel Mapping, Cambridge University Press, Cambridge, UK, 2002.
12. Engan, H., “Excitation of Elastic Surface Waves by Spatial Harmonics of Interdigital Transducers,” *IEEE Transactions on Electron Devices*, v. ED-16, No. 12, December 1969, pp. 1014-1017
13. Goano, M., Bertazzi, F., Caravelli, P., Ghione, G., and Driscoll, T. A., “A General Conformal-Mapping Approach to the Optimum Electrode Design of Coplanar Waveguides With Arbitrary Cross Section,” *IEEE Transactions on Microwave Theory and Techniques*, v. 49, n. 9, September 2001 1573
14. Goddu, G., McDowell, D., Bingham, B., “Adaptive control of radiated noise from a cylindrical shell using Active Fiber Composite actuators,” *Proceedings of SPIE - The International Society for Optical Engineering*. v 3991 2000. Society of Photo-Optical Instrumentation Engineers, Bellingham, WA, USA. p 95-102
15. Hayt, W. H., Engineering Electromagnetics, Fourth Edition, McGraw-Hill, 1981, New York

16. Inman, D. J., Cudney, H. H., "Structural Machine Design Using Piezoceramic Materials: A Guide for Structural Design Engineers," Center for Intelligent Material Systems and Structures, Virginia Tech, 2000.
17. Jha, A. K., Inman, D. J., "Vibration Control of a Gossamer Toroidal Structure Using Smart Material Actuators and Sensors," Proceedings of SPIE - The International Society for Optical Engineering. v 5056 2003. p 475-486.
18. Kim, S. J., Hwang, J. S., Paik, S. H., "Direct Numerical Simulation of Active Fiber Composite," Proceedings of SPIE - The International Society for Optical Engineering. v 5053 2003. p 568-575.
19. Lewis, J. A., Inman, D. J., "Finite element modeling and active control of an inflated torus using piezoelectric devices," Journal of Intelligent Material Systems & Structures. v 12 n 12 December 2001. p 819-833
20. Morris, D. G., Hagood, N. W., Pizzochero, A., "Experimental investigation on the effect of environmental stress on Active Fiber Composite actuators," Proceedings of Spie - the International Society for Optical Engineering. v 3674 1999. p 296-305.
21. Mudarri, T. C., "A Novel Use for Ionic Polymer Transducers for Ionic Sensing in Liquid," Virginia Tech Electronic Thesis, etd-01062004-120129.
22. Otter, M. W., "Approximate Expressions for the Capacitance and Electrostatic Potential of Interdigitated Electrodes," Sensors and Actuators, A 96, 2002, pp. 140-144
23. Paliouras, J. D., Meadows, D. S., Complex Variables for Scientists and Engineers, Second Edition, Macmillan Publishing Company, New York, 1990
24. Park, G., Ruggiero, E., Inman, D. J., "Dynamic testing of inflatable structures using smart materials," Smart Materials & Structures. v 11 n 1 February 2002. p 147-155.

25. Prechtel, E. F., Hall, S. R., "Closed-loop Vibration Control Experiments on a Rotor with Blade Mounted Actuation," 2000, 41st AIAA Structures, Structural Dynamics and Materials Conference, Atlanta, GA.
26. Rossetti, G. A., Pizzochero, A., Bent, A. A., "Recent advances in active fiber composites technology," IEEE International Symposium on Applications of Ferroelectrics. v 2 2000. p 753-756 (IEEE cat n 00ch37076).
27. Ruggiero, E., Park, G., Inman, D. J., Wright, J., "Multi-input multi-output modal testing techniques for a gossamer structure," American Society of Mechanical Engineers, Aerospace Division (Publication) AD. v 67 2002. p 167-175.
28. Schulz, M. J., Sundaresan, M. J., Ghoshal, A., Pai, P. F., "Active fiber composites for structural health monitoring," Proceedings of SPIE - The International Society for Optical Engineering. v 3992 2000. Society of Photo-Optical Instrumentation Engineers, Bellingham, WA, USA. p 13-24.
29. Sodano, H. A., Park, G., Inman, D. J., "An investigation into the performance of macro-fiber composites for sensing and structural vibration applications," Mechanical Systems & Signal Processing. v 18 n 3 May 2004. p 683-697.
30. Varma, V. K., Dixon, W. E., "Design of a piezoelectric meso-scale mobile robot: A compliant amplification approach," Proceedings - IEEE International Conference on Robotics and Automation. v 2 2002. p 1137-1142 (IEEE cat n02CH37292)
31. Weber, E., Electromagnetic Theory, Static Fields and Their Mapping, Dover Publications Inc., New York, 1965.
32. Wilbur, M. L., Mirick, P. H., Yeager W. T., Langston, C., Cesnik, C. W., Carlos, E. S., Shin, S. J., "Vibratory loads reduction testing of the NASA/Army/MIT active twist

rotor,” *Journal of the American Helicopter Society*. v 47 n 2 April 2002. p 123-133.

33. Wickramasinghe, V. K., Hagood, N. W., “Performance characterization of active fiber composite actuators for helicopter rotor blade applications,” *Proceedings of SPIE - The International Society for Optical Engineering*. v 4699 2002. p 273-284.

34. Wickramasinghe, V. K., Hagood, N. W., “Durability characterization of active fiber composite actuators for helicopter rotor blade applications,” *Collection of Technical Papers - AIAA/ASME/ASCE/AHS/ASC Structures, Structural Dynamics and Materials Conference*. v 2 2003. p 998-1007.

35. Wilkie, W. K., Bryant, R. G., High, J. W., Fox, R. L., Hellbaum, R. F., Jalink, A., Little, B. D., Mirick, P. H., “Low-Cost Piezocomposite Actuator for Structural Control Applications,” *NASA Langley Research Center, Hampton, VA 23681-2199*

36. Williams, R. B., Grimsley, B. W., Inman, D. J., Wilkie, W. K., “Manufacturing and Mechanics-Based Characterization of Macro Fiber Composite Actuators,” *Proceedings of IMECE.02 2002 ASME International Mechanical Engineering Congress & Exposition, New Orleans, Louisiana, November 17-22,2002*

37. Williams, R. B., Park, G., Inman, D. J., Wilkie, W. K., “An overview of composite actuators with piezoceramic fibers,” *Proceedings of SPIE - The International Society for Optical Engineering*. v 4753 I 2002. p 421-427.

38. Yim, W., Singh, S. N., “Robust Output Feedback Force Control of Cantilever Beam using Piezoelectric Actuator,” *ASME International Mechanical Engineering Congress and Exposition, Proceedings*. v 2 2001. p 1843-1850

39. Smart Materials Corp. Website, 2004, <<http://www.smart-material.com>>

Vita

Justin Michael Lloyd

Since this is the only portion of this work that anyone will probably read, I'll do my best to make it an entertaining synopsis of my short, pitiful life. On the snow encrusted, inauspicious day of January 30, 1980, I was born in the ghetto of Hyattsville, Maryland. It wasn't that much of a ghetto back then, but I hear it's gone downhill since. Shortly after the even more disastrous birth of my brother, my family moved to West Germany (again, at the time) when I was at the tender and impressionable age of 3. I learned and saw many "cultural" things in Germany during my three year stay there, and I was regularly bitten on various extremities at the hands of classmates during my two years of German kindergarten. This taught me how to get along properly with people at an early point in my life. Around the age of 6, my family moved back to the U.S. to live in "God's Country", a.k.a. North Carolina. I began my formal educational experience in Cary, North Carolina, and finished all twelve years of my public education within the confines of this relatively urbane suburb of Raleigh. Apparently, the public schooling system isn't completely broken, and North Carolina State University, home of the Wolfpack, saw it fit to accept me as a Mechanical Engineering student. I completed my B.S.M.E. at N.C.S.U. in 2002 after four years of torturous study. During this time, I managed to achieve some mild successes building remotely Internet-operated backhoes, affectionately referred to by some as the "Hand of God". After graduation from N.C.S.U., I packed my bags and left my beloved homeland to venture into the wilds of southwestern Virginia, where I began to work for my M.S.M.E. at Virginia Tech. At Virginia Tech, I met many strange and disturbed individuals who have probably scarred me for life through their meddling in my affairs. Currently, I am destined to work for John's Hopkins APL in Columbia, Maryland. Hopefully things will continue to go relatively smoothly.